# Processing of Preceramic Polymers for Direct-Ink Writing

**A Dissertation Presented for the**

**Doctor of Philosophy**

**Degree**

**The University of Tennessee, Knoxville**

**James William Kemp**

**December 2021**

# DEDICATION

I dedicate this work to all the friends and family that have been with me throughout this process.

# ACKNOWLEDGEMENTS

This dissertation research was supported by the University of Tennessee-Knoxville Chancellor's Fellowship, the Air Force Research Laboratory scholars program, and Honeywell Federal Manufacturing and Technologies through contract DE-NA0002839, administered by Dr. Eric Eastwood, Dr. Jamie Messman, and Mr. Steve Patterson

I would also like the thank and acknowledge the following:

My parents, Bill and Joy Kemp, for their love and support throughout my entire education. You both taught me to work hard and try to do my best. All I can hope for is that I made you proud. I would also like to thank my grandparents Estelene Johnson and James Kemp. You both gave me a warm meal whenever I needed it and sat and talk to me for hours. I appreciate all you have done for me over the years.

My fellow lab mates who walked with me throughout this journey. Especially for the support, teaching me how to use equipment, and giving me pep talks to keep going along the way. I would like to thank Dr. Compton's group, especially Nadim Hmeidat, Cody Pack, Stian Romberg, and Madeline Wimmer.

To my friends, Jalen Blue, Trent Rogan, Abby Gibbons, Anna Peterson, Evan Lewozcko, Marisa Infield, and Vernon Stafford, thank you for being with me, praying for me, and keeping me sane during this process. You helped me through many tough times.

Dr. Karen Boyd and Dr. Denise Gardner for being professional mentors and becoming pseudo-aunt figures for me. Whenever I need time to decompress, you both opened your doors and allowed me to spend time with your dogs and cats. I am forever grateful for the care you showed me.

Dr. Chris Wetteland being the first professor that helped me understand difficult materials science concepts in a clear way. Your courses from my undergraduate prepared me to be a much better researcher.

My committee members Dr. Chad Duty, Dr. Claudia Rawn, and Dr. Lisa Rueschhoff for their valuable insight and encouragement. Especially Dr. Lisa Rueschhoff for her mentorship for my internships during the AFRL scholars programs.

Dr. Brett Compton for being a fantastic advisor. Thank you for seeing potential in me and helping me a better researcher. Whenever I needed guidance for my research, you were always extremely helpful. I enjoyed our random talks and constant snarky comments. Thank you for helping me “make it so” in regards to my research.

Most importantly, I would like to thank my Lord and Savior, Jesus Christ. Thank you for reminding me that my failures are not the end of my story but something to learn from. Thank you for loving me and keeping me safe and healthy in this entire process.

# ABSTRACT

Preceramic polymers are organosilicon polymers that, when pyrolyzed to above 1000°C, convert from a polymer to an amorphous ceramic. These polymers have been used for fiber spinning, polymer infiltration, and casting of materials but have recently gained interest for use as the feedstock material for additive manufacturing techniques. This work explores preceramic polymers being used for direct-ink writing (an additive manufacturing method) and many of the issues that occur with the polymers during curing and pyrolysis.

The first chapter of this dissertation provides a review of preceramic polymers, while the second and third chapters focus on the development of inks made of preceramic polymers. The second chapter uses a polysilazane polymer mixed with up to 43.3 volume percent hexagonal boron nitride as the rheological modifier to enable printing. The pyrolyzed parts are tested with 3-point flexure and microhardness indentation to observe failure behavior. The third chapter uses a polycarbosilane polymer with zirconium diboride and silicon carbide fibers as constituents for printable inks. These polycarbosilane-based inks exhibit much more porosity and crack development during curing and pyrolysis than the inks in the second chapter. Defects are characterized with micro-computed tomography and scanning electron microscopy. From the measured defects, new suggestions for decreasing porosity and crack development are discussed.

Building from the observations in the third chapter, the fourth chapter focuses on how the size of printed material influences the development of defects

and overall strength. Two new inks, similar to those in chapter three, are used with the addition that one of the formulations utilizes fumed alumina as an added viscosity modifier. The final study investigates printed rods of varying diameters (0.45 to 1.7 millimeter) to observe the effects of off-gassing during curing on the development of porosity. Failure strength is measured with 3-point flexure and Weibull statistics are used to understand how specimen size and ink formulation affect final specimen strength.

Overall, this dissertation shows that preceramic polymers are a viable option as a feedstock material for direct ink-writing and begins to quantify the degree to which part size and filler selection affect overall porosity development after curing and pyrolysis.

# TABLE OF CONTENTS

# LIST OF TABLES

# LIST OF FIGURES

# CHAPTER 1 COMPREHENSIVE REVIEW OF PRECERAMIC POLYMERS

## 1.1 Background Information

### *1.1.1 AM of Ceramics*

AM, more commonly called 3D-printing, is a processing technique to build objects in a layer-by-layer fashion. The objects are made by first using computer-aided design (CAD) to create a shape, then slicing into layers with slicing software. Finally, the sliced object is deposited onto a substrate layer by layer [1]. Building up material in this fashion allows complex geometry and design flexibility. AM can be used with a variety of material types utilizing a range of methods. Material can be formed by sintering of metallic or thermoplastic particles (selective laser sintering and electron beam)[2], thermoplastic polymer extrusion (fused deposition modeling)[1], photocuring of thermoset polymers (stereolithography)[3], laminating material (laminated object manufacturing) [4], and direct-ink-write of thermoset polymer fluid resins and aqueous slurries [5,6]. The focus of this study is on ceramic-based AM with preceramic polymer resins.

Most often, ceramic materials have been additively manufactured with stereolithography and DIW [7–9]. Stereolithography based methods use a concentrated light source or laser beam to crosslink a photocurable polymer on a platform to build up material. To create ceramic parts, the photocurable polymer is typically a liquid preceramic polymer that has added photo-initiators, or a solid preceramic polymer powder added to a photo-curable polymer [9,10]. Printing in this manner can create materials that have a high degree of geometric complexity and resolution. Work by Zocca, Zanchetta, and others has shown that SiOC

ceramic parts can be made with stereolithography methods; however, printed parts usually have a high amount of linear shrinkage (~25%) after full ceramic conversion [9,10]. Another setback for stereolithography is the limitation of only translucent and transparent materials. Opaque resins and filler materials do not allow the laser and light source to pass through them. Alternatively, DIW utilizes viscoelastic fluids with tailored rheological properties for material deposition. Exemplar fluids include epoxy-nanoclay based inks[11,12], polysiloxanes [13], and (specifically for ceramic-based materials) preceramic polymer inks[7,14]. DIW allows the use of a wide range of materials for ink formulation, including opaque fillers. Therefore DIW is the focus of this study. Printability is the first consideration during ink formulation for DIW.

Printable inks can be quantified by measuring how shear-thinning they are and what their yield stress ($\tau_y$) behavior is under an applied load. Both properties are widely characterized for DIW inks [5,6,15–17]. The degree to which an ink is shear thinning can be represented by the flow index in the power-law fluid model:

$$\eta = K\dot{\gamma}^{n-1} \tag{1.1}$$

where $\eta$ is the apparent viscosity, $K$ is the consistency index, $\dot{\gamma}$ is the shear rate, and $n$ is the flow index. In the case of shear-thinning fluids, n<1, while n = 1 for Newtonian fluids and n>1 for shear thickening fluids. One method to quantify shear yield stress can be quantified by observing the cross over point of storage and loss moduli, G' and G" respectively, with increasing load. Both the flow index and moduli values can be measured using parallel plate rheometry. Examples of these

measurements are shown in **Figure 1.1** from work by Compton and Lewis on epoxy, nanoclay-filled, and SiC-filled inks. $n$ can be found by performing linear regression over the viscosity data shown in **Figure 1.1a.** With a suitable rheology modifier, preceramic polymers can act as an excellent base material for DIW.

### *1.1.2 Preceramic polymers*

a. *Preceramic Polymer Development*

Preceramic polymers are a class of organo-silicon polymers that when pyrolyzed at temperatures above 1000°C, convert to an amorphous ceramic material. The polymer derived ceramics (PDCs) are of interest for use in extreme environments because the initial polymers can be shaped into complex structures and then converted to ceramic. During the conversion process significant mass and shrinkage can occur. The mass loss amount can be represented as a percentage of initial polymer mass, called ceramic yield. In general, the final ceramic yield and products are affected by the polymer's structure and makeup. Based on what is in the polymer chain backbone, different phases will be present in the final ceramic product. Other influences include the temperatures of thermal treatments and the pyrolysis atmosphere. Inert atmospheres can cause chemical reactions with the polymer backbone and create ceramics such as $Si_3N_4$, SiC, and others. Most of the Si-based preceramic polymers follow the oversimplified structure shown in **Figure 1.2.**

The X group determines the polymer derived ceramic (PDC) type and is made up of B, C, N, O, Si, or various combinations. An in-depth description of the

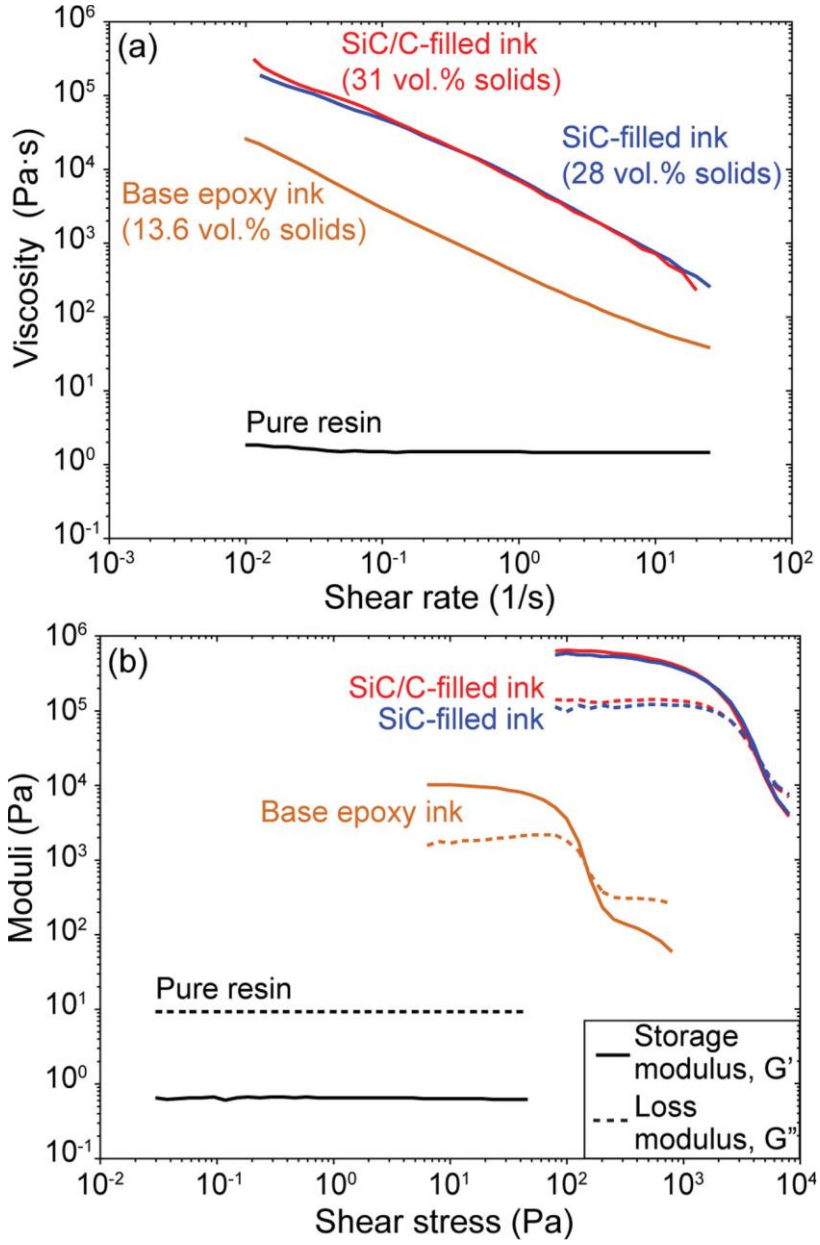


**Figure 1.1. Rheological measurements for epoxy/clay/SiC based inks for DIW** [18]**.**

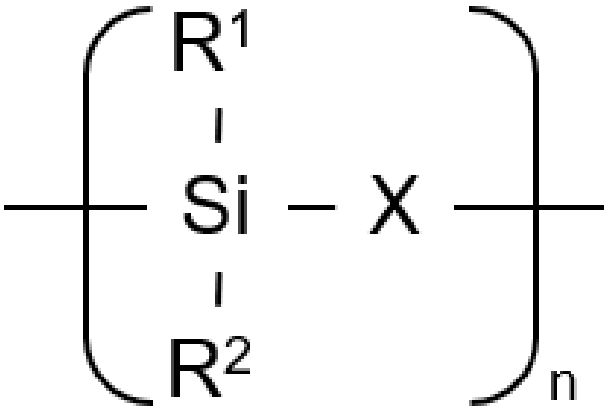


**Figure 1.2. - Oversimplified formula of silicon-based preceramic polymers (adapted from** [19]**)**

types of polymers is shown in **Table 1.1**. The R groups affect the polymer's thermal, mechanical, rheological, electronic, and optical properties before pyrolysis [19]. These R groups are typically either a hydrogen atom, alkyl, aryl, alkenyl, or other functional groups [20]. Therefore, these groups make up the carbon content, and eventual carbon burn-off during pyrolysis [19–21].

For polymer derived ceramics to be competitive with traditional ceramic manufacturing methods, they must be low cost. Fortunately, most preceramic polymers are synthesized from chlorosilanes, which are low cost and readily, commercially available[19]. Chloro-organosilicon compounds are essential to the synthesis of polysilanes, poly(carbosilanes), poly(organosilazanes), poly(borosilazanes), poly(silylcarbodiimides), poly(silsesquioxanes), poly(carbosiloxanes), and other silyl-containing polymers [19–22]. Other starting methods for preceramic polymers have been shown; however, none are as cheap and effective as methods with chlorosilanes [19]. **Figure 1.3** outlines many of these polymers and types in more detail. This current review will focus on two types of preceramic polymers in the following sections: Polycarbosilanes and Polysilazanes.

*Polycarbosilanes*

SiC fibers have been produced predominately by pyrolyzed polycarbosilanes. One such polymer is poly(methylcarbosilane) because of its high ceramic yield [23]. Fiber production follows the general process: distillation under

**Table 1.1: Silicon-based preceramic polymers organized by their X-groups**

| X-group class | Typical Molecules in group | Preceramic Polymer Classes |
|---|---|---|
| B | B-R | Polyborosilanes |
| C | $CH_2$ | Polycarbosilanes |
| N | NH | Polysilazanes, Polysilsesquiazanes |
| O | O | Polysiloxanes, Polysilsequioxanes |
| Si | Si | Polysilanes |

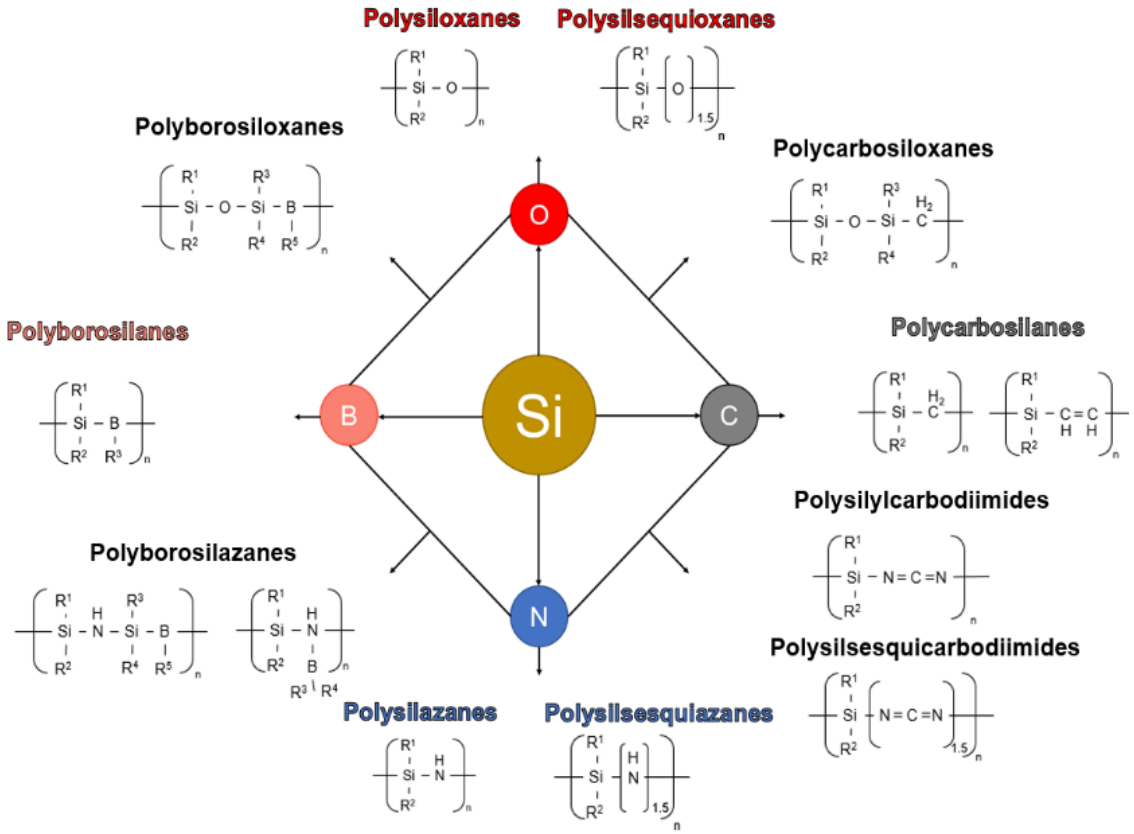


**Figure 1.3: Main silicon-based preceramic polymer classes and their structures (adapted from** [19]**)**

vacuum, melt spinning at 300°C, curing at 200°C, and a final pyrolysis step at 1200-1300°C.

Kumada first reported the synthesis of the polymers. The reaction is based on the thermal reorganization of a poly(methylsilane) to yield polycarbosilane [24]. The thermal process leads to the cleavage of Si-Si bonds to form Si-C bonds. This method of synthesis is known as Kumada rearrangement. Polycarbosilanes have a more complex structure when compared to other preceramic polymer classes. The X group, previously mentioned in **Fig. 1.1**, is made up of various hydrocarbons. These can range from methylidyne radicals to aromatic rings.

*Polysilazanes*

*b. Polymer Classes of Interest*

Currently, polysilazanes are used for higher temperature coatings of $Si_xN_y$ or SiCN systems on materials. They are used in the electronics industry to produce pure, porous $SiO_2$ coatings. The $SiO_2$ coating can provide anti-gas, anti-corrosion, or anti-tarnish barriers to metals because of their high oxidation resistance properties. Coatings are applied via curing in a moist atmosphere or with UV curing methods [25].

Typically, synthesis is performed in 1 of 2 of the following methods with chlorosilanes: ammonolysis or aminolysis reactions. The first report of an ammonolysis reaction was in 1964 by Kruger and Rochow. Both reactions have the problem of having leftover solid products: $NH_4Cl$ or $H_3NRCl$ [26]. Separation of the polymer and solid products can be difficult.

Polysilazanes are made of the Si - N backbone structure and have some of the highest ceramic yield of preceramic polymers [27]. However, there are some issues with the yield. Because of volatile oligomers, high molecular weight products can be complicated to produce. Methods to alleviate these problems have been reported [19].

One subset of polysilazanes of interest is polyborosilazanes. The SiBCN system is produced after full pyrolysis has led to high ceramic yield, temperature resistance, and oxidation stability. Polyborosilazanes are stable at higher temperatures (2000°C) without decomposition when compared to pure polysilazanes [28].

### 1.1.3 *Processing and Shaping of Preceramic Polymers*

The ease of shaping preceramic polymers makes them a viable route to make ceramics. PDC preparation from preceramic polymers is shown in **Figure 1.4**. The processing includes shaping of the polymer, curing, pyrolysis, and a higher temperature thermal treatment to form a crystalline ceramic. The preceramic polymer route to ceramic parts can be advantageous when compared to traditional ceramic processing methods for several reasons. Typical ceramic powder processing methods occur at much higher temperatures (1500-1700°C) [29], while preceramic polymers form glasses at ~1000°C [30]. Lower processing temperatures is not the only advantage to ceramic processing with preceramic polymers; like other polymers, they can be shaped into a green body. Processing methods can include resin transfer molding, warm pressing, fiber drawing,

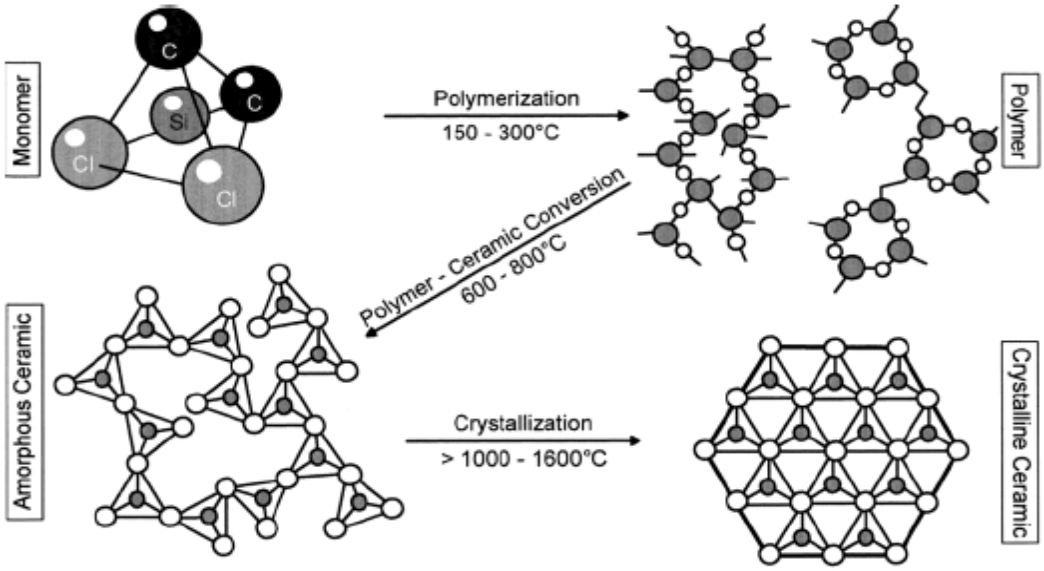


**Figure 1.4: Polymer to ceramic transition. Each step shows what the polymer structure looks like after a thermal treatment** [21]**.**

extrusion, injection molding, AM, and many others[19,21]. Shaping with polymeric techniques enables easier shape control when creating ceramic parts. Additionally, there are no issues centered around ceramic brittleness and tool wear [31].The ceramic precursors are either in the form of a cross-linkable liquid, meltable curable solid, or nonmeltable solid [19]. The polymers have additional functional groups (-OH, -H, and vinyl groups) to make them curable like thermoset polymers [19]. Curing of the polymers is caused by polycondensation or thermal cross-linking at or below 200°C. There are other curing techniques like UV, gamma rays, electron-beam, plasma, and others [32]. Cross-linking is of extreme importance because of its effects on final ceramic conversion after pyrolysis. If full cross-linking occurs during curing, then higher ceramic yield can be achieved [33]. Full cross-linking means that there are fewer oligomers and other low molecular weight chains that could volatilize, thereby achieving higher ceramic yield. Research has shown that the presence of catalysts helps lower the temperature of curing. One such example occurs with a polysilazane when mixed with dicumyl peroxide demonstrated by D'Elia and others [34,35]. It is important to note that the addition of catalysts can cause a change in rheology [36]. Finding a catalyst that does not significantly change the rheology of a preceramic polymer resin while also reducing the volatile nature of gas egress is of extreme interest for use in DIW. Other factors that affect the ceramic yield include the previously mentioned rearrangement steps and cleavage of carbon and hydrogen bonds [37].

## 1.2 Research Outline

The research focuses on the DIW preceramic polymer-based inks and many of the issues that plague the full processing of printed parts. The research focuses on the following objectives:

i. *Development of preceramic polymer-based inks:* Ceramic additive manufacturing is relatively immature when compared to metal and polymer methods. The development and optimization of ceramic precursor polymer-based inks for the additive manufacturing technique of direct ink writing to produce complex-shaped ceramic parts is an important avenue to expand ceramic additive methods. Polysilazane, a silicon nitride precursor, and hexagonal boron nitride are the chosen base materials for the printing feedstock. Rheological measurements, flexural tests, and hardness measurements are measured for the pyrolyzed inks. The printing of these preceramic inks is the focus of Chapter 2.

ii. *Direct ink writing of polycarbosilane and ultra-high temperature ceramic inks and associated porosity observations*: Building upon Chapter 2, new inks are developed with polycarbosilane (a silicon carbide precursor), zirconium diboride, and silicon carbide fibers. The rheological properties and failure strengths are measured similarly to how they were in Chapter 2. Fiber alignment is also measured. These inks are discovered to produce more porous final printed parts. The

printing of these inks and an outline of the causes for flaws in final pyrolyzed parts is outlined in Chapter 3.

iii. *Polycarobsilane microrod production and size effects on porosity*: Based upon the difference in porosity content between the inks in Chapters 2 and 3, a testing method for porosity development is necessary. Two inks are formulated that are similar to the ink that does not contain silicon carbide fibers in Chapter 3, but one with fumed alumina. Microrods with varying diameters are produced with the two inks. Flexural properties of the inks are shown, and Weibull analysis is performed to understand to what extent rod size and ink composition have porosity development. This work on the size effects of microrods is discussed in Chapter 4.

# CHAPTER 2 POLYSILAZANE-DERIVED BORON NITRIDE CERAMIC COMPOSITES VIA DIRECT-INK WRITING

A version of this chapter was originally published by James W. Kemp, Nadim S. Hmeidat, and Brett G. Compton:

Kemp, JW, Hmeidat, NS, Compton, BG. Boron nitride-reinforced polysilazane-derived ceramic composites via direct-ink writing. J Am Ceram Soc. 2020; 103: 4043– 4050. https://doi.org/10.1111/jace.17084

Changes to the text include removal of an equation, as it is already referenced as Eq. 1.1. NSH assisted with flexural testing. BGC assisted with data analysis and oversaw article writing and editing

## 2.1 Abstract

In this study we investigate the use of hexagonal boron nitride (hBN) as a rheology modifier in polysilazane resin to enable direct-ink writing (DIW) of polysilazane-derived boron nitride-reinforced ceramic composites. hBN is shown to effectively modify the flow properties of the resin by imparting strong shear thinning and yield stress behavior, and to reduce the mass loss and shrinkage associated with the polymer-to-ceramic conversion process, when compared to unfilled polysilazane resin. DIW inks are formulated with 40 vol.% hBN and used print flexural specimens and complex structures with high resolution. Mechanical properties of the resulting polymer-derived ceramic composites were evaluated by 3-pt. flexure and Vickers microhardness. The printed composites exhibit flexural strength of 56.4 MPa, and microhardness of 111.4 HV2.

## 2.2 Introduction

Additive manufacturing (AM) of ceramic materials has many advantages, primarily because it enables the creation of complex geometries that are not otherwise feasible to make with traditional ceramic processing approaches. In the last few years, attention has turned to the use of preceramic polymers as feedstocks for AM processes, which enable the creation of amorphous ceramic lattice structures with fine resolution using photo-initiated polymer resins [10,38]. However, unfilled preceramic resins suffer from 25-30% linear shrinkage during polymer-to-ceramic conversion[10,38]. Colombo, Greil, and others have studied the use of inert and reactive filler materials to mitigate shrinkage and porosity in polymer-derived ceramics, and shown that near-net-shape fabrication of ceramic composites is possible for the certain combinations of preceramic resin, filler, and pyrolysis conditions [19,22,27,39,40]. While light-based AM methods achieve high geometric resolution, such technologies are not amenable to resins containing high amounts of opaque fillers because these materials limit the penetration of light required to achieve complete cross-linking [41]. Direct-ink writing (DIW), on the other hand, utilizes paste-like viscoelastic feedstock materials that rely on a finite yield stress to maintain the printed shape after deposition. Such DIW feedstocks usually rely on filler materials with tailored surface chemistry to achieve yield stress behavior. For example, ceramic inks and slurries utilize dispersants and pH to tailor the interparticle pair potential between suspended particles [42–44], while polymer-based DIW inks rely on flow control agents such as functionalized

nanoclay or fumed silica [11,18,45], which form weak networks within the polymer to impart yield strength [46,47].

Because filler materials can mitigate shrinkage of preceramic polymers during pyrolysis, and because current DIW polymer inks rely on inorganic fillers to achieve rheological properties favorable for 3D printing [11], DIW is a uniquely suited processing method to produce polymer-derived ceramic composites in complex geometries with reduced shrinkage compared to both ceramic powder-based approaches and AM approaches that utilize unfilled preceramic polymers. Furthermore, DIW printing opens the door to new opportunities for printing ceramic composites with controlled fiber orientation or hybrid architectures that may be advantageous for achieving unique structural and functional properties. For example, Compton and Lewis demonstrated a high degree of alignment of SiC whiskers in fine-scale printed honeycomb architectures [18], Collino et al. combined DIW printing with acoustic focusing to achieve partitioning of disparate filler materials within a single printed line [48], and Raney et al. utilized a rotating print head to achieve helical arrangements of carbon fibers within printed composites that frustrate crack growth and improve damage tolerance [49]. By developing DIW feedstocks based on preceramic resins, these methods that have been developed for AM of polymer composites can be made equally accessible for the creation of novel high temperature ceramic composites. Recent work in this area has shown considerable promise [7,50,51], but to-date very few ceramic

precursors and filler materials have been investigated for use in DIW 3D printing of ceramic composites.

In this work, we show that hexagonal boron nitride (hBN) platelets are a promising high temperature filler material to impart desirable rheological properties to a polysilazane preceramic resin for the development of DIW ink. We show that polysilazane/hBN inks can be used to print tall, geometrically complex structures, and that the resulting polymer-derived ceramic composites display good mechanical properties with high geometric fidelity and low shrinkage (<8%, linear) due to pyrolysis. We anticipate that hBN platelets can be used similarly with a variety of preceramic resins and additional filler materials including fibers, whiskers, and ceramic powders to create a wide array of preceramic DIW feedstocks for a range of target structural and functional applications. In addition, we believe that the specific material system described in this work may find immediate application in 3D-printed thrusters, high temperature sensors, micro-reactors, battery materials, and heat exchangers [52,53].

## 2.3 Experimental Procedure

The preceramic polymer resin used in this study was Durazane 1800 (EMD Performance Materials Corp, Philadelphia, PA), a polysilazane resin with alternating Si and N atoms on the polymer backbone and methyl and vinyl functional groups in a ratio of 1:4 respectively [34]. The Durazane 1800 resin is a low-viscosity, colorless liquid with a density of 1.0 g/cc. The nominal chemical structure is depicted in **Figure 2.1a**. Dicumyl peroxide (DCP) was obtained from

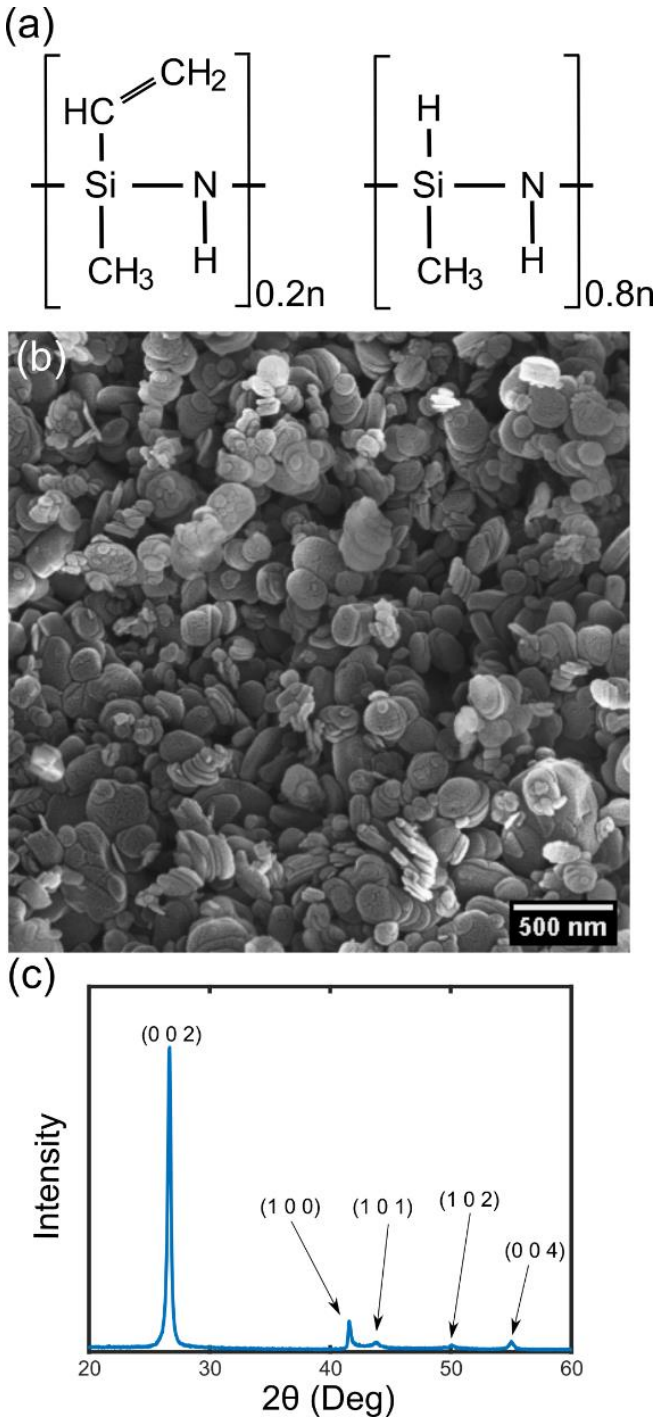


**Figure 2.1: (a) Nominal structure of Durazane 1800, (b) SEM micrograph of hBN particles, (c) XRD diffraction pattern for hBN**

Sigma Aldrich (St. Louis, MO) and used as a crosslinking initiator at a concentration of 2 wt.%, following D'Elia et al. [34]. HBN nanoplatelets with a density of 2.1 g/cc and nominal particle size of 500 nm were obtained from SkySpring Nanomaterials Inc. (Houston, TX). Morphology and phase of the boron nitride powder were confirmed with scanning electron microscopy (SEM) and X-ray diffraction (XRD) using an Auriga Crossbeam FIB/SEM (Zeiss Group United States) and Panalytical Empyrean diffractometer (Malvern Panalytical Ltd., Malvern, UK), respectively. Lattice constants were determined using Highscore Plus software (Malvern Panalytical Ltd.), and average agglomerate size was measured using a Beckman Coulter Multisizer 4E (Beckman Coulter, Indianapolis, IN).

The DCP was added to Durazane 1800 and stirred using a magnetic stir rod for 1hr at 20°C and ~500 rpm until the DCP had dissolved in the Durazane and bubble formation ceased. Hereafter, we will refer to the Durazane + 2 wt.% DCP mixture as the resin. Next, hBN nanoplatelets were incorporated into the resin using a centrifugal planetary SpeedMixer (FlackTek, Inc. Landrum, SC) in 98-mL plastic containers. Prior to mixing, the hBN platelets were dried at 70°C overnight to minimize water content. Four formulations containing 20, 30, 40, and 43.3 vol.%

hBN were prepared[1]. These inks were mixed with yttria-stabilized zirconia (YSZ) milling media (Inframat Advanced Materials LLC.) under vacuum at 0.1 atm at 1800 rpm for 6 minutes.

The rheological properties of the inks were measured with a Discovery HR-2 Rheometer (TA Instruments, New Castle, DE) using 40-mm-diameter flat platens. Filled formulations were measured using a 500 µm gap, while a 400 µm gap was used for the unfilled resin. All rheological measurements included a two-minute conditioning step at a constant shear rate of 0.1/s followed by a two-minute rest period. Oscillatory stress sweeps were measured in a range of 5 - 5000 Pa, and flow sweep measurements were taken at shear rates from 0.02-100 1/s. All tests were performed in ambient lab conditions (~21°C). The inks were then cast into 15-mm-diameter molds and cured in air by ramping up to 167°C at 3°C/min then back down to room temperature at the same rate, following D'Elia et al [34]. Thermo-gravimetric analysis (TGA) was conducted on samples cut from the cast discs using a Q500 TGA (TA Instruments). Samples were ramped up to 900°C at a ramp rate of 10°C/min under nitrogen atmosphere. The samples weighed approximately 0.5 mg prior to TGA.

---

[1] Volume percent was calculated with the following equation: $Vol.\% = \frac{\frac{m_1}{\rho_1}}{\frac{m_1}{\rho_1}+\frac{m_2}{\rho_2}} \times 100\%$ *(2.1)*

Where $m_1$ and $\rho_1$ are the mass and density of hBN respectively and $m_2$ and $\rho_2$ are the mass and density of the as-received Durazane1800 respectively. To find the proper mass of hBN for each volume percent, $m_1$ was solved for in Eq. 1.

Flexural bars and honeycomb samples were printed with the 40 wt.% ink using a custom DIW platform comprising a 3-axis gantry (ShopBot Tools, Inc., Durham, NC), solenoid valves, and a voltage-controlled air pressure regulator. The ink was manually loaded into 10cc syringe barrels (Nordson EFD) and centrifuged to reduce air pockets in the ink. The barrels were then loaded into an HP-3 air pressure adapter (Nordson EFD) and mounted on the printer. Objects were then printed onto glass substrates following print paths described in g-code and generated using custom scripts written in Scilab software (ESI Group, France).

Printed objects were pyrolyzed in a tube furnace (CM Furnaces Inc., Bloomfield, N.J.) under nitrogen flowing at 5.2 liters per minute (lpm) using the following heating schedule: 7°C/min up to 250°C, 3°C/min from 250°C to 1000°C, dwell at 1000°C for 4 hours, 3°C/min from 1000°C to 400°C, cool down to room temperature at 7°C/min. Density was measured using the Archimedes method.

The printed, pyrolyzed flexure bars were tested in three-point flexure on an electromechanical load frame (Model 45, MTS Systems Corporation, Eden Prairie, MN, USA) using a 10 kN load cell and cross-head rate of 0.8 mm/min. Specimens had dimensions of ~38 x 7 x 1.5 mm and tests were conducted at ambient temperature (~21°C). A span of 25 mm was used for all tested specimens. Samples were oriented such that the top surface – containing print features – was loaded in tension. Surfaces of the flexural bars were not ground or polished before

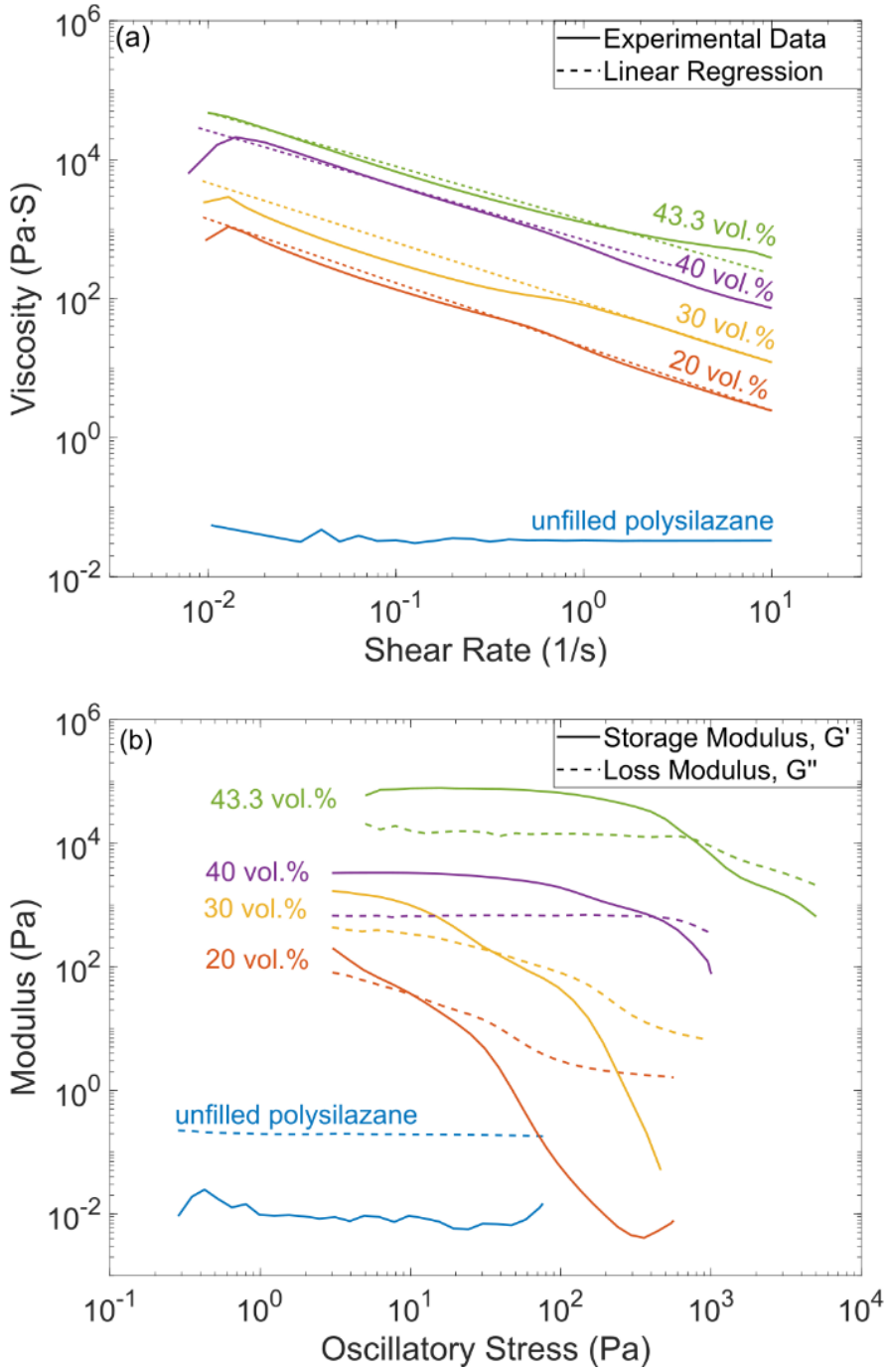


**Figure 2.2: Rheological behavior of hBN and polysilazane system. (a) Apparent viscosity vs. shear rate with linear regression highlights, and (b) Loss and storage moduli as a function of oscillatory shear stress.**

testing. Vickers hardness testing was conducted on polished cross-sections of printed bars using a Wilson VH1202 microhardness tester (Buehler, Lake Bluff, Illinois) with a 2 kg load and 10 second dwell.

Optical micrographs were taken with a VHX-5000 digital microscope (Keyence Corporation of America, Itasca, IL.). SEM of Vickers indentations and fracture surfaces was performed on the same Auriga Crossbeam FIB/SEM mentioned above.

## 2.4 Results

SEM micrographs reveal the powder to be comprised of platelet-like particles predominantly less than 500 nm in diameter (**Figure 2.1b**) and lattice constants of the powder were identified from the XRD pattern to be $a$ = 2.5012 Å and $c$ = 6.6884 Å, which are consistent with reported values (ICDD No. 01-073-2095) (**Figure 2.1c**). Average agglomerate size, as measured by the Coulter principle, is 6 µm. The unfilled Durazane 1800 resin behaves as a Newtonian fluid, possessing an apparent viscosity that is independent of shear rate over the range of shear rates probed. The addition of hBN leads to pronounced shear thinning and an increase in apparent viscosity that correlates with hBN content (**Figure 2.2a**). The presence of hBN also increases the storage and loss moduli (G' and G", respectively) in oscillatory stress measurements (**Figure 2.2b**). The unfilled resin has a loss modulus approximately one order of magnitude lower than its storage modulus, indicating a viscous fluid. In the loaded mixtures, the values of G' and G" are highly dependent on the applied shear stress, with significantly

higher G' values occurring at lower stresses (**Figure 2.2b**). With 30 vol.% hBN and higher, the mixtures display a plateau storage modulus ($G'_0$) and well-defined shear yield stress ($\tau_y$) that are characteristic of DIW inks. $G'_0$ is defined as the constant value of G' that exceeds G" exhibited in the low-stress region, and $\tau_y$ is defined as the transition from solid-like to liquid-like behavior with increasing shear stress of an ink as represented by G' and G" crossing each other in **Figure 2.2b.** The 40 vol.% and 43.3. vol.% mixtures display $G'_0$ and $\tau_y$ values of 76.3 KPa and 427 Pa, and 3.3 KPa and 711 Pa, respectively. The ink containing 43.3 vol.% was tested as a possible candidate for printing, however, it did not print reliably at the practical printing targets of a 410 µm nozzle size and 25 mm/s translation speed, which require a driving pressure of less than 360 psi for the custom printing set-up. Based upon experience with the 43.3 vol.% ink and on rheological characterization, the mixture containing 40 vol.% hBN was selected for printing flexural bars and complex geometries, including a honeycomb and multi-walled hourglass geometry (**Figure 2.3a,c**). The ink was printed using a 410 µm nozzle and extruded consistently and reliably without clogging. After deposition, the ink recovered solid-like behavior and retained the printed shape. Inks with less than 40 vol.% hBN did not retain their shape after extrusion.

TGA thermograms of the samples cut from cast, cured discs show two distinct degradation events centered at 380°C and 600°C for all ink formulations (**Figure 2.3e**). Dried hBN powder alone shows a negligible change in mass across the entire temperature range, and the presence or absence of hBN in the resin

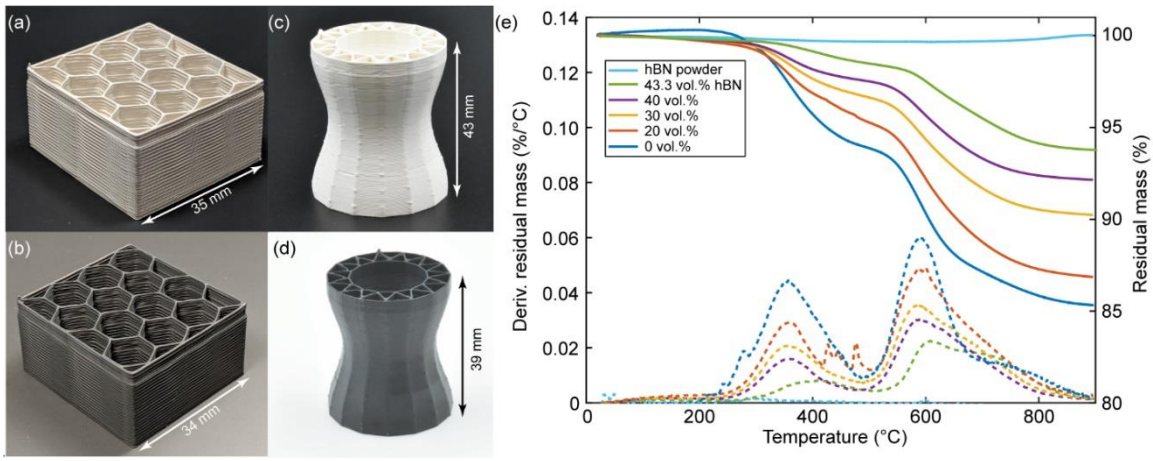


**Figure 2.3: Printed honeycomb (a) before and (b) after pyrolysis at 1000°C. Printed hourglass shape with complex inner channels (c) before and (d) after pyrolysis at 1000°C. Both the honeycomb and hourglass prints were made from made of polysilazane with with 40 vol.% hBN ink. (e) Residual mass percent (right axis) and derivative of residual mass percent (left axis) of hBN and polysilazane mixes during TGA in nitrogen atmosphere. Curves indicate that the presence of hBN does not strongly affect the pyrolysis of the polysilazane resin.**

does not alter the basic degradation profile of the unfilled resin, supporting the assumption that hBN acts as an inert filler. The presence of an inert phase serves to reduce the total fraction of mass lost during pyrolysis. Here, the unfilled resin loses 15% mass during pyrolysis, while the mixtures containing 30, 40, and 43.3 vol.% hBN lose 10, 8, and 6% mass, respectively. During TGA, samples containing less than 40 vol.% hBN cracked into several pieces, precluding measurement of the dimensional change associated with pyrolysis. The cast TGA specimen containing 40 vol.% hBN exhibited 2.31% linear shrinkage. After pyrolysis in the tube furnace, the printed flexural bars exhibited linear shrinkage of 6.4 ± 0.2% along the print direction and 7.5 ± 0.6% transverse to it, while the printed honeycomb shrank 3.4% along the longest edge, 7.4% along the shorter edge, and 6.6% in the through-thickness direction (**Figure 2.3b**). The hourglass geometry shrank 9.3% in height and 2.7% in diameter during pyrolysis (**Figure 2.3d**).

The flexural strength of the pyrolyzed bars was 56.4 ± 7.6 MPa, and the flexural modulus was measured to be 28.9 ± 1.3 GPa (**Figure 2.4**). Vickers microhardness was measured to be 111.9 ± 7.11 HV2 (1.10 GPa) on cross-sections oriented normal to the print direction. Optical micrographs of the fracture surface of flexure bars show a uniform microstructure with minimal evidence of discrete print paths or large hBN agglomerates (**Figure 2.5a**). SEM of the fracture surface reveals a dense microstructure with evidence of significant pull-out of individual hBN platelets or small stacks of platelets (**Figure 2.5b**). SEM in the

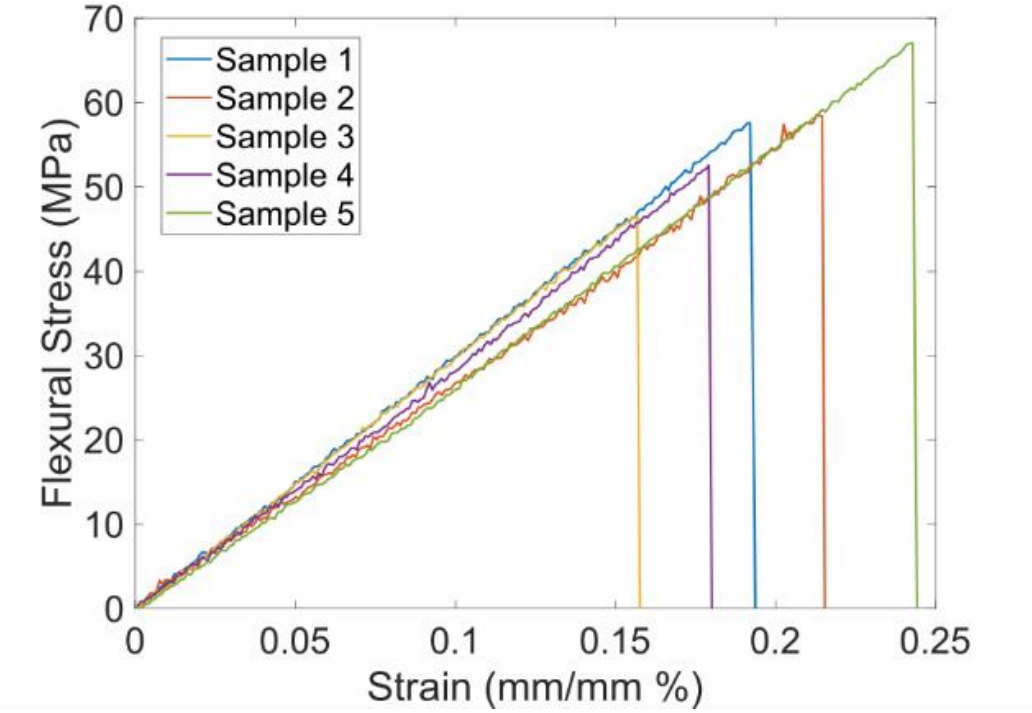


**Figure 2.4: Flexural stress-strain curves for printed flexural specimens made with 40 vol.% hBN.**

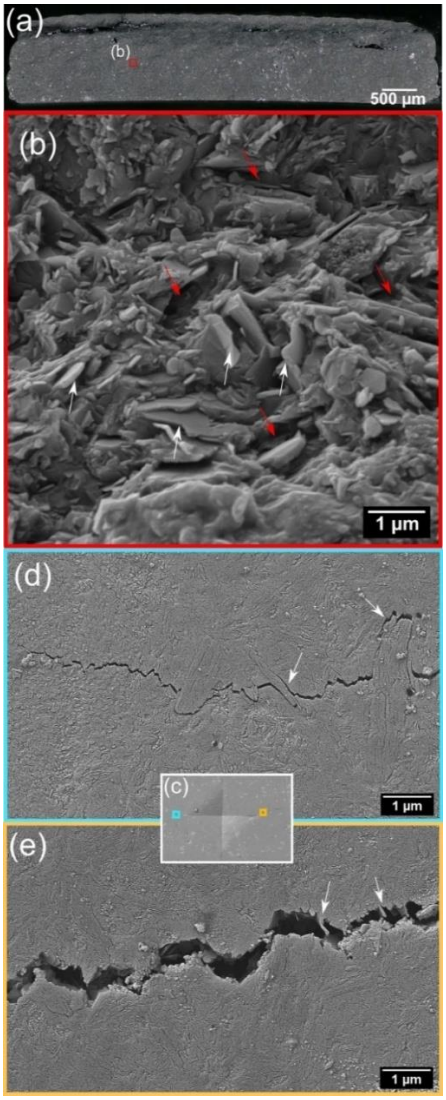


**Figure 2.5: (a) Optical and (b) SEM micrographs of the fracture surface of a tested flexural specimen. (c) Vickers indentation on a polished cross-section of the same specimen. (d-e) Crack tips from Vickers indentation showing crack deflection, bridging, and pullout from the hBN platelets. White arrows highlight hBN stacks around which the crack was deflected while red arrows indicate voids caused by platelet pull-out**

vicinity of a Vickers indentation provides corroborating evidence of pullout and crack deflection around hBN platelets and stacks of platelets (**Figure 2.5 c,d**).

## 2.5 Analysis and Discussion

Despite the absence of any chemical surface functionalization, the hBN platelets at high volume percent loading are effective at imparting shear thinning and yield stress behavior to the polysilazane resin as shown in **Figure 2.2**. Shear thinning is an empirically-based, common feature for DIW inks [see the following references for further discussion] [5,15,17,54] and can be quantified by the flow index in the power-law fluid model shown in Eq 1.1. In the case of shear thinning fluids, $n<1$, while $n = 1$ for Newtonian fluids and $n>1$ for shear thickening fluids. Numerical values for n were calculated by linear regression over the linear portion of the curves and are indicated in **Figure 3.2**. Values vary from 0.09 to 0.13 to 0.14 for 20 vol.%, 30 vol.%, and 40 vol.% hBN, respectively, indicating good shear thinning across a wide range of solids loading. These values compare favorably to values measured for other successful thermoset-based DIW inks that utilize fumed silica or layered silicates as rheology modifiers. The shear yield stress value for the present ink also compares favorably to other printable thermoset-based DIW inks, albeit at significantly higher solids loading [11]. Other rheology modifying fillers like nanoclays and fumed silica have shown an increase in shear-yield behavior with proper surface functionality and exfoliation [12,55]. If the hBN platelets had proper surface functionality and exfoliation, we believe that an increase in shear-yield behavior is possible given how other fillers behave with

similar treatment. To date, the authors could find no literature on these processing methods on hBN for rheological modification and needs further research.

Because of the high hBN loading in the printable ink formulation, the shrinkage due to pyrolysis is substantially reduced compared to unfilled polysilazane, which has been reported at 25% linear [56]. We attribute the difference in shrinkage between the TGA samples and the flexure bars to the higher pyrolysis temperature and longer dwell period for the flexure bars. The anisotropic shrinkage observed for the printed flexural bars seems to indicate that the hBN platelets are at least partially aligned by the deposition process. Alignment of high aspect ratio filler materials has been studied in depth for traditional extrusion processes and has been reported for carbon nanotubes, carbon and glass fibers [45,49,57–59], SiC whiskers [18], and more recently, nanoclay platelets [11] and graphene flakes [60] in material extrusion AM processes. This feature represents a new avenue to tailor and spatially control directional properties in ceramic composites that is a direct result of the printing process. From literature, the a-direction lattice parameter of hBN has shown minimal to no expansion at an elevated temperature while the c-direction greatly increases [61]. The anisotropic CTE of hBN suggests further evidence of alignment because of the reduced amount of linear shrinkage made possible by the low CTE in the direction of printing.

The present ceramic composite exhibits elastic modulus and Vickers hardness values that are significantly lower than that of the matrix alone, which

have been reported as 117 GPa and 11.3 GPa, respectively, for a similar polysilzane resin pyrolyzed at 1000°C [56]. We attribute this difference primarily to incomplete exfoliation of the hBN agglomerates, which are in the form of stacks, much like layered silicates. Because the bonding is weak between individual platelets, these interfaces act as shear faults that serve as initiation points for inelastic deformation, leading to reduced hardness [62,63]. Ruigang et al. observed similar behavior in $Si_3N_4$/hBN (hBN platelet size of 0.53 micron) composites, where the Vickers hardness decreased from nearly 19 GPa for the $Si_3N_4$ alone to 5 GPa for a composite containing 25 vol.% hBN, and the elastic modulus decreased from 240 GPa to 180 GPa over the same range [63]. Other groups have reported similar effects from hBN in other ceramic materials, including aluminum nitride (AlN) and silicon aluminum oxynitride (SiAlON) [64,65]. Decreases in mechanical properties are accompanied by an increase in fracture toughness, neutron cross-section, lubricity, machinability, thermal conductivity, and thermal shock resistance.

## 2.6 Summary and Conclusions

In this study we have shown that hBN platelets can be used as an inert, high temperature viscosity modifier to impart shear thinning and yield stress behavior to a polysilazane preceramic polymer to enable DIW of SiCN/hBN ceramic composites. To the authors' knowledge, this is the first report of DIW of hBN-based composites, and the first report of a non-silica-based high temperature ceramic as the viscosifying additive for preceramic DIW inks. Although the high

hBN content reduces the hardness and strength of the ceramic matrix, we believe the ability of a DIW ink formulation to accommodate, and sometimes require, high solids loading is a distinct advantage compared to other AM routes that have been used to print preceramic polymers. In the present case, the hBN serves to simultaneously impart favorable rheology for printing and significantly reduced dimensional change as a result of pyrolysis and hBN alignment. Recent developments in X-ray CT analysis on printed parts present exciting opportunities for future work to determine the exact amount of platelet alignment in filled polymer systems [59]. We anticipate that recent developments in surface functionalization of hBN [66] may lead to significantly stronger rheology-modifying behavior at lower solids loading levels, thereby presenting greater opportunities for the incorporation of other filler materials that may be desired for specific structural or functional properties, for example, the inclusion of ceramic fibers or ultra-high temperature ceramic powders.

# CHAPTER 3 DIRECT INK WRITING OF $ZrB_2$-SIC CHOPPED FIBER CERAMIC COMPOSITES

A version of this chapter was originally published by James W. Kemp, Abel A. Diaz, Elizabeth C. Malek, Brendan P. Croom, Zlatomir D. Apostolov, Surya R. Kalidindi, Brett G. Compton, Lisa M. Rueschhoff

Kemp JW, Diaz AA, Malek EC, Croom BP, Apostolov ZD, Kalidindi SR, Compton BG, Rueschhoff LM. Direct Ink Writing of ZrB2-SiC Chopped Fiber Ceramic Composites. Additive Manufacturing. 2021 May 21: https://doi.org/10.1016/j.addma.2021.102049

Changes to the text include removal of an equation as it is already referenced as Eq. 1.1. AAD and ECM assisted with fiber alignment and porosity volume calculations. AAD also assisted with writing. BPC performed micro-CT measurements. ZDA and SRK provided guidance for the article. BGC and LMR helped analyze data and assisted in writing.

## 3.1 Abstract:

Ultra-high temperature ceramics (UHTCs) are of interest for thermally- and/or mechanically- extreme environments because of their high melting temperatures (>3000°C) and ablation resistance. More widespread use is limited by low fracture toughness and inability to be processed into complex-shaped components. Here, we report the production of fiber-reinforced UHTC matrix composites (UHTCMCs) formed via the additive manufacturing technique of direct

ink writing (DIW). Slurry 'inks' were developed containing up to 47.5 vol.% of the UHTC zirconium diboride ($ZrB_2$), up to 10 vol.% chopped silicon carbide fiber ($SiC_f$), and a silicon carbide (SiC) precursor polymer. Lattice structures and flexural specimens were printed and pyrolyzed to form UHTCMCs with aligned (relative to the print direction) $SiC_f$ in the $ZrB_2$ – SiC matrix. Flexural strength of fiber-containing parts is presented, and fiber alignment due to deposition is analyzed with X-ray computed tomography. Defects that occurred during the DIW process, and their probable causes and mitigation strategies are also discussed.

## 3.2 Introduction

Ultra-high temperature ceramics (UHTCs) are a group of boride, carbide, and nitride ceramics characterized by their high melting points (>3000°C) [29,67]. As such, UHTCs are excellent candidate materials for use in extreme environments such as high-speed flight, where temperatures at leading edges and control surfaces can exceed 2000°C [68]. Diboride ceramics, like zirconium diboride ($ZrB_2$) and hafnium diboride ($HfB_2$), are of interest for the aforementioned applications because of their higher oxidation resistance and thermal conductivity when compared to other UHTCs [69,70]. Of the diborides, $ZrB_2$ is of particular interest in particle loaded slurries for ease of particle stabilization due to the decreased density over $HfB_2$ (6.08 vs. 10.5 g/cm$^3$) [29]. Other processing methods (e.g., injection molding [71], freeze-casting [72], freeze-form extrusion [73], tape casting [74], and gel casting [75]) have been used to produce near-net-shape $ZrB_2$

components. However, all processing methods still yield monolithic $ZrB_2$ that exhibits brittle failure, limiting the use in harsh environments.

The addition of fibers to UHTCs to form UHTC matrix composites (UHTCMCs) promotes more graceful failure compared to monoliths and could provide increased thermal and environmental protection compared to classical CMCs (e.g., C/C, C/SiC) [76,77]. Fibers used for reinforcement include carbon ($C_f$) and silicon carbide ($SiC_f$) in both chopped and continuous form (e.g., 2D lay-ups, 3D woven architectures) [76]. Ultimately, the choice of fiber, fiber architecture, and processing routes are dependent upon the needs of the desired application [69]. While continuous fiber UHTCMCs provide the most significant improvement in mechanical performance, their near-net shaped processing remains difficult [74,75]. Chopped and discontinuous fibers offer improvement in fracture toughness over monolithic UHTCs [78,79]. For example, Silvestroni et al. reported a 52% increase in fracture toughness with the addition of 20 vol.% chopped $SiC_f$ to $ZrB_2$ relative to monolithic $ZrB_2$ [80]. While many have proven the structural benefit of chopped-fiber additions to improve the mechanical performance of UHTCs, all employ geometrically simple processing routes such as die-pressing [80–83]. Generally, these approaches result in randomly oriented fibers or slight orientation if pressure is applied in the forming/sintering process [84]. Little has been done to explore and/or quantify the alignment of fibers during processing, and how that may improve the mechanical performance of UHTCMCs.

Additive manufacturing (AM) offers the possibility of creating near-net shaped components with controlled fiber alignment. The AM technique of direct ink writing (DIW) is of particular interest due to past success in creating polymer matrix composite (PMC) structures with enhanced stiffness due to the alignment of chopped fibers [18,57,59,85]. DIW utilizes viscoelastic, paste-like feedstock that is extruded from a nozzle and deposited in a layer-by-layer fashion to build up complex parts. The feedstock must have a sufficient yield stress ($\tau_y$) and storage modulus (G') to hold the as-deposited shape after printing[5,11,15,16,54,86,87]. This technique has been used to manufacture ceramics via highly loaded aqueous-based slurries [88–90] and loaded preceramic polymer inks [7,9,14,51]. The use of preceramic polymers, a class of inorganic polymers that convert to ceramic upon pyrolyzation, can eliminate the need for the addition of a large amount of solvent and/or sacrificial polymer binder [19].

There has been limited work up until now on the processing of CMCs via DIW [7,91,92]. Most of the referenced work has focused on chopped fiber additions due to the difficulty of incorporating a continuous fiber filament into existing DIW processes. In one of few examples, Zhao et al. have reported the incorporation of continuous $SiO_2$ fibers into a preceramic ink matrix via a customized print head that directly feeds a single continuous fiber into the nozzle during deposition. [92]. The rest of the work in this area includes the addition of chopped $SiC_f$ or $C_f$ as reinforcements into preceramic polymer-based inks [7,8,93,94]. Franchin et al. gave an in-depth description of chopped $C_f$ loaded preceramic polymer inks for

CMC production [8]. They discussed the interplay between rheology and printability, as well as the increased toughness that fiber inclusion causes. Mechanics for the single printed filaments are promising, but do not reflect the performance of complex and larger components with road-to-road interactions. More component-representative work includes a study by Xiong et al. reporting the use of polymer infiltration and pyrolysis (PIP) to fully densify CMCs made via DIW of preceramic polymers [93]. However, there is still a gap in reported literature on a comprehensive understanding of the impacts of fibers on ceramic ink rheology, printability, and defect evolution through processing. This knowledge, along with expansion into high-temperature ceramic matrix phases, is needed to advance current state-of-the-art.

In this work, we show an example of additive manufacturing of UHTCMCs, ultimately creating near-net and complex shaped parts of $SiC_f$-reinforced $ZrB_2$-SiC. DIW inks containing $ZrB_2$ powder, PCS, and chopped $SiC_f$ have been developed and characterized as a function of $SiC_f$ content. We demonstrate the ability of this ink to make geometrically complex ceramic composites with a low amount of linear shrinkage (<5%). Defect evolution through processing steps was investigated with identification of mitigation steps for future studies. Fiber alignment is quantified, and flexural strengths of printed specimens are presented.

## 3.3 Experimental

### *3.3.1 Materials and mixing*

A commercially available allylhydridopolycarbosilane SiC-yielding preceramic polymer, SMP-10 (Starfire Systems Inc., Schenectady, NY), was used in this study as the base for DIW inks. SMP-10 has a polydispersity index of 5.544 and a 72-78 wt.% ceramic yield [33,95]. The PCS thermally cross-links without the addition of a catalyst at 250°C and begins to form SiC crystallites at 1250°C [33]. The low temperature thermal cross-linking process is onset by two main reactions: hydrosilylation and dehydrocoupling [96]. **Table 3.1** summarizes the three inks that were developed for this study, all contain only three components: PCS polymer, $ZrB_2$ powder, and $SiC_f$. No additional dispersant or solvent was added to the PCS preceramic polymer.

The as-received $ZrB_2$ (H.C. Stark GmbH, Grade B, Goslar, Germany) used in this study had an average particle size of 3.6 µm, as measured via a multi-wavelength particle size analyzer (Beckman Coulter, LS 13 320 Particle Size Analyzer, Indianapolis, IN). Particle size reduction was achieved via ball milling for 24 hours in ethanol with 5 mm diameter SiC milling media (average particle size 1.3 µm, Fig. S1). A 50/50 by weight blend of milled and unmilled powder was used for the inks in an attempt to increase particle packing for maximum solids loading [97]. The $SiC_f$ (UBE Industries, LTD, Tyranno SA3, Yamaguchi, Japan) had a diameter of 10 µm. The SiC fibers were hand-cut with cleaned laboratory scissors to ~1 cm before adding to the ink mixture.

**Table 3.1: Composition of inks used for DIW, containing volume percent of each material in the inks.**

| Ink Name | SMP-10 [vol.%] | $ZrB_2$ [vol.%] | SiC fiber [vol.%] | Average SiC fiber length (mm) |
|---|---|---|---|---|
| SMP-0f | 52.5 | 47.5 | 0.00 | - |
| SMP-5f | 52.0 | 42.2 | 5.77 | 0.27 ± 0.17 |
| SMP-10f | 51.2 | 38.8 | 10.0 | 0.22 ± 0.14 |

The first ink did not contain $SiC_f$ (SMP-0f) and was designed to have as high of $ZrB_2$ loading as extrudable to minimize pyrolysis shrinkage. $SiC_f$ was added at both 5.75 and 10 vol.% (SMP-5f and SMP-10f, respectively) to identify any effects of fiber loading on rheology, fiber alignment, and material properties. These fiber amounts were chosen as benchmarks to understand the effects of fiber additions and to find the upper limit of fiber incorporation. For increasing amounts of $SiC_f$, the amount of $ZrB_2$ was reduced in order to keep the total ceramic content ($SiC_f$ + $ZrB_2$, ~48 vol.%) similar in all three inks. This made it possible for the effects of fiber additions alone on the ink rheology and printed part fidelity to be investigated.

A planetary vacuum mixer (Thinky USA Inc., ARV-310LED, Laguna Hills, CA) was used to mix all inks. Each formulation was mixed by first adding the total amount of SiC chopped fiber to the neat PCS polymer and mixing for 9 minutes in increments of 90s at 1800 rpm. $SiC_f$ was added first to understand the effects that mixing alone had on fiber length. $ZrB_2$ was added in three equal mass increments followed by mixing for 90s at 1800 rpm to reach the desired volume fraction, as shown in **Table 3.1**. Gradual introduction of the $ZrB_2$ in these smaller increments allowed for better mixing and incorporation into the polymer. To calculate values of average fiber length for each fiber-containing ink, a small aliquot of ink was removed after the total mixing time, placed on a glass slide, and diluted with a small amount of Tetrahydrofuran (THF). Several images of the diluted aliquot were taken on a VHX-5000 digital microscope (Keyence Corporation of America, Itasca,

IL.), and fiber length was measured manually with ImageJ. The average and standard deviation of the measured fiber length after mixing is shown in **Table 3.1**.

### *3.3.2 Rheological properties*

The rheological properties of the inks were measured with a Discovery HR-2 Rheometer (TA Instruments, New Castle, DE) using a 40-mm-diameter aluminum, flat platen, and Peltier base. Testing was kept at a constant temperature of 25°C. Filled formulations and the unfilled polymer were measured using a 500 µm and 250 µm gap size, respectively. For the unfilled polymer, larger gap sizes resulted in torques, displacements, or rotation rates that were outside of the measurement range of the machine. All rheological measurements included a two-minute pre-conditioning step at a constant shear rate of 0.1/s followed by a two-minute rest period. Oscillatory stress sweeps were measured between of 5 - 5000 Pa, and flow sweep measurements were taken at shear rates from 30 - 1000 1/s and 0.02 - 50 1/s for the neat polymer and filled inks, respectively. All tests were performed in ambient lab conditions (~21°C).

### *3.3.3 Printing and pyrolysis*

A Hyrel System 30M printer (Hyrel, Norcross, GA) with a displacement-controlled syringe extruder attachment (VOL25) with a Luer lock, tapered nozzle with an exit diameter of 0.840 mm (Nordson EFD, Westlake, OH) was used for printing. Inks were loaded by hand with a spatula into a 20cc aluminum syringe (Hyrel VOL25 extruder head). Printing was conducted at room temperature with a

print head speed of 14 mm/s. The deposition rate was specified as 9.87 $mm^3/s$ based upon the nozzle size and print speed. Porous PTFE film (Coast-Line International, Release Ease 234TFP-1, Amityville, NY) was taped onto the glass slide printing platform for ease of removal after printing. Custom print paths were made from g-code scripts written in Scilab open-source software (ESI Group, France). Examples of prints made from each ink are shown in **Figure 3.1**. **Figure 3.1C** shows the tallest attempted print at 10 mm high, corresponding to 15 printed layers (using a layer height of 0.67 µm during printing). After printing, specimens were cured in a vacuum oven (MTI Corporation, Richmond, CA) a 1°C/min ramp rate to 160ºC with a 1 hr hold, then at the same ramp rate up to 230°C and another 1 hr hold, followed by cooling to room temperature at 5°C/min. Pyrolysis was performed in a tube furnace (CM Furnaces Inc., 1830-10 VF, Bloomfield, NJ) with a graphite sleeve and flowing argon at a rate of 5.2 liters per min (lpm). The pyrolysis schedule was as follows: 1°C/min to 1200°C with 1hr holds at 300, 450, and 600°C and 2hr holds at 800 and 1200°C on the ramp up, then cooled to room temperature at 5°C/min. Both curing and pyrolysis schedules were based upon previous thermal characterization of the PCS polymer [33,98]. The onset of pyrolysis, associated with the decomposition of the polymerized allylic cross-linking groups, occurs around 400°C and the mass losses associated with the pyrolysis are concluded by 900°C [98]. At elevated temperatures through 1200°C, amorphous SiC forms via atomic rearrangement, with higher temperature treaments yielding crystallization [98]. Other reports of UHTCMC matrix

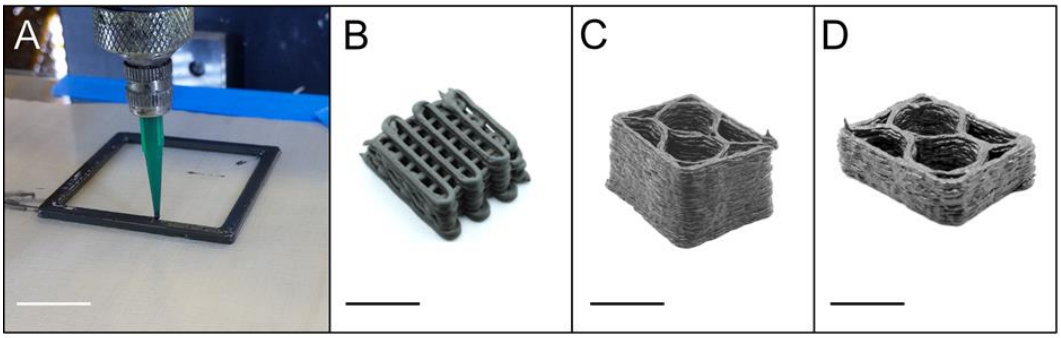


**Figure 3.1: (A) Example of UHTC based ink being printed and pyrolyzed structures made from (B) SMP-0f, (C) SMP-5f, (D) and SMP-10f. All scale bars are 1 cm.**

densification using similar UHTC powder/PCS blends used similar pyrolyzation temperatures of 1200 – 1300°C but required post infiltration and pyrolysis or hot pressing at 1650°C for enhanced densification [99–102] In the present work, higher temperature pyrolysis steps were not considered because of the porosity and cracking that formed in the printed parts after the initial 1200°C pyrolysis. Additionally, strength degradation has been observed in SiC fibers with pyrolysis temperature above 1400 – 1500°C [103].

Archimedes density (based upon ASTM B962 – 17) was measured on 5 printed, pyrolyzed parts made from each of the three inks [104]. Pyrolyzed flexural bars were tested in three-point flexure on an electromechanical load frame (Model 45, MTS Systems Corporation, Eden Prairie, MN, USA) using a 10 kN load cell and crosshead rate of 0.5 mm/min. Specimens had dimensions of ~45 x 4 x 3 mm with a span of 40 mm, and tests were conducted at ambient temperature (~21°C) following ASTM C1161 [105]. In accordance with the standard, grinding was done perpendicular to the load directions, and the long edges were chamfered. Samples were oriented such that the print direction was perpendicular to the applied load, and the top surface (the final printed layer) was loaded in tension. A total of 3 and 7 testable bars were made from SMP-5f and SMP-10f inks, respectively. SMP-0f printed bars fractured during machining because of the large amount of macroporosity present in these samples and were unable to be tested.

### *3.3.4 Imaging and Analysis*

Optical micrographs of fracture surfaces of flexural specimens were taken with a VHX-5000 digital microscope (Keyonce, Itasca, IL). SEM micrographs of gold sputter-coated flexural fracture surfaces were taken on a Phenom XL SEM (Phenom-World, Eindhoven, Netherlands) at an operating voltage of 10kV.

To visualize the fiber alignment, porosity, and internal microstructure of the composite, printed samples were scanned using X-ray computed tomography (XCT) (Zeiss Group, Versa 520, US). The samples were extracted from the wall of a pyrolyzed rectangular box that was two layers high and one filament thick (~1.3 mm x 0.8 mm) for each of the three printed inks. All XCT scans were acquired using an x-ray source voltage of 140 keV and power of 9 W. The scans were reconstructed from ~1400 projections acquired with 5-second exposure using a 4x magnification detector, resulting in a reconstructed volume of size 2×2×2 $mm^3$ and a voxel size of 2 μm. The reconstructions were denoised using non-local means filters and analyzed using Dragonfly graphics software (Object Research Systems, Montreal, Quebec, CA).

The fiber, crack angular orientation, and pore size in the samples were measured manually using ImageJ open-source software (National Institute of Health, Madison, WI) on 2D images. The line tool was used to trace the location of the fiber or crack. Each angle was calculated by determining the drawn line's angle in reference to the x-axis (perpendicular to print direction). The print direction was represented as 90º, while 0 and 180º were perpendicular to the print direction.

Fiber angles and lengths were collected from 5 XCT image scans from each SMP-5f and SMP-10f samples at different depths into the sample resulting in approximately 974 fibers measured for SMP5-f and 2078 fibers for SMP-10f. Crack angles were measured from the same set of images with 41 cracks measured from SMP-5f and 85 cracks from SMP-10f. Pore size analysis of three representative fracture surfaces from each ink was calculated using the freehand tool in ImageJ to outline each pore for a total of approximately 50 pores per ink. An average major and minor axis were obtained using the fit ellipse measurement to estimate pore size and area %.

X-ray diffraction (XRD) of mortar and pestle ground pyrolyzed specimens was performed using a Panalytical Empyrean diffractometer (Malvern Panalytical Ltd., Malvern, UK). Phase identification was determined using Highscore Plus software (Malvern Panalytical Ltd.).

## 3.4 Results/Discussion

### *3.4.1 Rheology and printability*

Previous studies have established that successful DIW inks are typically shear-thinning, yield-stress fluids, with a $\tau_y$ ≥~200 Pa, and an equilibrium storage modulus ($G'_0$) ≥~$10^4$ Pa [5,6,11,16,60,106–108]. A high $\tau_y$ prevents slumping of the lower layers when loaded by the weight of upper layers in a printed part [11,106,108], while a high $G'_0$ prevents elastic buckling of tall features [16] and excessive sagging of spanning features[5,109]. The rheological behavior of all inks

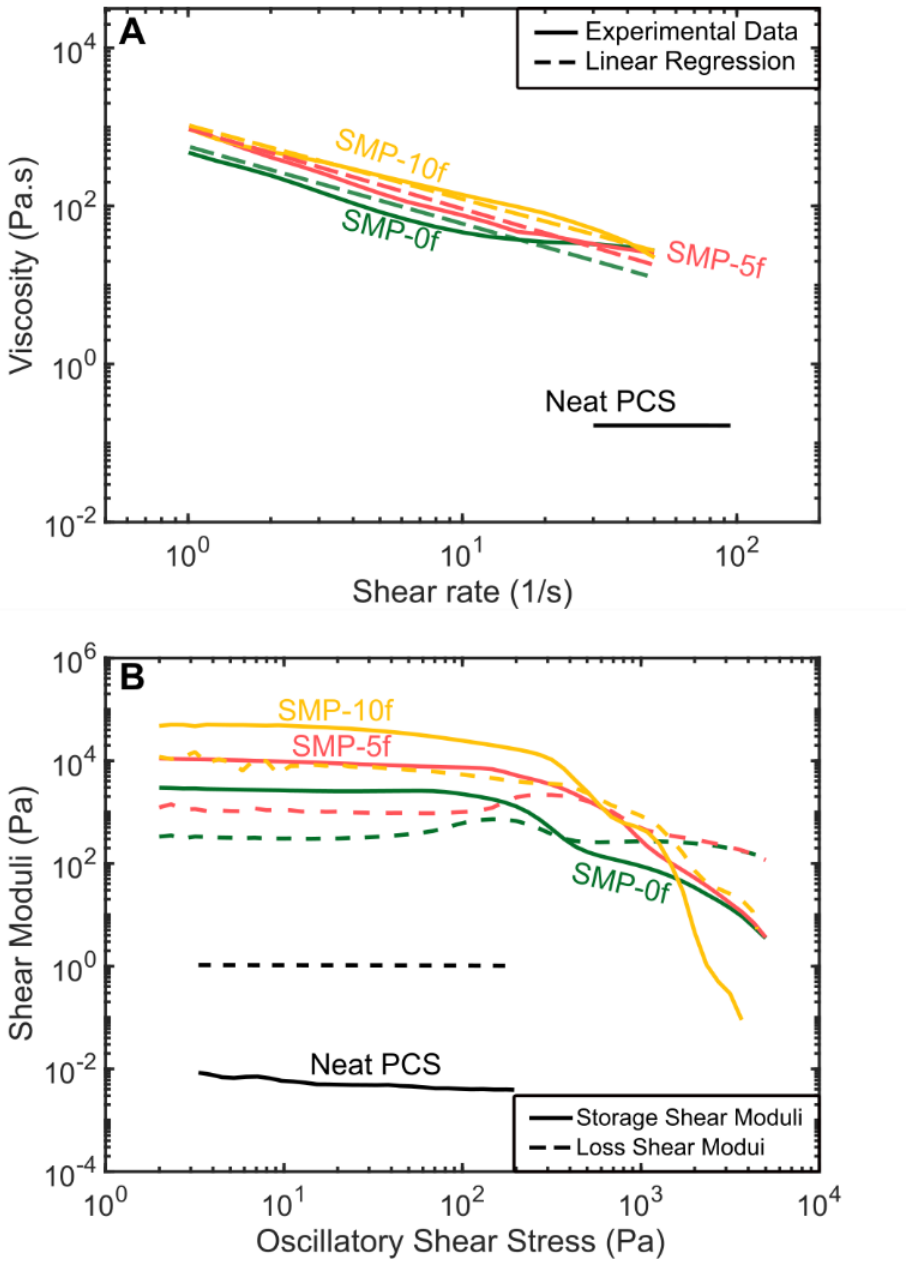


**Figure 3.2: Rheological behavior of PCS based inks. (A) apparent viscosity vs. shear rate. (B) Shear moduli vs. oscillatory shear stress.**

in this study, as well as reference neat PCS, is shown in **Figure 3.2.** The viscosity of neat SMP-10 was probed at higher shear rates than the printable ink formulations due to the sensitivity of the instrument and the low response of the PCS polymer in the specific testing geometry. Here the intent is to compare the general behavior of the base PCS with and without added ceramic filler. The reported viscosity is within the same range as others reported in literature for SMP-10 using parallel plate (e.g. 0.1 Pa•s at 20-100 1/s) [33]. For a more detailed analysis of the SMP-10 rheological behavior it is recommended to use capillary rheometry which is a more accurate test method for low viscosity fluids [110].

The shear-thinning behavior of the inks shown in **Figure 3.2A** was quantified with the power-law fluid model (*Eq. 1.1*). The value of *n* represents the shear rate dependence of the fluid where a shear-thinning fluid, Newtonian fluid, and a shear thickening fluid are $n < 1$, $n = 1$, and $n > 1$, respectively. Linear regression was used to calculate *K* and *n*, and all values for each ink are given in **Table 3.2** along with the $R^2$ values for the regression. All values of *n* are lower than unity and indicate shear-thinning behavior, which is desirable for extrusion. When compared to other inks for DIW, including preceramic polymer-based inks, these *n* values are similar to printable mixtures [5,11,14]. The addition of $ZrB_2$ and $SiC_f$ to the neat PCS impart the desirable shear thinning behavior for material deposition. Additionally, the presence of $SiC_f$ increased the viscosity of the inks over much of the shear rate range probed. This observation is in agreement with

**Table 3.2: Rheological properties of the DIW inks**

| Ink Name | $G'_0$ (kPa) | $\tau_y$ (Pa) | n | K (Pa•s) | $R^2$ |
|---|---|---|---|---|---|
| SMP-0f | 2.54 | 371 | 0.24 | 358 | 0.94 |
| SMP-5f | 8.86 | 586 | 0.04 | 786 | 0.983 |
| SMP-10f | 48.8 | 503 | 0.13 | 950 | 0.989 |

other fiber-containing viscoelastic materials, where fiber-fiber interactions become more prevalent with the addition of fibers, causing an increase in shear-thinning behavior [7,109].

In the case of SMP-0f with the highest content of $ZrB_2$ (47.5 vol.%), shear-thinning is observed before approximately 10 1/s after which there is a plateau then slight increase in viscosity (**Figure 3.2A)**. This behavior may be due to particle jamming in the ink at higher shear rate. Similar behavior is observed in other highly-loaded viscoelastic fluids, where a water-based slurry loaded with silica particles transitions from shear-thinning to shear-thickening at higher viscosities due to particle jamming [111,112]. The lowest value of *n* is observed in SMP-5f, likely due to the decreased $ZrB_2$ loading (42.2 vol.%) and the addition of fibers which align during shear flow. While there is a similar reduction in the $ZrB_2$ loading of the SMP-10f ink (38.8 vol.%), an increase in the *n* value is observed and could be attributed to the near double fiber content. This greater volume of fibers in the ink is most likely above some critical amount for jamming associated with the percolation threshold of the fiber network. Limited work has been done to thoroughly analyze the rheological properties of highly-loaded particle and fiber viscoelastic fluids as a function of fiber and particle content for comparison. One such example from Sidauoi *et al*. on suspensions of particles and fibers at varied loadings found a similar critical fiber volume fraction (of 4 vol.%) for a transition to shear-thickening behavior that was nearly independent of particle concentration [113].

**Figure 3.2B** shows the measured storage and loss moduli (G' and G", respectively) in the oscillatory stress range probed. In the linear viscoelastic region (LVER), the G' value remains at a nearly constant value. This constant modulus value is known as the plateau or equilibrium modulus ($G'_0$). As stress increases, the weak particle network breaks down and the storage modulus drops considerably. At even higher stresses, the storage modulus drops below the loss modulus, resulting in liquid-like behavior. The shear yield stress is associated with the breakdown of the particle network within the fluid and can be characterized in various ways [114]. Here, the $\tau_y$ is approximated as the crossover point between G' and G". Rheological parameters for the present inks are summarized in **Table 3.2**. While the equilibrium moduli for SMP-0f and SMP-5f are somewhat lower than typical DIW inks, indicating larger structures may be unstable, the equilibrium modulus for SMP-10f and the shear yield stress values for all inks are comparable to other successful DIW inks [5,11,15,54]. With the addition of any amount of fiber, there is an increase in $G'_0$ and $\tau_y$. While the $\tau_y$ for SMP-5f is the largest value for all three inks, the difference between both SMP-5f and SMP-10f $\tau_y$ values is negligible.

A possible source of error is in the gap size used for the parallel plate measurements. The fibers in both the SMP-5f and SMP-10f inks are approximately half the 0.5 mm gap size (~0.25 mm), meaning that the fibers could have caused interference with the measurements. Future work will study the effect of different gap sizes on rheology measurements.

An estimate of the strain rates experienced by the ink in the nozzle can be made by assuming a fully-developed flow in a straight pipe. For a shear-thinning fluid, the maximum shear rate is given by [15]:

$$\dot{\gamma} = \frac{4Q}{\pi r^3}\left(\frac{3n+1}{4n}\right) \quad (3.1)$$

where *r* is the radius for the nozzle, *Q* is volumetric flow rate, and *n* is the flow index. In this case, *Q* = 9.87 $mm^3/s$, r = 0.42 mm, and *n* is set to 0.14 to represent the average value for all three inks. The resulting maximum shear rate is 430 1/s, well above the shear rates that were able to be measured with parallel plate rheometry. Despite this, the measurements made here provide a helpful comparison to the many DIW inks that have been described in the literature and characterized in a similar manner.

During deposition, all three inks were easily extruded into uniform filaments that could support the weight of additional layers without slumping or collapse of the wall structure. SMP-0f behaved most reliably as nozzle clogging did not occur during extrusion. Approximately 15 to 20% of nozzles clogged during printing for the SMP-5f and SMP-10f inks, respectively. The increase in fibers from SMP-5f to SMP-10f did show a small increase in the number of nozzles clogged and was most likely caused by the increased fiber interactions. To understand our inks' specific nozzle clogging mechanism, Croom et al. analyzed a nozzle clogged with SMP-5f ink and showed misalignment of $SiC_f$ directly at the nozzle tip [115]. Croom et al. hypothesized that changing the nozzle geometry to a smoother, monotonically tapered nozzle can help improve the flow profile and reduce fiber

misalignment and clogging events during deposition [115]. The focus of future studies will be on enhanced understanding of the interplay between the PCS polymer and the added $ZrB_2$ powder and $SiC_f$. This includes more analysis of the surface functionalization and subsequent particle interactions of the powder and fiber in the polymer medium. This enhanced understanding would enable the increased fiber loading necessary for improved mechanical performance all while maintaining or improving rheology for printing. Other changes that could improve printability include: adding rheological modifying chemicals specifically parameterized for PCS polymers (solvents, dispersants, binders, etc.) [116], and gaining a better understanding of how the particle size of $ZrB_2$ directly affects the inks viscosity.

### *3.4.2 Printed Microstructure and Fiber Alignment*

Optical images of printed, pyrolyzed components made from all three inks are shown in **Figure 3.1C-D**. Phase analysis of pyrolyzed components is shown in the x-ray diffraction analysis in **Figure 3.8** (in appendix). While there is some degree of crystallization expected for the polymer-derived SiC-based matrix, the spectrum of the SMP-0f is dominated by the high crystallinity of the $ZrB_2$ phase. The spectra for SMP-5f and SMP-10f both contain β-SiC peaks from the fiber additions.

Selected XCT images of 2-layer, pyrolyzed specimens printed using each of the three inks are shown in **Figure 3.3,** where the print direction is from the bottom of the image to the top. Circle (i) in **Figure 3.3A** (SMP-0f**)** highlights an

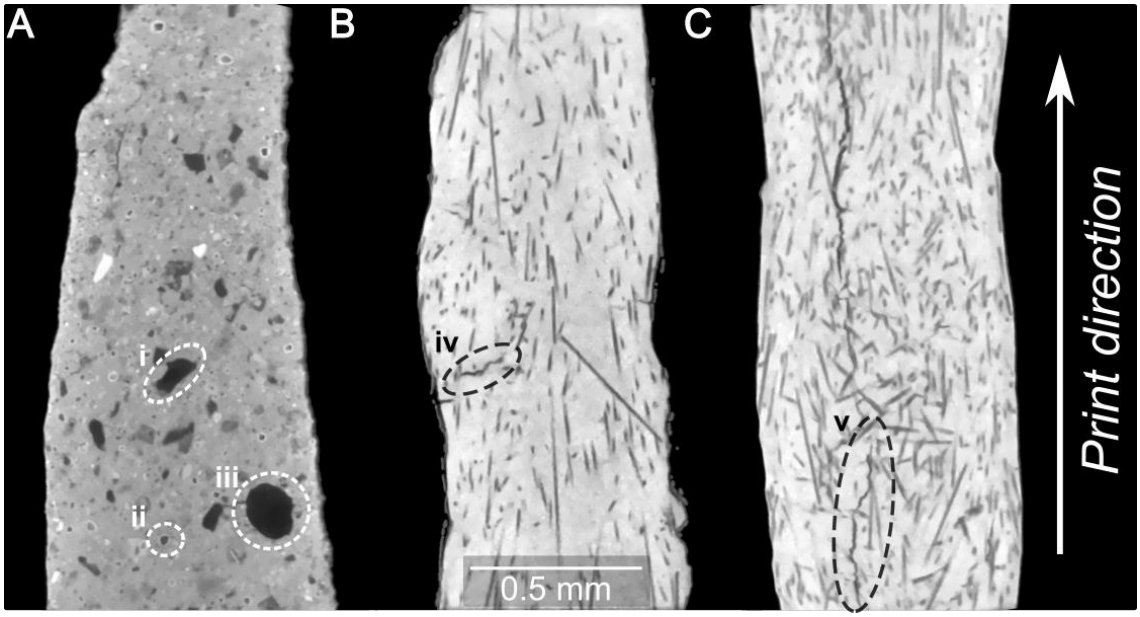


**Figure 3.3: XCT scans of printed and pyrolyzed 2-layer specimens made from (A) SMP-0f, (B) SMP-5JJJf, and (C) SMP-10f. In (A), Dotted circle (i) denotes examples of large ZrB2 particles circles (ii) and (iii) denote voids in SMP-0f. Circle (iv) highlight**

example of large spheroidal $ZrB_2$ particles. $ZrB_2$ particles are present in **Figure 3.3 B** and **C,** like they are in **Figure 3.3A.** However, fiber-containing images have a different level of contrast that was used during scanning, thereby making the $ZrB_2$ difficult to see. Defects, including porosity and cracking, of varying shape and size scale were observed in pyrolyzed components from all 3 inks. **Table 3.3** outlines these defects as categorized by the processing step in which they likely originate. Probable causes are suggested, along with potential mitigation strategies and quantification methods.

Broadly, there are two main types of defects observed in the microstructures of the printed composites: those with spheroidal morphology that likely formed under the influence of surface tension at a point when the PCS was at least partially flowable, and sharp, flat cracks that must have formed once the PCS had become rigid and brittle after thermal cross-linking. The crack-like defects were not observed in any as-cured specimens, so these must have arisen during the pyrolysis process, when the PCS matrix is undergoing considerable mass loss and constrained shrinkage (constrained by the fibers and particles), or during the cool-down stage, where the thermal expansion mismatch between the SiC fibers (~4.5 x $10^{-6}$ $K^{-1}$), the $ZrB_2$ particles (~7.5 x $10^{-6}$ $K^{-1}$), and the amorphous polymer-derived ceramic (PDC) matrix puts the matrix and particles in residual tension [77]. Within the population of spheroidal pores, larger pores of >~80 μm in diameter were observed with somewhat irregular contours, (e.g. circle iii in **Figure 3.3A**),

**Table 3.3: Steps in DIW and ceramic conversion of preceramic inks with associated defects observed in pyrolyzed samples**

| Processing step | Defect location | Defect geometry | Potential cause | Mitigation strategy | Potential quantification methods |
|---|---|---|---|---|---|
| Loading syringe barrel | Intra-filament | Circular smooth | Entrapped air in the syringe barrel | Centrifuging /planetary mixing syringe barrel before deposition [11,117] | Visual inspection; XCT of as-loaded syringe barrel |
| Deposition | Filament weld lines | Circular, cylindrical, or ellipsoidal smooth | Intermittent nozzle clogging; path/layer spacing too large | Larger nozzle; ink refinement; reduce layer height or path spacing | Optical microscopy; *in situ* pressure monitoring; *in situ* machine vision analysis |
| Curing | Inter- and intra-filament | Ellipsoidal with irregular contour | Boiling of low-molecular-weight oligomers | Refine synthesis process or remove low molecular weight species through chemical initiator or [34] or thermal pretreatment [33] | Thermogravimetric analysis; XCT |
| Pyrolysis | Inter- and intra-filament | Thin cracks | Constrained volumetric shrinkage of the polymer during conversion | Increase ceramic yield of the polymer; isotropic passive or active fillers[22,39]; infiltration | Metallography; *in situ* microscopy during pyrolysis [118] |

along with smaller (<~20 μm in diameter) round pores (e.g. circle ii in **Figure 3.3A**). These voids were only observed in samples after both curing and pyrolysis and are attributed to either the volatilization of low-molecular-weight oligomers from the PCS during curing [33,98] or the entrapment of air in the ink during the loading process [7,15]. The lack of larger-scale, bulk processing of PDCs reported in literature makes it difficult to directly compare these porosity results. In fact, it's virtually impossible to obtain a dense PDC unless dimensions are kept below a few hundred micrometers [19]. Reported studies on bulk PDC processing using DIW have kept feature sizes small through utilizing much smaller nozzle diameters (0.160 – 0.410 mm) than the 0.840 mm size used here [7,14,90,119].

Matrix cracking was observed in all fiber-containing specimens after pyrolysis. The average directionality of the cracks changed from relatively perpendicular to the print direction in SMP-5f specimens (circle iv, **Figure 3.3B**), to aligning with the print direction in SMP-10f (circle v, **Figure 3.3C**). Interestingly, the perpendicular cracks in SMP-5f almost always appeared on the outer surface of the printed filament and were shorter in length than the parallel cracks observed mostly in the interior of the SMP-10f samples. Constrained shrinkage in the length direction would support the expectation of perpendicular surface cracks in the SMP-5f samples. The curious change in orientation with increased fiber loading in SMP-10f may be due to the decrease in fiber alignment in these samples and/or an increase in internal porosity. These internal defects can act as stress initiators for cracks to propagate to relieve the matrix stresses from constrained shrinkage

and/or CTE mismatch. A detailed crack angle analysis calculated from 10 XCT slices and 126 total cracks highlight the different crack orientation in the two composites (**Figure 3.9, in appendix**). Clearly, more research in this area is warranted to understand and mitigate this cracking phenomenon.

Histograms of the measured fiber angles relative to the print direction for SMP-5f and SMP-10f pyrolyzed prints with a bin size of 3.6° are shown in **Figures 3.4A** and **B,** respectively. For each measurement, 90° is along the print direction, while 0° and 180° are perpendicular to the print direction. **Figure 3.3B** and **C** show representative images of measured fibers for the histograms shown in **Figure 3.4**. A Kolmogorov-Smirnov goodness of fit test (i.e., KS test, MATLAB code `kstest2`) was used to determine that the two fiber angle sample sets for SMP-5f and SMP-10f differ significantly and returned a 1, meaning they cannot be fit to the same distribution. The average fiber angles were 89.2 ± 20.2 and 83.0 ± 32.7 for SMP-5f and SMP-10f, respectively, where the larger standard deviation in the SMP-10f fiber angle measurements corresponds to the broader distribution of fiber orientation shown in **Figure 3.4B.**

This decrease in alignment may be attributed to increased fiber-fiber interaction in the more highly-loaded ink. This phenomenon has been observed experimentally in the literature in simple flow studies [120], additive manufacturing of polymer matrix composites [115,121], and in highly resolved numerical simulations of confined flow of fiber suspensions in tapered DIW nozzles [122].

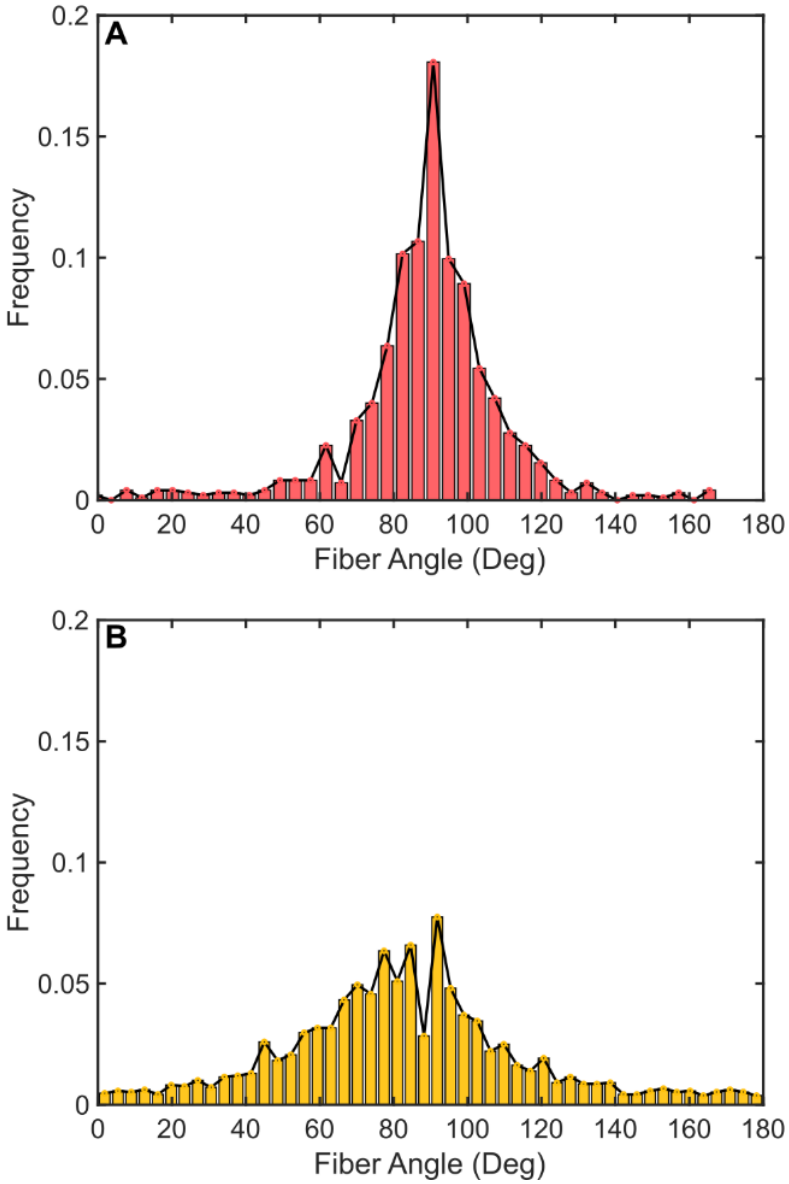


**Figure 3.4: Histograms of fiber angles measured from (A) SMP-5f and (B) SMP-10f prints. Representative images of XCT images used to measure these angles are shown in Figure 3.3.**

Specifically, Folgar and Tucker studied the behavior of 1 - 15 vol.% nylon fibers in silicone oil and observed that fiber-fiber interaction disrupts the Jeffrey orbitals of the individual fibers and results in a broader distribution of steady-state fiber orientation than would be expected for dilute suspensions. Tekinalp et al. reported a 5% decrease in alignment along the print direction in fused deposition modeling structures when fiber content was increased from 10 to 40 wt.% [121].

All linear shrinkage measurements between as cured and pyrolyzed specimens are shown in **Table 3.4**. For the SMP-0f samples the height and length shrinkage only differ by 1.3%. Conversely, both fiber-containing inks had more anisotropic shrinkage with similar values (3.6 - 4%) for both height and width directions, while the length direction shrank less than 1%. Near zero shrinkage in the length direction is observed in these samples due to fiber alignment along the print direction. The linear shrinkage from the polymer-to-ceramic conversion of unfilled PCS is expected to be 20 - 30% [19], but the presence of ~50 vol.% solids drastically reduces the total shrinkage of the composites through rigid constraint. While this is beneficial to the fabrication of near net shape UHTCMCs, the rigid network also contributes to the formation of porosity [39]. The density of pyrolyzed and printed specimens was 3.8 ± 0.1, 4.0 ± 0.1, and 2.7 ± 0.2 for SMP-0f, SMP-5f, and SMP-10f, respectively. The decrease in density from SMP-5f to SMP-10f is likely due to the large amount of porosity present in the samples post-pyrolysis. The porosity will be discussed in subsequent sections.

**Table 3.4: Linear shrinkage of pyrolyzed flexural bars. Number of samples measured for linear shrinkage were 3, 8, and 7 for SMP-0f, SMP-5f, and SMP-10f.**

| Ink Name | Shrinkage in height direction (%) | Shrinkage in width direction (%) | Shrinkage in length direction (%) |
|---|---|---|---|
| SMP-0f | 5.0±1.1 | 4.8±0.7 | 3.7±0.1 |
| SMP-5f | 3.6±0.4 | 4.0±0.9 | 0.4±0.2 |
| SMP-10f | 3.6±0.1 | 4.6±1.1 | 0.5 ±0.2 |

### *3.4.3 Properties of Pyrolyzed Prints*

Flexural specimens were printed with all three inks, then pyrolyzed and tested in 3-point flexure, with printed filaments being deposited along the length of the bar. Optical micrographs of the overall fracture surface of the SMP-5f and SMP-10f bars in **Figure 3.5** show increased large-scale porosity with increasing fiber content. SEM of the SMP-5f and SMP-10f fracture surfaces show evidence of some fiber pullout (**Figure 3.5C** and **D**), which is an indicator of a weak fiber-matrix interface and a known toughening mechanism [79,80]. Future work will focus on modification of the fiber-matrix interface (i.e., fiber coatings) to increase the amount of fiber pullout to improve fracture toughness.

The average fracture strength of the SMP-5f and SMP-10f pyrolyzed bars were 51.9 MPa and 38.3 MPa, respectively. The fracture strength is low compared to other dense $ZrB_2$ and $SiC_f$ based UHTCMCs (240 - 600 MPa) [79], due to the prevalence of large pores and defects (**Figure 3.5 A** and **B**). The average pore major and minor axis for SMP-5f was 588.1 ± 53.7 µm and 223.3 ± 23.8 µm, respectively. The average pore size for SMP-10f was slightly larger at 667.2 ±108.5 µm for the major axis and 276.1 ± 25.0 µm for the minor axis. The pore area % was calculated by dividing the total measured pore area by the area of the fracture surface. These values were 11.16 ± 5.34% for SMP-5f and 24.63 ± 5.58% for SMP-10f. The slightly lower size and amount of porosity in SMP-5f may explain the higher strength over SMP-10f, but both sets were severely limited by this prevalent porosity. Due to the complex shape and arrangement of the porosity, it

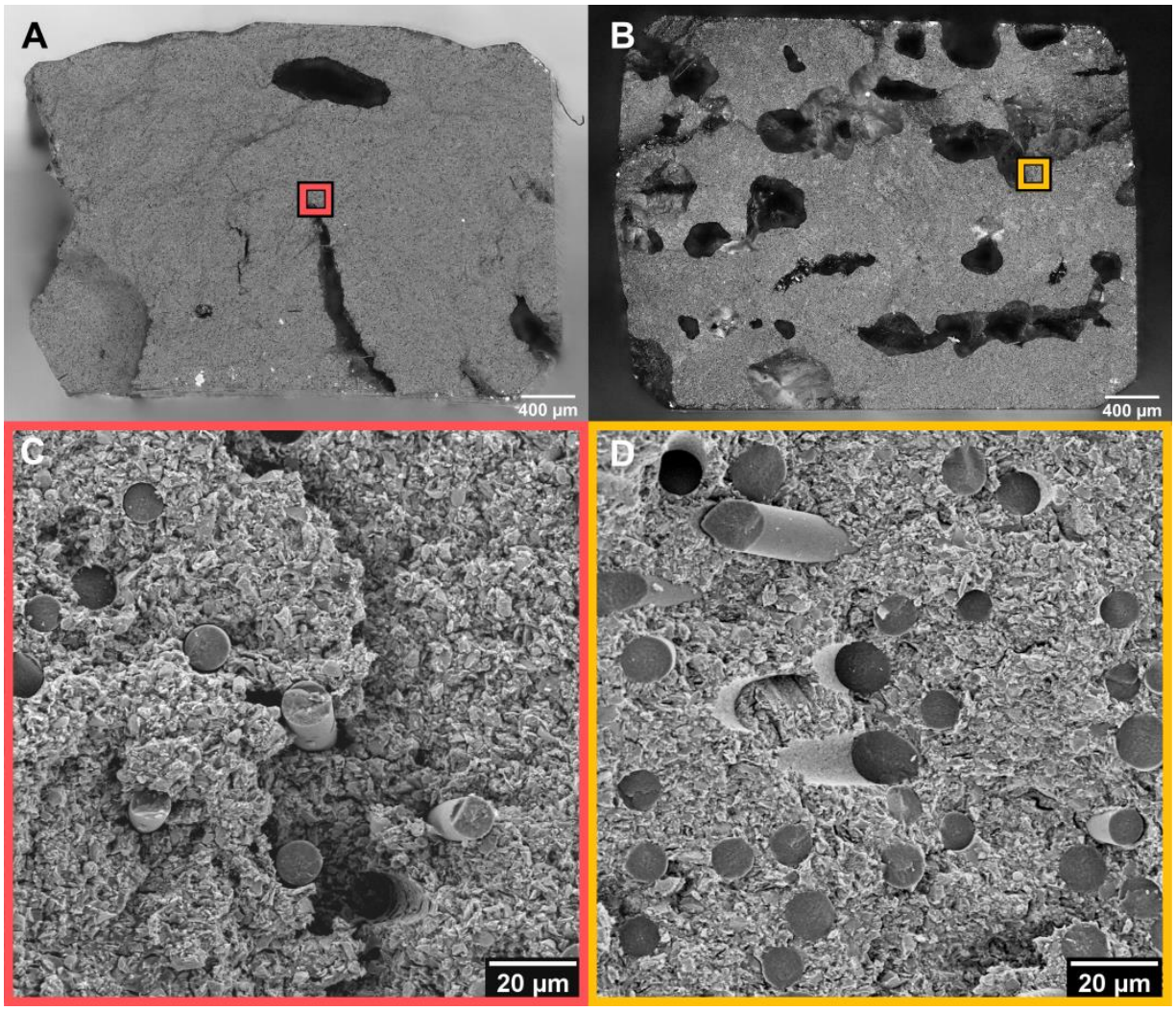


**Figure 3.5: Optical images of the fracture surface of (A) SMP-5f and (B) SMP-10f flexural bars. (C) and (D) show SEM micrographs of the highlighted portions from (A) and (B).**

is not feasible to infer the strength of a fully dense, pore-free printed composite. It is also important to note that these values are an overestimation of the total sample as the failure is most likely to occur at the weakest cross-section. Additionally, the pore size and amount played a role into the overall density measurements. The density, based upon 5 samples each, of SMP-0f, SMP-5f, and SMP-10f were 3.8 ± 0.1, 4.0 ± 0.1, and 2.7 ± 0.2 respectively. The large pore area increase from inks made with SMP-5f to SMP-10f could have influenced the overall measurement method and other density testing methods are needed and will be performed in subsequent work.

To improve upon the printed composites' mechanical strength, a key area of future study is to better understand the observed macro-scale porosity in printed polymer-derived ceramics and the shrinkage cracking that occurs during pyrolysis. **Table 3.3** outlines some of the current methods to reduce porosity in polymer derived ceramics, including polymer-infiltration and pyrolysis (PIP) processing [99], thermal pretreatment [98], and catalyst addition [123,124]. PIP has been frequently used in polymer derived ceramic composite structures to decrease the amount of porosity present in the final product by infiltrating preceramic polymer into the composite via a vacuum system with multiple infiltration steps [99,100]. PCS has been used to infiltrate UHTC-based woven mats and has shown up to an 11 percentage point open porosity reduction after multiple infiltration steps [99]. However, little work has been done with AM based methods [93]. Initial trials on the infiltration of PCS into printed specimens made of SMP-5f and SMP-10f show

a mass increase of 1.6% and 6% after 1 reinfiltration cycle, respectively. The minor increase in mass is attributed to the fact that primarily closed porosity was observed in the pyrolyzed samples (e.g., **Figure 3.3A - B**). Post-treatment of polymer-derived components to 1800ºC has been shown to build interconnected pores more favorable for PIP [93] and could be explored in future studies.

## 3.5 Conclusions

In this study, we have shown an example of UHTCMCs fabricated by DIW. Inks were developed with high $ZrB_2$ powder content and SiC fibers, which effectively modify the flow properties of the neat PCS polymer to impart favorable printing behavior for DIW. These inks were used to print complex-shaped UHTCMCs with preferential alignment of the chopped SiC fibers along the print direction. An increase in porosity area fraction and size, along with a lower degree of fiber alignment, was observed in the pyrolyzed parts with the highest fiber content (10 vol.% vs. 5.75 vol.%). With increased fiber content, fiber misalignment and a change in orientation of shrinkage cracking were observed. Defects were prevalent in all pyrolyzed components, resulting in limited mechanical performance. Outgassing and constrained shrinkage during preceramic polymer curing and pyrolysis, respectively, were identified as the main culprits. These thermal processing induced defects are a major limiting feature for AM of bulk polymer-derived ceramic composites and will be the focus of future studies. We have identified mitigation strategies to explore to address these defects, including

polymer pretreatment, incorporation of active fillers, and/or reduction of PCS content.

# Appendix

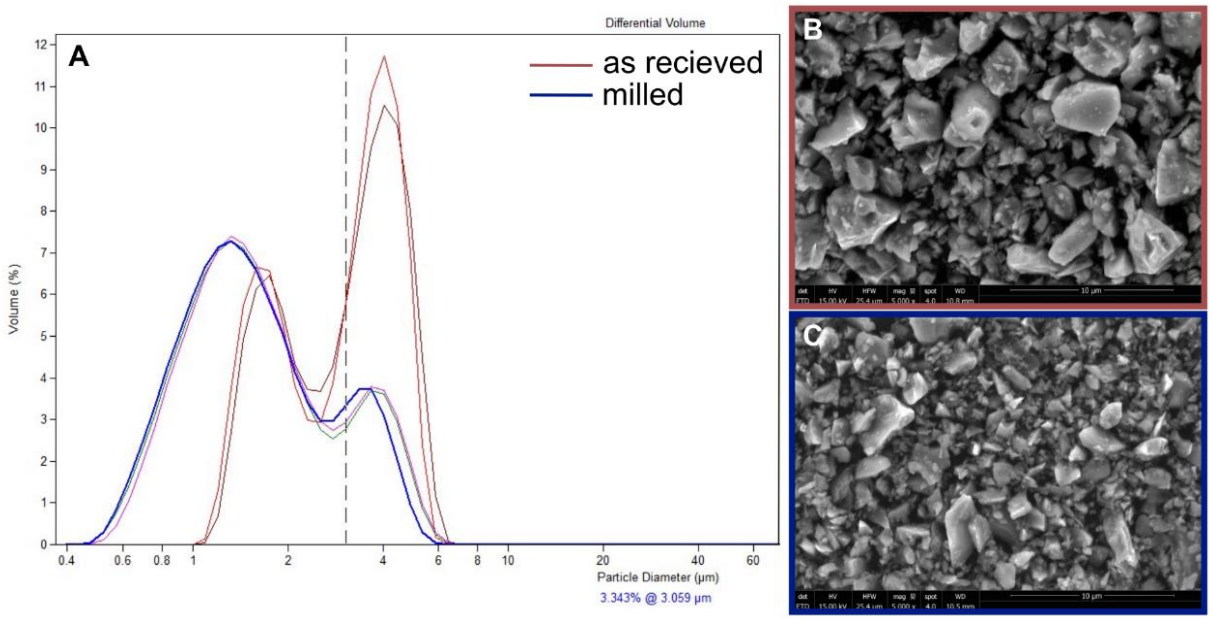


**Figure 3.6: (A) Granulometric distribution of ZrB2 and corresponding SEM images of the (B) as received and (C) milled powder portions.**

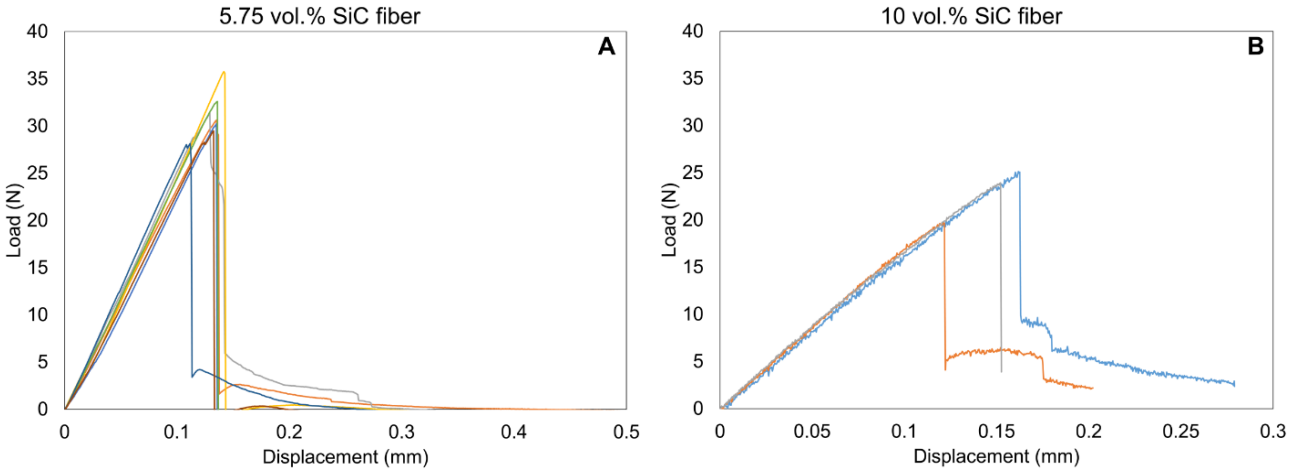


**Figure 3.7: Load vs. Deflection for (A) SMP-5f samples and (B) SMP-10f**

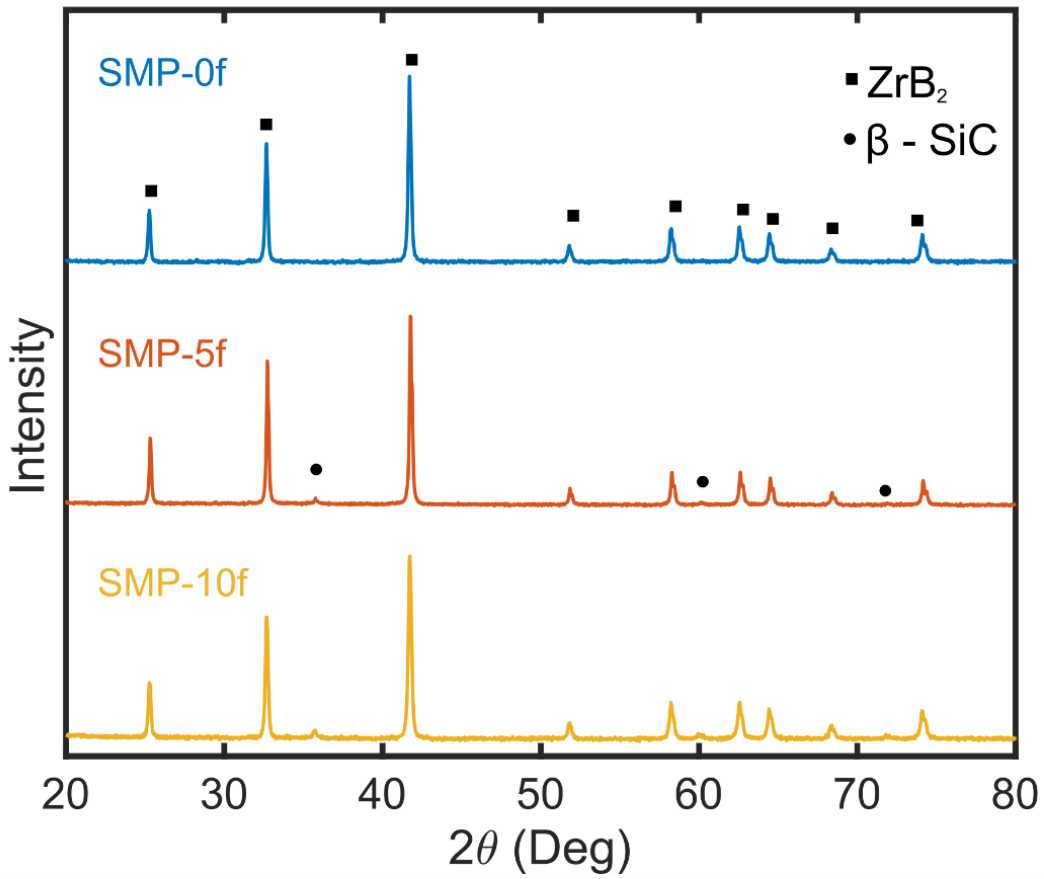


**Figure 3.8:XRD pattern of printed samples post-pyrolysis.**

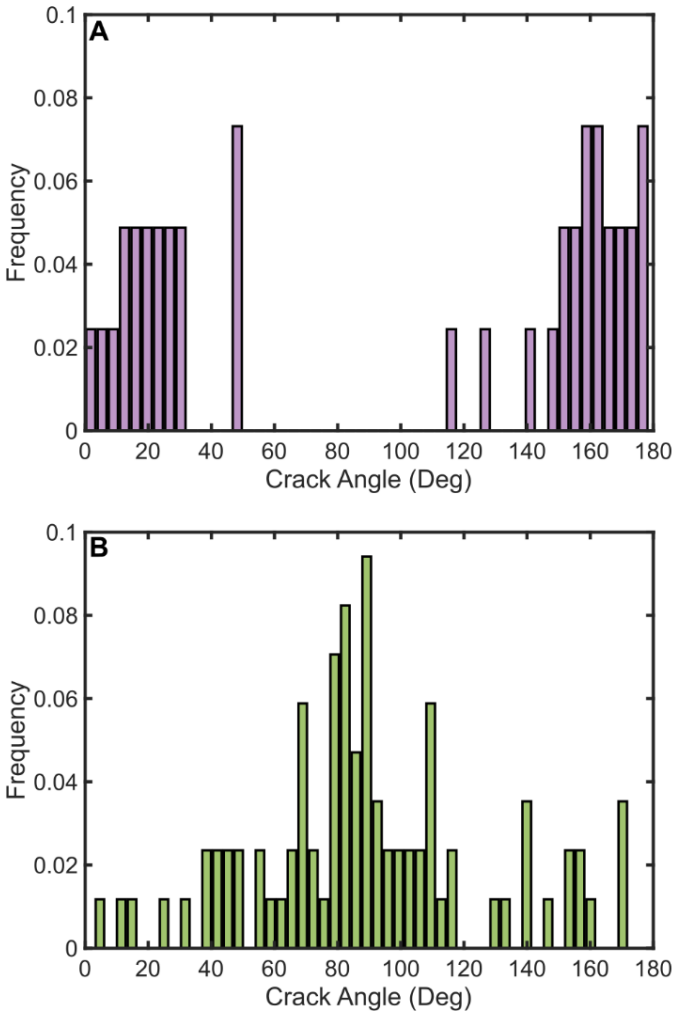


**Figure 3.9: Analysis of crack angle for (A) SMP-5f, and (B) SMP-10f. 90° corresponds to the print direction, and angle orientation was organized into 50 bins. Cracking observed in the SMP-5f is predominantly perpendicular to the print direction. SMP-10f cracks trended to align parallel to the print direction. A total of 41 and 85 cracks were measured for SMP-5f and SMP-10f, respectively.**

# CHAPTER 4 SIZE EFFECTS IN 3D-PRINTED POLYMER-DERIVED CERAMIC MICRORODS

## 4.1 Abstract

Preceramic polymers are of interest for use in many manufacturing techniques such as injection molding, ceramic fiber infiltration, and additive manufacturing. However, off-gassing of low molecular weight oligomers can occur when these polymers cure, leading to porosity in the cured part. Microrods of varying sizes were fabricated via direct ink writing (DIW), an additive manufacturing technique, with two inks comprised of polycarboslane (PCS), zirconium diboride ($ZrB_2$), and fumed alumina (FA). Each microrod was 25 mm in span length and nominally either 450, 634, 979, 1346, or 1702 μm in diameter. The amount of observed porosity was found to increase with increasing sample size. Failure strength was measured through 3-point flexural testing for microrods printed with each ink composition and nozzle size. For a given nozzle size, the microrods made with FA-containing ink possess higher strength than those without FA. Additionally, with increasing nozzle size, strength decreases for both inks. Weibull strength analysis was performed on each group of microrods and shows that the addition of FA increases Weibull modulus from 4.63 ± 1.56 to 9.35 ± 0.601. In conjunction with optical microscopy, this analysis indicates two distinct flaw populations in the printed materials, one which arises during the curing step and one which arises during pyrolysis of the larger specimens.

## 4.2 Introduction

Polymer-derived ceramics (PDCs) are a class of ceramic materials formed from the conversion of polymeric precursors to inorganic ceramics. This class of materials has been of interest in recent years because of their ability to be formed into complex structures, with most of the commercially available polymers being precursors to SiOC, SiCN, SiC, and $Si_3N_4$ materials. While still in the polymeric phase, the precursors behave similarly to thermoset polymers that thermally cross-link [19,21]. During the cross-linking phase, many low-molecular-weight oligomers and various hydrocarbon gasses (methane, ethanol, ammonia, etc.) diffuse out of the formed polymer [33,98], commonly referred to as off-gassing, leading to porosity development in the part that can be detrimental to the strength and performance of the final part [33,125].

Previous work has explored porosity development in the AM technique of DIW. DIW-printed structures explored in Chapter 3 showed that the polycarbosilane-based inks develop large porous networks after curing [125]. The suggested mitigation methods included thermal pretreatment, addition of a chemical initiator, or synthetic refinement of the polymer. Apostolov et al. explored the thermal pre-treatment method on a polycarbosilane and a polysilazane and showed that many of the low-molecular-weight oligomers present in the polymer could be removed with a combination of heat and vacuum [33]. D'Elia et al. focused on the addition of a chemical initiator, dicumyl peroxide, to a polysilazane and showed that many low molecular weight oligomers and methyl/vinyl groups could

be pulled off prior to thermal cross-linking [35]. However, a description of how these mitigation strategies influence porosity in cured and pyrolyzed materials is limited.

In the context of AM, there are few, if any, studies at present that investigate how print parameters affect the development of porosity in preceramic polymer inks. Franchin et al. measured mechanical properties of individual preceramic polymer filaments [8], and others have shown properties of printed 3 point and 4 point flexural bars [126], but no research has studied how sample size affects the development of porosity and mechanical strength in polymer-derived ceramics. Traditionally, ceramic test specimens made with conventional ceramic processing methods with different volumes and mechanical strengths have been analyzed through Weibull statistical analysis [127,128]. Intrinsic and extrinsic flaws usually dictate the brittle failure of ceramics, and with increased material volume, there is an increased likelihood of a strength-limiting flaw being present in a ceramic. By using a Weibull distribution fit, the effects of flaw size distribution and sample volume can be accounted for by determining a Weibull modulus, or a measure of the sample's likelihood of failure [128].

In this work, ceramic microrods of varying diameters are printed using polycarbosilane (PCS)-based inks loaded with, $ZrB_2$ and fumed $Al_2O_3$ (FA). The effects of deposition nozzle diameter and ink composition are characterized and analyzed with Weibull analysis. Porosity content is quantified through area

analysis, and the strength of individual microrods is measured with 3 pt. bend testing.

## 4.3 Experimental

### *4.3.1 Materials and Mixing*

SMP-10 (Starfire Systems Inc., Schenectady, NY), an allylhydridopolycarbosilane, or simply polycarbosilane, was used as the base for all DIW inks. The PCS polymer has a polydispersity index of 5.544, thermally crosslinks without catalyst at 250°C, yields 72-78 wt.% amorphous SiC after pyrolysis, and begins to form SiC crystallites at 1250°C [33,95]. Two inks were developed with SMP-10, one containing $ZrB_2$ and FA, and the other containing only $ZrB_2$. These formulations will be designated SMP-FA and SMP-00, respectively **Table 4.1** summarizes the compositions of each ink.

The FA (Evonik Industries, Aerosil 805C, Essen, Germany) and $ZrB_2$ (H.C. Stark GmbH, Grade B, Goslar, Germany) had average particle sizes of 13 nm [129] and 3.6 µm, respectively [125]. SMP-00 ink is similar in composition to the SMP-0f described in Chapter 3, with the only difference being that all $ZrB_2$ used in the SMP-00 was unmilled. The $ZrB_2$ amount for SMP-FA was kept above 40 vol.% to provide a comparable ink composition to SMP-00 and other inks from Chapter 3.

Both inks were mixed with a planetary mixer (FlackTek, Inc. Landrum, SC) in 98-mL plastic containers under vacuum of 100 mbar. $ZrB_2$ was added to the PCS polymer in two equal parts to reach the desired loading and was mixed at 1500 rpm for 2 min after each addition. For SMP-00, the sidewalls of the mixing cup

**Table 4.1: Ink compositions for microrod printing**

| Ink Name | SMP-10 [vol.%] | $ZrB_2$ [vol.%] | Fumed $Al_2O_3$ [vol.%] |
|---|---|---|---|
| SMP-00 | 52.5 | 47.5 | 0.00 |
| SMP-FA | 51.7 | 42.4 | 5.95 |

were scraped down with an offset spatula and mixed once more at 1800 rpm for 2 min. FA was added to the SMP-FA ink in 3 equal increments followed by mixing for 2 min at 1800 rpm after each addition. The gradual introduction of $ZrB_2$ and FA aided in the mixing and incorporation of the ceramic powders into the PCS polymer.

### *4.3.2 Rheological Characterization*

The rheological properties of each ink were measured using a Discovery Hybrid Rheometer (DHR-2, TA Instruments, New Castle, DE) using a 40 mm diameter, flat platen, and a Peltier base. Testing was performed at 25°C with a gap size of 1 mm.

All tests included a 2 min. pre-conditioning step at a constant shear rate of 0.1/s followed by a 2 min. rest to allow the material to equilibrate. Oscillatory stress sweeps were conducted between 50 – 7000 Pa for both inks. In addition, flow sweeps were measured over a range of 0.01 – 3 1/s for both inks.

### *4.3.3 Printing and Pyrolysis*

Microrods were printed using five different nozzle sizes with diameters of 450, 634, 979, 1346, and 1702 µm. A custom DIW platform comprised of a 3-axis gantry (ShopBot Tools, Inc., Durham, NC), solenoid valves, and a voltage-controlled air pressure regulator was used for deposition. Inks were manually loaded into 10 cc syringe barrels (Fisnar Inc., Wayne, NJ) with a SpeedDisk (FlackTek, Inc. Landrum, SC), which reduced the amount of air in the syringe. Syringes were loaded into a HP-10cc air pressure adapter (Nordson EFD., Westlake, OH) then

mounted to the gantry system. The print head was raised to a height of 0.75 times the nozzle diameter above the substrate. Microrods 32 mm in length were printed on glass slides coated with a PTFE-coated aluminum foil (Bytac, Saint-Gobain Performance Plastics, Worcester, MA). Custom print paths for the microrods were made from g-code scripts written in Scilab open-source software (ESI Group, France). For all nozzles used, a print speed of 20 mm/s was specified. A summary of the required pressures for each combination of ink and nozzle size is shown in **Table 4.2**.

Printed samples were cured in air with a two-stage process. The first stage was a ramp-up to 167°C at 1°C/min, hold for 1 hr., then back down to room temperature. The second stage was a ramp-up to 230°C at 1°C/min, hold for 1 hr., then back down to room temperature. The two-stage curing cycle was used to prevent the adhesive backing in the Bytac film from degrading and affecting curing. Additionally, curing in air introduced oxygen into the final cross-linked polymer and may have caused oxides to form after ceramic conversion. Pyrolysis was performed in a tube furnace (CM Furnaces Inc., 1830-10 VF, Bloomfield, NJ) with flowing argon at a rate of 5.2 liters per min (lpm). The pyrolysis schedule was as follows: 1°C/min to 1200°C with 1 h holds at 300, 450, and 600°C and 2 h holds at 800 and 1200°C on the ramp-up, then cooled to room temperature at 5°C /min. Both curing and pyrolysis schedules were based upon previous thermal treatments of the PCS polymer [33,98].

**Table 4.2: Summary of pressures used for both inks with varying nozzle sizes**

| Nozzle Diameter [µm] | SMP-00 pressure [kPa, psi] | SMP-FA pressure [kPa, psi] |
|---|---|---|
| 450 | 2758, 400 | 2758, 400 |
| 634 | 2068, 300 | 1793, 260 |
| 979 | 1931, 280 | 1379, 200 |
| 346 | 1655, 240 | 1048, 152 |
| 702 | 1379, 200 | 1048, 152 |

Thermogravimetric analysis (TGA) and differential scanning calorimetry (DSC) of uncured inks were performed on a Q500 TGA (TA Instruments, New Castle, DE) and Q60 DSC (TA Instruments, New Castle, DE) instruments, respectively. In addition, TGA and DSC of cured material were performed on a simultaneous thermal analyzer (SDT) Q600 (TA Instruments, New Castle, DE).

Flexural properties of pyrolyzed microrods were measured on the same Discovery Hybrid rheometer that performed the parallel plate rheometry, but with a 3pt. bend fixture. A span of 25 mm and a crosshead speed of 0.01 mm/s were used. Vickers microhardness testing was conducted on polished cross-sections of printed, pyrolyzed bars using Wilson VH1202 microhardness tester (Buehler, Lake Bluff, Illinois) with a 0.2 kg load and 10 s dwell.

### *4.3.4 Imaging and Analysis*

Optical images of fracture surfaces of the microrods and porosity area percentage measurements on the bottom surface of fractured microrods were taken with a VHX-5000 digital microscope (Keyence, Itasca, IL). The second moment of area about the x-axis, $I_x$, of fracture surfaces was calculated by using a plug-in for the open-source software, ImageJ (National Institute of Health, Madison, WI) called MomentMarcro (John Hopkins School of Medicine, Baltimore, MD). Weibull analysis of fracture strength was performed with custom scripts in MATLAB software (Mathworks, Natick, MA), and Weibull moduli were found by performing a least-squares fit. SEM micrographs of gold sputter-coated flexural

fracture surfaces were taken using an Auriga Crossbeam FIB/ SEM (Zeiss Group United States).

## 4.4 Results and Discussion

### *4.4.1 Rheology and printability*

DIW inks characteristically exhibit a high degree of shear-thinning, yield stress behavior ($\tau_{y,} \geq 200$ Pa), and an equilibrium storage modulus ($G'_0$, $\geq 10^4$ Pa) [5,6,11,16,54,60,106–108]. High $\tau_y$ indicates that a layer of ink will support the weight of subsequent layers [11,16], while sufficiently high $G'_0$ indicates an ink can withstand buckling and support its own weight over spanning features with minimal elastic deformation [11,16,108]. The rheological behavior of each ink is shown in **Figure 4.1**. The rheological properties of the base PCS resin are characterized in Chapter 3 and elsewhere [33,125]. The viscosity profile of both inks is shown in **Fig 4.1 A**. Here **Eq. 1.1** is fit to the apparent viscosity measurements using linear regression and used to find *K* and *n* for each ink. The value of *n* characterizes the nature of the fluid, where $n < 1$, $=1$, and $>1$ represent a shear-thinning fluid, a Newtonian fluid, and a shear-thickening fluid, respectively. The fitted values and their goodness of fit are shown in **Table 4.3.** Both inks have nearly identical viscosity profiles over the range of shear rates probed and are similar to SMP-0f's profile shown in Chapter 3 where their *n* values are less than 1.

Both G' and G" for both inks are shown in **Fig. 4.1 B**. For the majority of the stress range probed, the storage modulus is larger than the loss modulus,

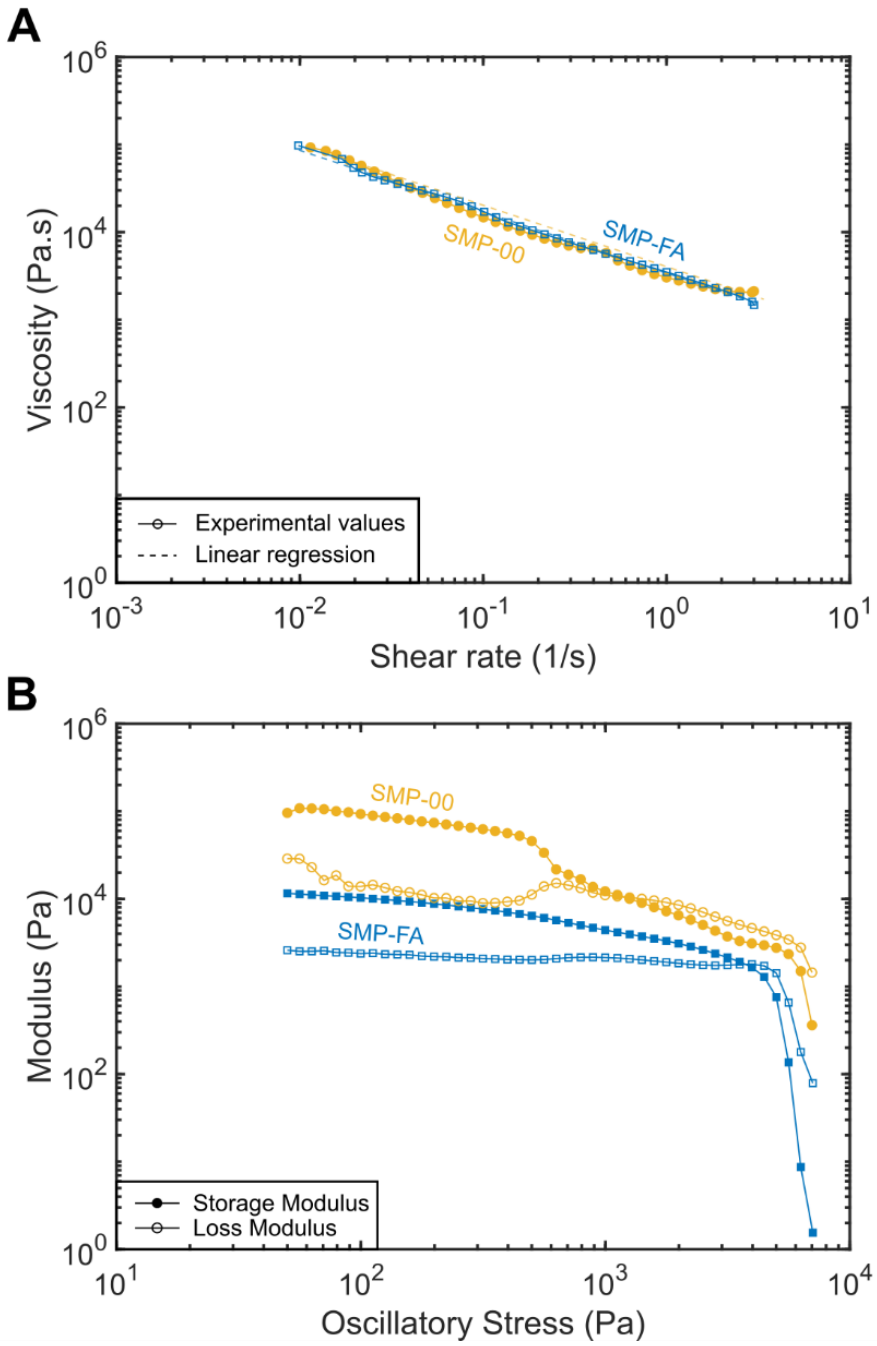


**Figure 4.1: Rheological behavior developed inks. (A) Apparent viscosity vs. shear rate. (B) Shear moduli vs. oscillatory shear stress.**

**Table 4.3: Rheological properties of DIW inks**

| Ink Name | $G'_0$ [kPa] | $\tau_y$ [Pa] | n | K [Pa•s] | $R^2$ |
|---|---|---|---|---|---|
| SMP-00 | 84.6 | 1119 | 0.28 | 3285 | 0.988 |
| SMP-FA | 9.58 | 3760 | 0.29 | 3491 | 0.982 |
| SMP-0f | 2.54 | 371 | 0.24 | 358 | 0.94 |

indicating nominally elastic solid-like behavior. With increasing stress, the particle network in each ink breaks down and G' decreases until it is surpassed by G". The $\tau_y$, described as the break-down point of the particle network, can be defined in several ways [114], but in this study, is defined as shear stress at which G" exceeds G', providing a direct comparison to the inks described in Chapter 3. SMP-00 and SMP-0f contain identical amounts of $ZrB_2$, with the difference being that SMP-0f has a milled portion of $ZrB_2$. Both SMP-00 and SMP-0f have similar $\tau_y$ values, but SMP-00 has a $G'_0$ value approximately 1 order of magnitude higher than SMP-0f. This is attributed to the presence of smaller $ZrB_2$ particles and a smaller gap size of 0.5 mm shown in Chapter 3 where particle surface area was larger in the SMP-0f ink [130].

With the addition of FA, a decrease in $G'_0$ and an increase in $\tau_y$ are observed. Fumed oxide materials, like the FA used in this study, have been a common additive for pastes and DIW inks [7,16,85] due to their inherent ability to induce shear-thinning behavior by forming networks of interconnected oxide colloidal aggregates [37,131,132]. Work with similar fumed $Al_2O_3$ materials has also shown that even a small addition of the fumed oxide increases a paste's $\tau_y$ [133]. The reduced $G'_0$ value for SMP-FA compared to SMP-00 may be explained by the reduced volume fraction of $ZrB_2$ in the SMP-FA ink, or it may be an effect of the fumed alumina or some interaction between the FA and $ZrB_2$. Fumed alumina has not been used as a viscosifier in preceramic polymer inks before, and

many open questions remain about its function and optimal use. These questions are of high interest, but are beyond the scope of the present work.

### *4.4.2 Thermal behavior*

TGA and DSC curves for both uncured inks up to 300°C and cured inks up to 1200°C are shown in **Figure 4.2 A** and **B**, respectively. For both the uncured SMP-00 and SMP-FA inks, mass loss (solid lines) begins at the onset of heating and proceeds at a constant rate until approximately 170°C (**Fig 4.2 A**), where the loss rate slows. DSC curves indicate that crosslinking initiates at ~120°C, with a peak exotherm between 170°C and 200°C, roughly corresponding to the reduction in the mass loss rate observed with TGA. During the initial ramp-up in temperature, the PCS present in each ink begins to off-gas low molecular weight oligomers, shown by mass loss up to 170°C. Interestingly, the SMP-00 differs from SMP-FA in that it has an endothermic reaction occurring at 210°C that also corresponds to a small mass loss event. At present, it is unclear what causes this event, but it is not observed in the PCS alone or the SMP-FA ink. Future work will focus on varying the content of FA and observing at what volume fraction of FA the endothermic reaction begins to occur. Additionally, mass-spectrometry and gas chromatography measurements during a similar heat ramp would help identify a difference in the composition of the gases evolving from each ink during curing and pyrolysis [134].

During pyrolysis (**Fig. 4.2 B**), both cured SMP-00 and SMP-FA samples show only ~1-2 wt.% total mass loss, while the neat PCS exhibits 24% total mass

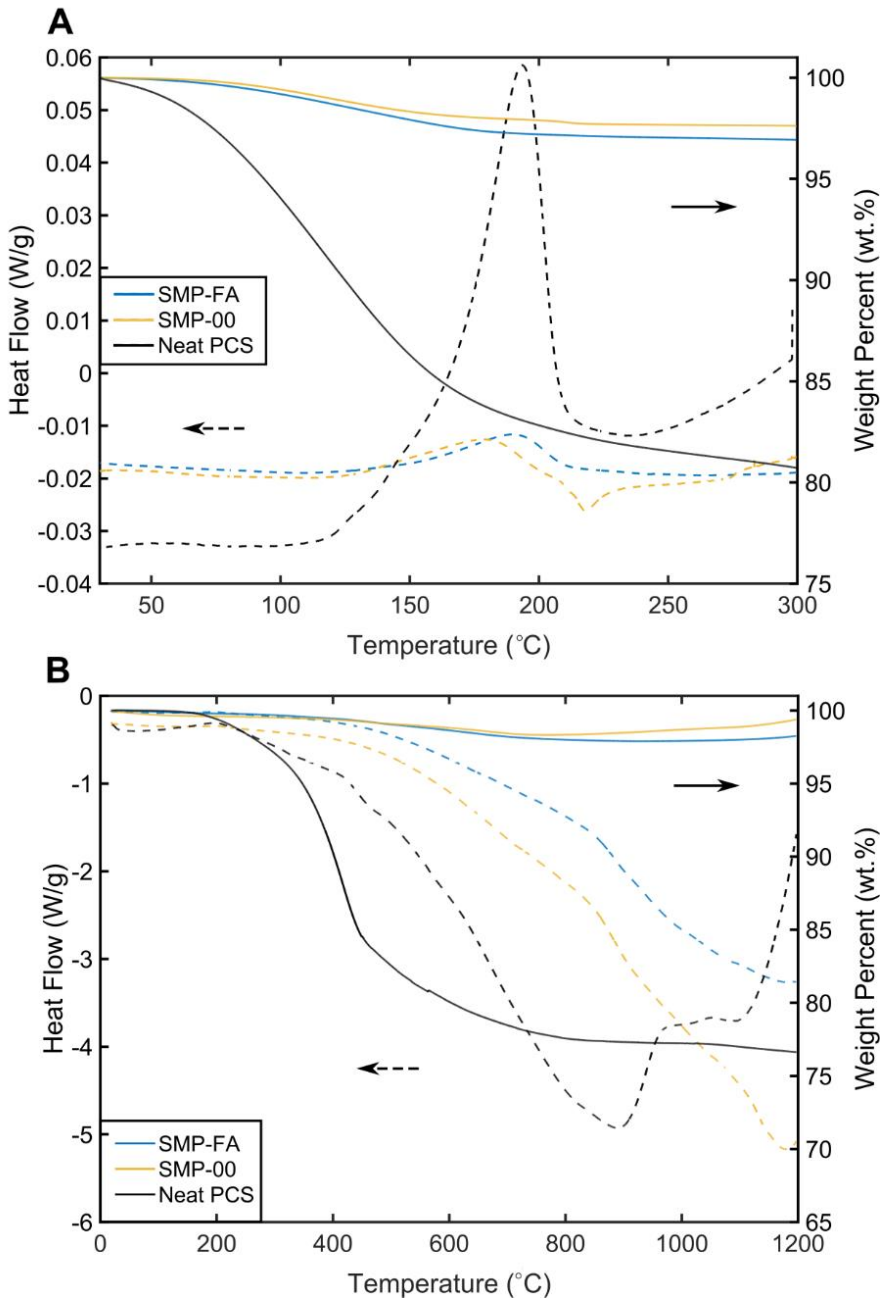


**Figure 4.2: Heat flow of reaction (left, dashed lines) and mass loss (right, solid lines) for (A) uncured inks and neat PCS resin up to 300°C, and (B) cured specimens up to 1200°C**

loss. All three cured materials have an initial mass loss event that begins at 200°C and ends at 400°C, with another event beginning at around 800°C. The large amount of inert ceramic filler content dominated the mass loss curves for the two inks.

**Figure 4.3** depicts representative regions of the bottom surface of microrods printed with 5 different nozzle diameters after curing. The surfaces were directly in contact with the PTFE-coated substrate. Looking at SMP-00 rods in **Fig 4.3 A** and moving from left to right, bubbles are not present in the smallest rod (nozzle diameter = 450 µm, width = 0.319 mm) but become prevalent as nozzle size increases. Additionally, as nozzle size increases, bubble size appears to increase. Large crack-like features form on the surface of the largest printed rods. For the SMP-FA rods in **Fig 4.3 B,** bubbles are observed in all rods except the smallest nozzle diameter size. In contrast to SMP-00, bubbles observed in the SMP-FA rods appear to be more consistent in size and distribution in the middle 3 nozzle sizes until reaching the largest nozzle size (1702 µm), where bubble size increases considerably.

To quantify the area of porosity on the bottom surface of printed and pyrolyzed, optical analysis was performed utilizing a Keyence microscope's built-in area analysis software. An example of the bubbles and the corresponding binary image is shown in **Figure 4.4**. Histograms of effective bubble radius, *r*, for each nozzle diameter for both SMP-00 and SMP-FA are shown in **Figure 4.5**, where $r = \sqrt{(A_b/\pi)}$, and $A_b$ is the area of a bubble. A bin size of 3 µm was used for the

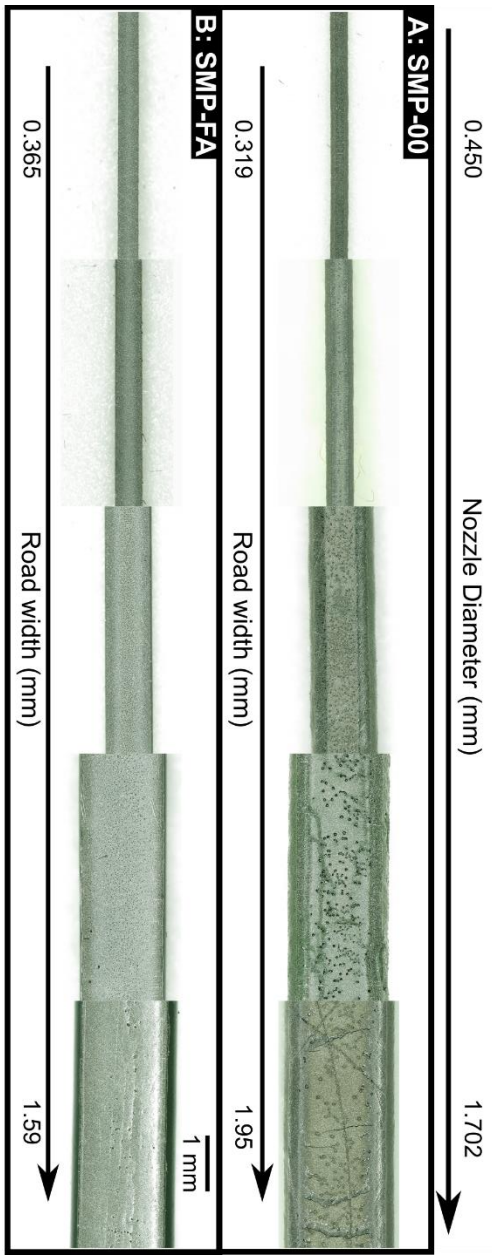


**Figure 4.3: Bubble formation on the bottom part of printed microrods. (A) and (B) show specimens made with SMP-00 and SMP-FA, respectively. Nozzle diameter used for deposition for both (A) and (B) increases from the left to right.**

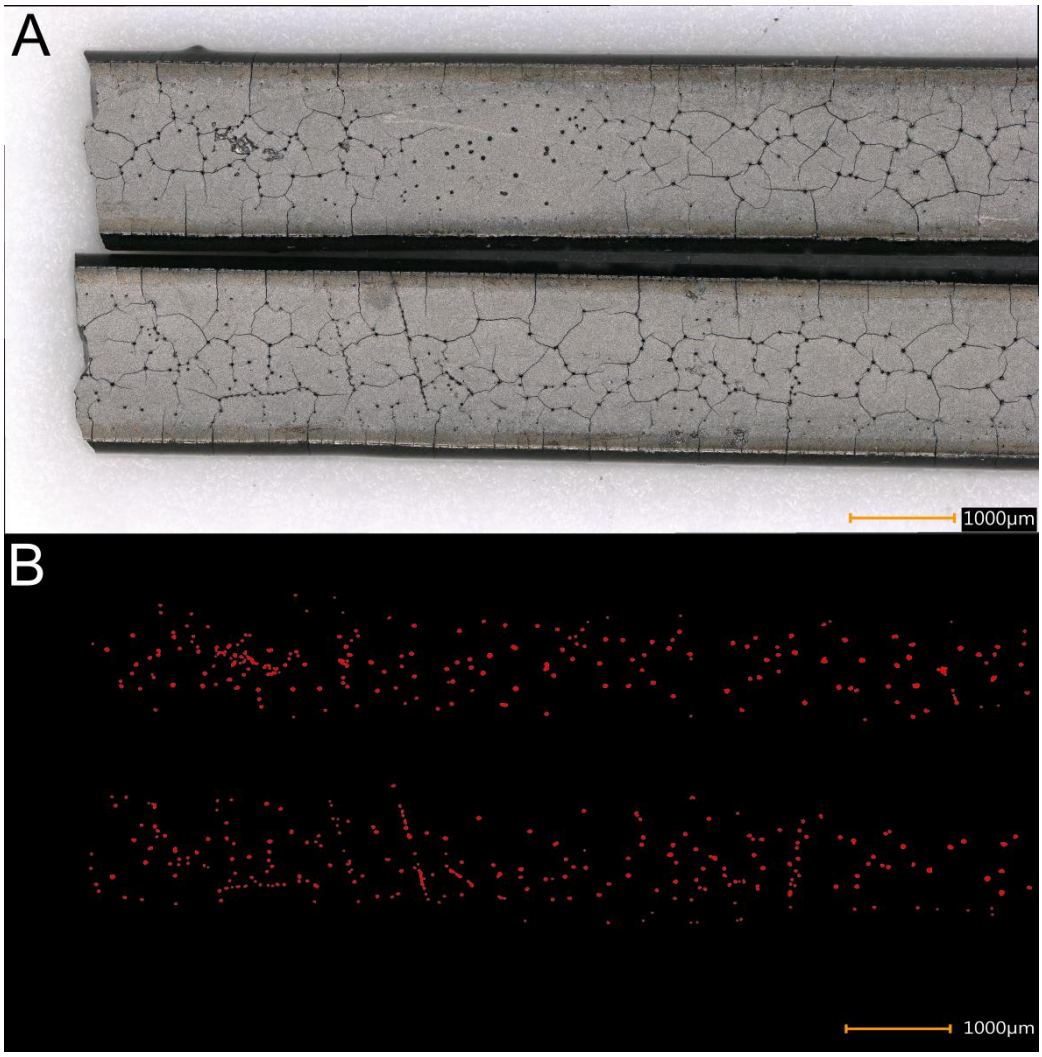


**Figure 4.4: Porosity composition image of 1.702 mm nozzle where (A) is the original image and (B) is the binary image of porosity highlighted in red.**

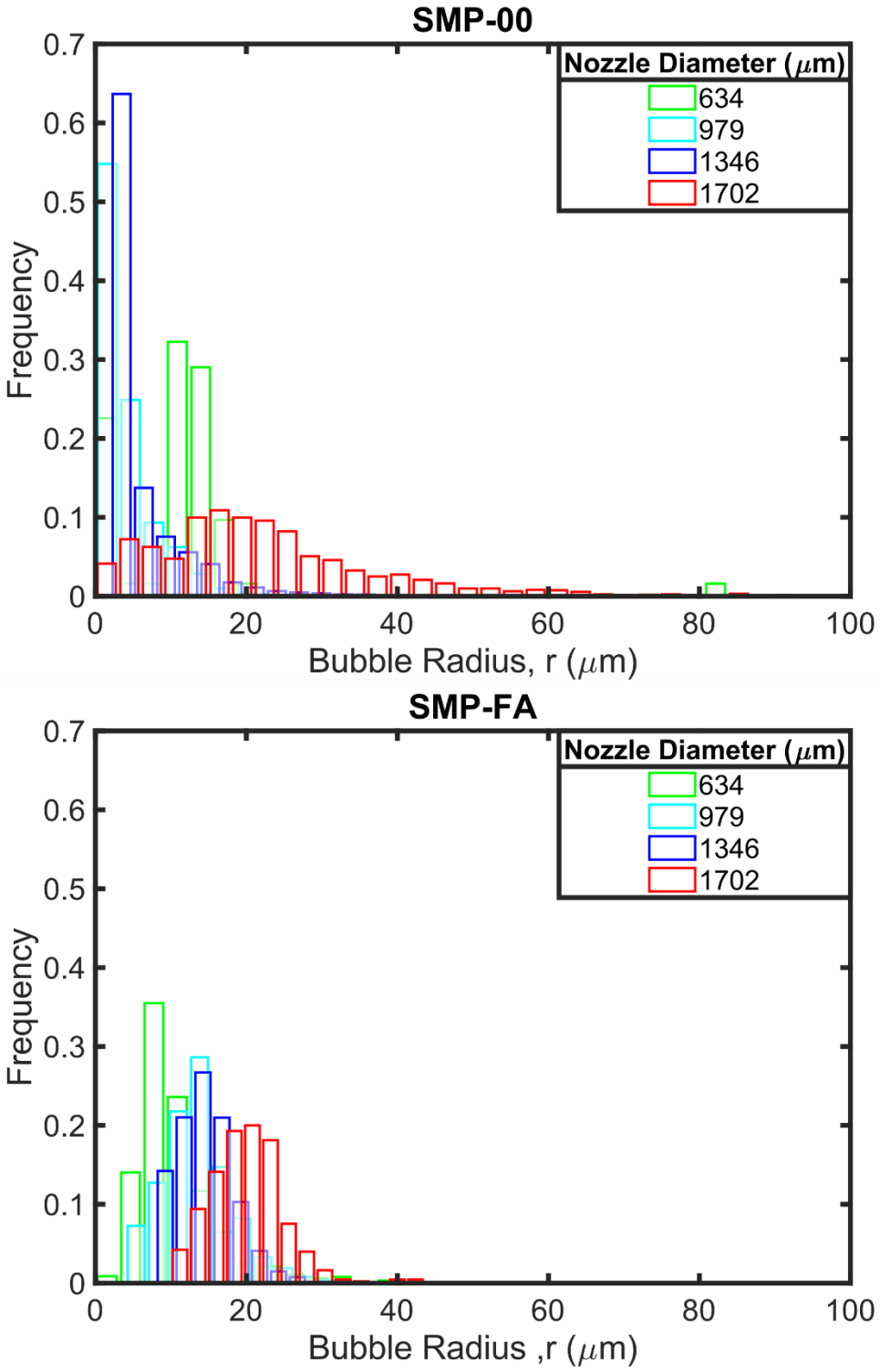


**Figure 4.5: Histograms of effective bubble radius for (A) SMP-00 and (B) SMP-FA.**

histograms. The smallest nozzle size, 450 µm, is not shown because no bubbles were observed at 1000 times magnification for both inks. For SMP-00 (**Fig. 4.5 A**), the three smallest nozzle sizes have a higher number of smaller bubbles. While for SMP-FA (**Fig. 4.5 B**), the with increasing nozzle size, *r* also tends to increase.

**Table 4.4** displays the total area of porosity measured on each specimen along with the number-average and mode *r*. The smallest printed rod has an average bubble size much larger than both the 979 and 1346 µm nozzles for the SMP-00 ink but has a much larger standard deviation. This indicates there are both very large and small bubbles present in the smallest nozzle size. For the largest nozzle size of 1702 µm, the SMP-00 has a large standard deviation in *r*. For SMP-FA, *r* increases in size from 26 µm to 35 µm between 1346 and 1702 µm nozzles. An additional measurement of the percentage of the area imaged (just the bottom surface) is shown in the final column of **Table 4.4**. The area percentage is just of the surface imaged and is not representative of the total volume of the microrod. This percentage, in tandem with the bubble size, shows that for both materials, the increase in bubble size for both inks is detrimental to the strength of the larger microrods and indicates that with increasing nozzle size, flaw distribution changes. This observation will be explored in subsequent sections.

The bubbles in **Fig 4.3 A** and **B** are caused by the off-gassing of oligomers and other hydrocarbon materials from the PCS polymer during curing, just like the inks shown in Chapter 3 [33,125], and as indicated in the TGA analysis (**Fig. 4.2**).

**Table 4.4: The measured area of all specimens used for porosity area calculation**

| Nozzle diameter [μm] | Number of bubbles measured, N | Total Area measured [μm$^2$] | Average effective bubble radius, r [μm] | Mode effective bubble radius, r [ μm] | Percentage of measured area that is bubbles [%] |
|---|---|---|---|---|---|
| | | | *SMP-00* | | |
| 634 | 62 | 2589.9 | 11.3 ± 10.5 | 1.38 | 1.78 |
| 979 | 17417 | 8920.9 | 4.36 ± 3.77 | 1.78 | 20.4 |
| 1346 | 12291 | 21790.7 | 6.17 ± 6.45 | 2.32 | 14.1 |
| 1702 | 1595 | 26818.2 | 23.2 ± 17.3 | 0.977 | 15.6 |
| | | | *SMP-FA* | | |
| 634 | 1496 | 5648.4 | 10.8 ± 5.89 | 5.56 | 12.5 |
| 979 | 2190 | 11050.3 | 13.5 ± 4.77 | 5.89 | 12.8 |
| 1346 | 3203 | 20253.6 | 14.7 ± 3.95 | 8.23 | 11.5 |
| 1702 | 425 | 30270.6 | 20.0 ± 4.84 | 11.5 | 1.88 |

The greater size of bubbles and the presence of a crack-like structure for the SMP-00 rods suggests that FA's addition in the SMP-FA may have aided in the diffusion process. FA is thought to aid in the gas diffusion of low-molecular-weight oligomers, whereas the $ZrB_2$ alone caused significant entrapment of gases. Because of the spheroidal shape of the $ZrB_2$ particles, gaps occur between individual particles. These gaps are places where gases can collect during off-gassing that lead to eventual porosity.

### *4.4.3 Mechanical testing*

32-mm-length microrods printed with 450, 634, 979, 1346, and 1702 µm-diameter nozzles were pyrolyzed and tested in 3-point flexure. Optical micrographs of the overall fracture surface of each microrod are shown in **Figures 4.6** and **4.7** for SMP-00 and SMP-FA, respectively. For the SMP-00 samples in **Fig 4.6**, a noticeable boundary in the center of the fracture surface develops in the larger rods. SEM along this boundary in the sample printed using the 1702-µm-diameter nozzle (**Fig. 4.6 E**) is shown in **Fig. 4.6 F**. A significant difference in contrast between the inner and outer surfaces can be seen, where the darker, inner region appears to be more porous when compared to the outer, lighter region. This observation may be the result of how gas diffuses in the specimens, where gas pressure in the center of the specimens may lead to a higher concentration of PCS polymer near the outer boundaries of the rods. An additional reason for this boundary structure may be due to the deposition process, where higher shear rates at the nozzle wall may lead to a higher concentration of polymer [122].

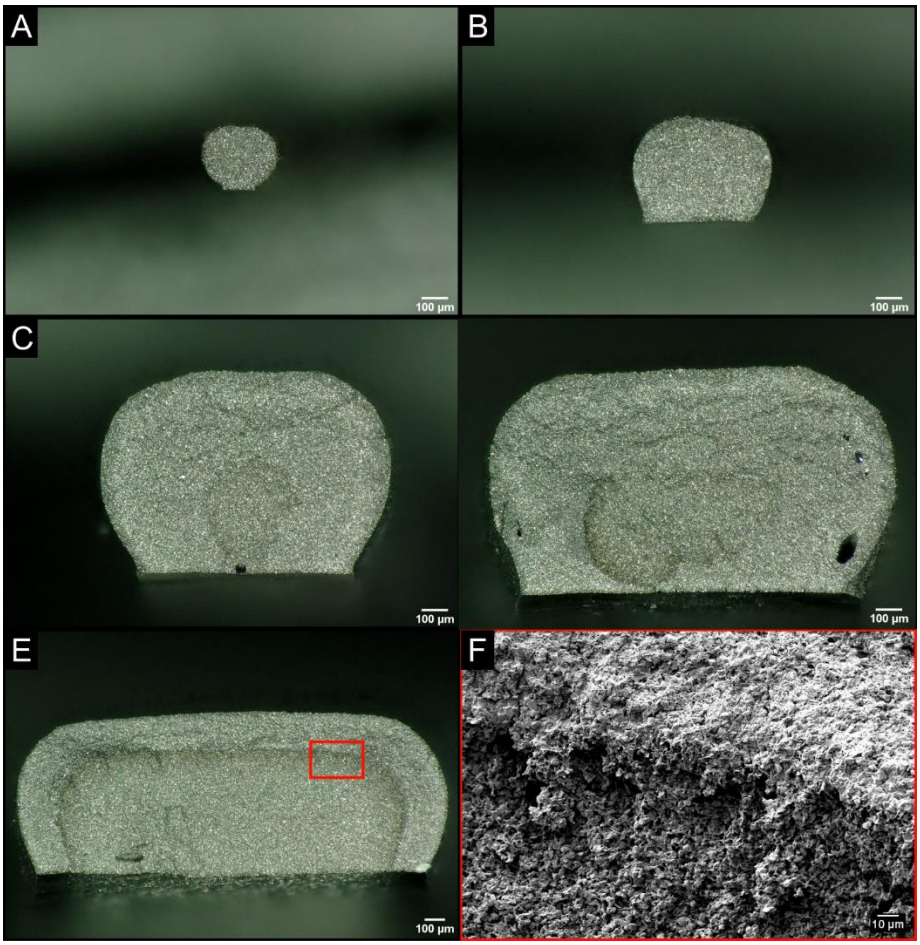


**Figure 4.6: Optical images of pyrolyzed fracture surfaces of microrods made with SMP-00. Deposition nozzle diameters used were (A) 450, (B) 634, (C) 979, (D) 1346, and (E) 1702 µm. (F) SEM micrograph of red boxed region shown in (E).**

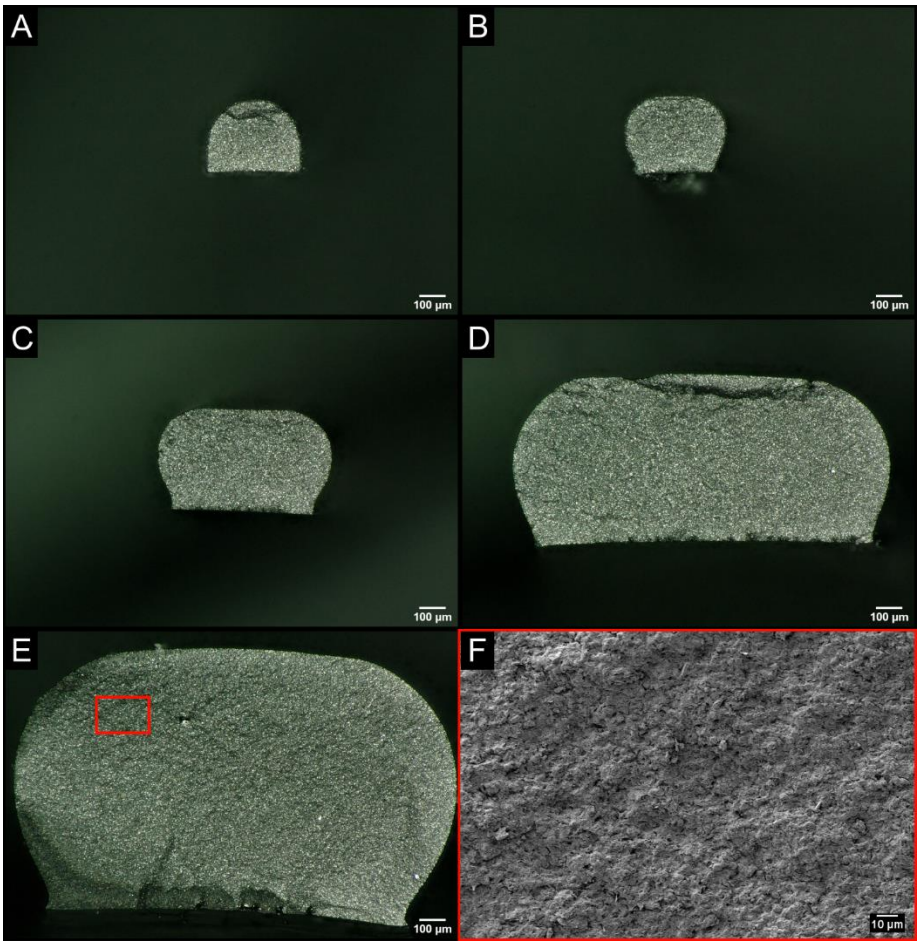


**Figure 4.7: Optical images of pyrolyzed fracture surfaces of microrods made with SMP-FA. Deposition nozzle diameters used were (A) 450, (B) 634, (C) 979, (D) 1346, and (E) 1702 µm. (F) SEM micrograph of red boxed region shown in (E).**

However, because the boundary feature is not observed on the bottom surfaces of the rods, where the major porosity forms, it appears more likely that the feature is related to off-gassing during curing.

Alternatively, for the SMP-FA samples (**Figure 4.7**), no circular internal boundary is apparent, and all fracture surfaces appear smoother and more uniform than those of the SMP-00 (**Fig 4.7 F**). Vickers microhardness indentations on polished cross-sections from the rods printed using the 1702-μm diameter reveal differences between the two different regions in the SMP-00. The inner region of the SMP-00 rods has a Vickers hardness of 2.84 ± 1.7 GPa, while the outer region has a Vickers hardness of 6.05 ± 0.45 GPa. The SMP-FA rod has a Vickers hardness value of 4.71 ± 0.11 GPa. The fact that the inner region of the SMP-00 samples had the lowest hardness is consistent with the hypothesis that gas evolution during curing leads to a lower concentration of PCS polymer in the central region of the printed samples, as discussed above. Therefore, future work will focus on identifying any compositional differences between the inner and outer regions of the SMP-00 samples using techniques such as energy-dispersive X-ray spectroscopy.

The measured cross-sectional area, $A_c$, of the fracture surface of a microrod with respect to the measured failure strength, $\sigma_f$ of each microrod, is shown in **Figure 4.8**. $\sigma_f$ for each microrod was calculated by using the classic bending formula:

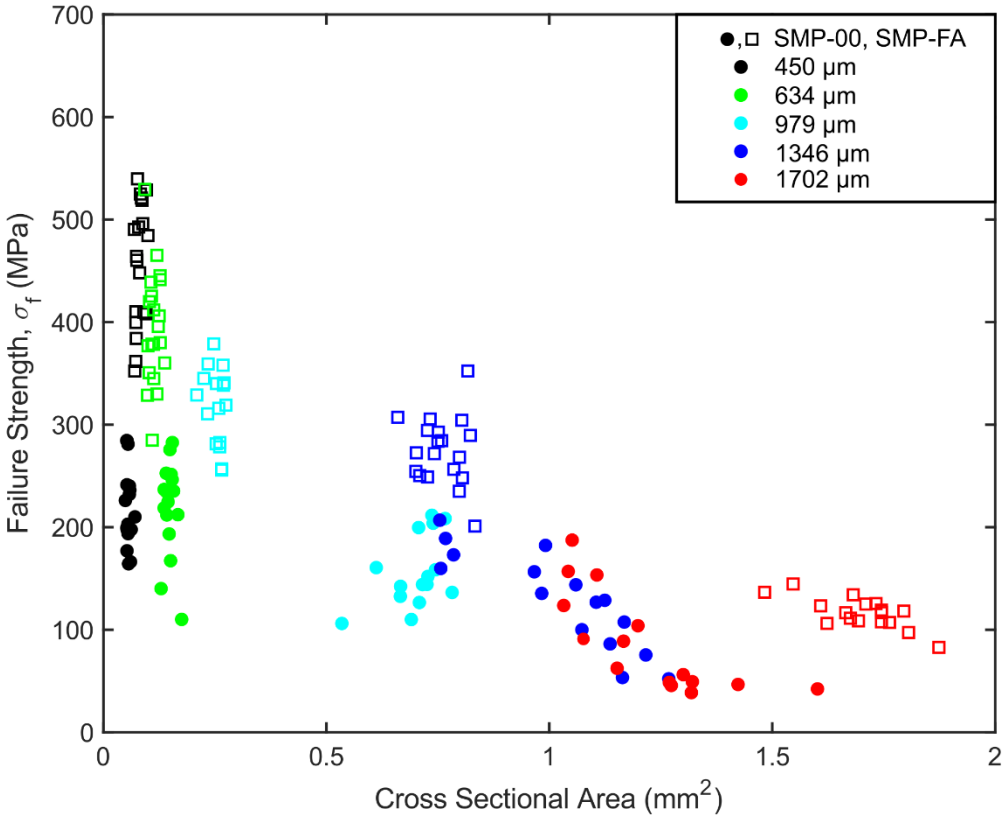


**Figure 4.8: Failure Strength as a function of $A_c$.**

$$\sigma_f = \frac{Mc}{I_x} \tag{4.10}$$

where *c* is the distance from the centroid to the bottom surface of the microrod, $I_x$ is the calculated $I_x$ from ImageJ, and *M* is the bending moment. The printed microrods were loaded in 3-pt. flexure, so that the maximum moment in the rod is $M = FL/4$ (where L is the span length of the microrod and *F* is the force applied to the rod at failure). Thus:

$$\sigma_f = \frac{FLc}{4I_x} \tag{4.11}$$

where $A_c$ was measured and $I_x$ was calculated using the open-source macro, MomentMacro, for ImageJ. The tool calculates $I_x$ following much of the work described by Medalia [135]. By plotting $A_c$ against $\sigma_f$, two major conclusions can be drawn from **Fig. 4.8**: i) strength is inversely related to cross-sectional area, and ii) SMP-FA is generally stronger than SMP-00. The decrease in strength is correlated with the presence, size, and amount of porosity observed on the bottom surfaces of the printed rods (**Figs. 4.4** and **4.6F**) and will be analyzed in greater depth in the following section.

### *4.4.4 Weibull analysis*

Weakest link theory states that the survival probability of a brittle solid depends on sample volume and flaw distribution [136]. Flaws within a sample ultimately dictate strength, meaning that larger volumes of material have a greater

likelihood of failure because of the increased chance of a failure initiating flaw being present in the sample [127,136]. Weibull suggested that a two-parameter fit can be used to interpret the probability of failure of brittle ceramics as a function of failure strength with the following equation:

$$P_f = 1 - \exp\left(-\left(\frac{\sigma_f}{\sigma_c}\right)^m\right) \tag{4.12}$$

where $P_f$ is the probability of failure, $m$ is the Weibull modulus, and $\sigma_c$ is some characteristic strength of tested specimens [128]. **Eq. 4.12** has been rearranged for better interpretation into the following form:

$$\ln\ln\left(\frac{1}{1-P_f}\right) = m\ln\sigma_f - m\ln\sigma_c \tag{4.13}$$

When strength data are plotted in this manner, a linear regression of the data provides the $m$ as the slope of the linear fit and $\mathrm{m}\ \ln\sigma_c$ as the y-intercept. Such plots for each family of printed microrods from both SMP-00 and SMP-FA are shown in **Figures 4.9 A** and **4.9 B**, respectively. All average $\sigma_f$, $\sigma_c$, and $m$ are shown in **Table 4.5**. SMP-00 $m$ values vary from ~3 to 6.8, while SMP-FA varies from ~8.6 to 10. SMP-00 has much lower $m$ and $\sigma_c$ when compared to the SMP-FA at the same nozzle size, corresponding to a greater dispersion of strength values within one family of samples. The decrease in strength with increasing nozzle diameter for both inks corresponds to the increase in porosity size shown in **Figure 4.4**. The diameter of the deposition nozzle affects how much porosity develops, which affects the strength of the rod. This size effect is expected from

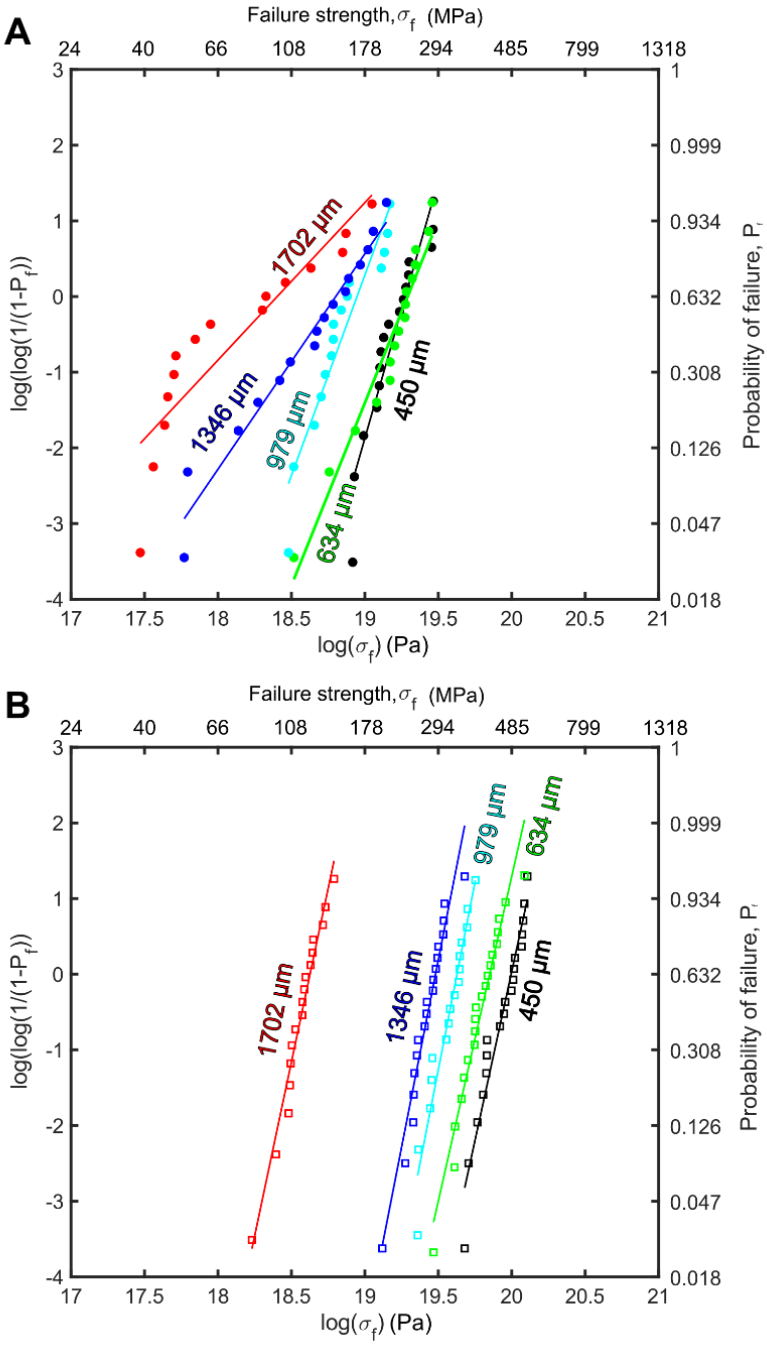


**Figure 4.9: Weibull plots of failure strength of (A) SMP-00 and (B) SMP-FA.**

**Table 4.5: Nozzle size, number of samples tested, average failure strength, characteristic strength, and Weibull modulus for both SMP-00 and SMP-FA samples**

| Nozzle Size [μm] | N, number of samples | Avg. Fracture Strength, $\sigma_f$ [MPa] | Char. Strength, $\sigma_c$ [MPa] | Weibull Modulus |
|---|---|---|---|---|
| | | *SMP-00* | | |
| 450 | 17 | 219.6 | 235.2 | 6.79 |
| 634 | 16 | 218.4 | 238.9 | 4.82 |
| 979 | 15 | 155.8 | 169.2 | 5.30 |
| 1346 | 15 | 129.8 | 146.4 | 2.97 |
| 1702 | 15 | 86.4 | 98.3 | 3.29 |
| | | *SMP-FA* | | |
| 450 | 19 | 457.6 | 483.3 | 8.93 |
| 634 | 20 | 394.6 | 417.4 | 8.58 |
| 979 | 16 | 318.2 | 334.3 | 9.94 |
| 1346 | 19 | 274.8 | 288.8 | 9.92 |
| 1702 | 17 | 116.5 | 122.7 | 9.36 |

the weakest link theory for brittle fracture, which has been extensively explored by many researchers [127,136].

Data from all tests were also plotted using **Eq. 4.13** in the manner described above (**Figure 4.10**). For both materials, there is a considerable shift in strength values for the largest samples tested. This reduction in strength for larger samples closely corresponds to the observed onset of cracking on the bottom surfaces of the larger sample (example shown in **Figure 4.11**), which strongly suggests that two separate flaw populations dictate the strength of printed polymer-derived ceramic composites: developed pores below a certain sample size, and cracks that form during pyrolysis dictate strength.

## 4.5 Conclusion

The effect of microrod size and filler composition on the development of porosity and $\sigma_f$ is investigated in this work. Inks were developed based on the SMP-0F, the SMP-0F ink shown in Chapter 3, but with an additional ink that included FA. The inks were used to deposit 32 mm long microrods of varying diameters. Microrods printed from both inks using a variety of nozzle diameters were tested with 3 pt. bend testing and analyzed with Weibull analysis. With increased nozzle size, an increase in porosity size occurred, leading to a decrease in flexural strength. Additionally, the addition of 6 vol.% of FA increased the strength at a given nozzle diameter. This work lays a foundation for understanding the effects of nozzle size and filler characteristics on the mechanical properties of printed PDC-based composites, but future work is warranted. Mainly, continued

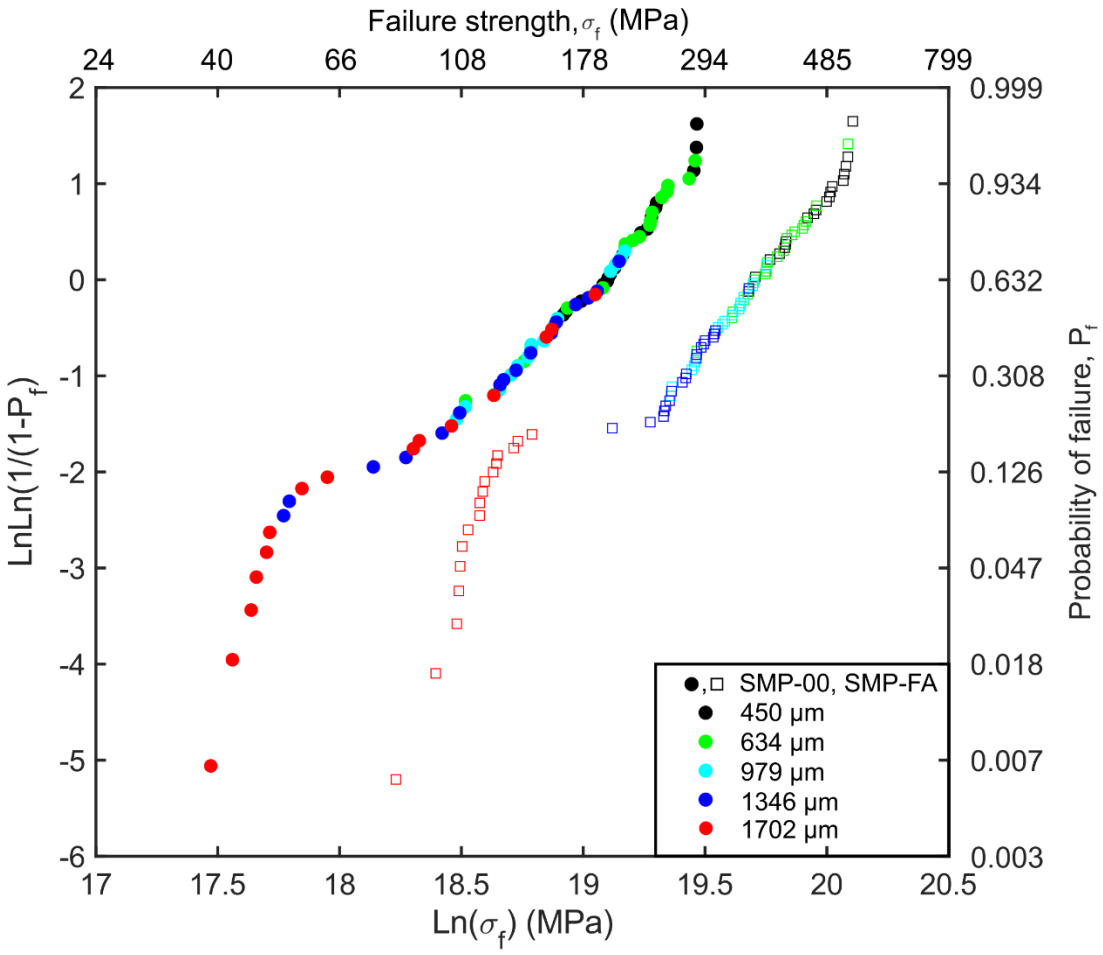


**Figure 4.10: Combined Weibull plots of all samples made from SMP-00 and SMP-FA specimens.**

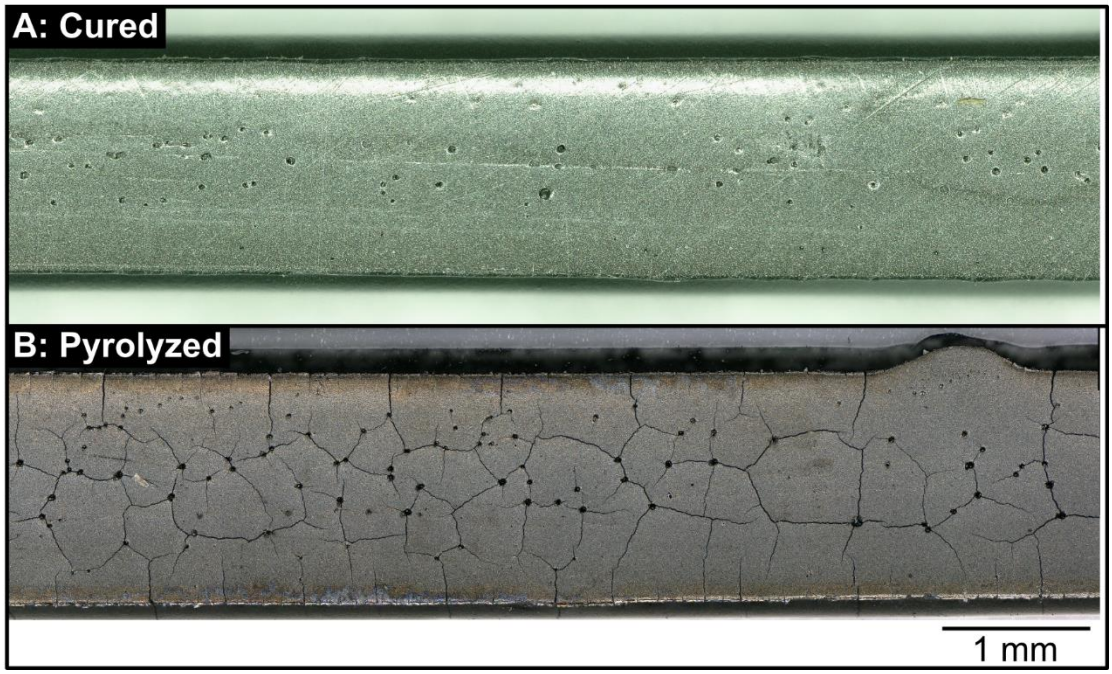


**Figure 4.11: SMP-FA rods made with the 1702 μm nozzle after (A) curing and (B) pyrolysis. The cured specimen only has observable pores, while the pyrolyzed specimen has interlocking cracks connecting the pores. (A) and (B) are different microrods, but are made with the same ink, and cured identically.**

study is needed to understand the exact mechanisms responsible for the development of porosity during curing in order to accurately describe the difference in porosity observed between the base and FA-containing inks.

# CHAPTER 5 CONCLUSION

The primary motivation driving much of this work was to develop near-neat shape, pore-free ceramic components with DIW of preceramic polymer inks. This was first achieved with a specific ink made polysilazane and hBN. The addition of a chemical initiator to the base polymer removed many of the volatile low-molecular-weight oligomers that cause porosity post-curing and pyrolysis. These printed structures were pore-free after full pyrolysis. Printed structures displayed failure strength and Vickers microhardness of 56.4 ± 7.6 MPa and 1.10 GPa, respectively.

Another ink was then developed with a SiC precursor polymer, $ZrB_2$, and chopped SiC fibers. In contrast to the polysilazane ink, these inks developed a large amount of porosity in printed parts after curing. Cracking also developed in these inks after pyrolysis due to polymer shrinkage. Failure strengths were observed to be 51.9 MPa and 38.3 MPa for the 5 and 10 vol.% fiber inks. These low values were caused by the large amount of porosity, which accounted for 11.16% and 24.63% of the measured fracture surface area for the 5 and 10 vol.% fiber inks, respectively. Mitigation strategies (i.e., polymer pretreatment, addition of chemical initiators, and proper filler selection) were outlined to reduce porosity and cracking effects. Finally, Micro-CT imaging was used to quantify fiber alignment along the print direction, where a higher volume fraction of fibers led to more misalignment of fibers.

The final part of this work investigated the extent to which sample size and filler morphology influence the development of porosity and overall strength.

Microrods of constant length were made from two preceramic inks, both with polycarbosilane and $ZrB_2$, while one had a small amount of FA added. Each ink was used to produce five different diameter rods made with deposition nozzle diameters ranging from 0.45 mm to 1.702 mm. These ten unique families of microrods were pyrolyzed, then tested in 3-point flexural testing. The fracture surfaces were imaged, and failure strengths were calculated for each microrod. The failure strengths were analyzed with Weibull statistics as well. For a given ink, the samples showed a trend to decrease in strength with increasing nozzle size, which was correlated to increasing porosity. Additionally, the ink containing FA had higher Weibull moduli (8.6-10) than those without FA (3-6.8) for a given nozzle size. The rods made without FA had high characteristic strengths (~240 MPa) up to a nozzle size of 634 µm, while the ink with FA had characteristic strengths greater than 280 MPa up to a nozzle size of 1346 µm. The interplay between polymer off-gassing, part size, and filler morphology is theorized to have strongly influenced the development of porosity and the strength of printed components.

# REFERENCES

[1] K. V Wong, A. Hernandez, A review of additive manufacturing, Int. Sch. Res. Not. 2012 (2012).

[2] W.J. Sames, F.A. List, S. Pannala, R.R. Dehoff, S.S. Babu, The metallurgy and processing science of metal additive manufacturing, Int. Mater. Rev. 61 (2016) 315–360. https://doi.org/10.1080/09506608.2015.1116649.

[3] F.P.W. Melchels, J. Feijen, D.W. Grijpma, A review on stereolithography and its applications in biomedical engineering, Biomaterials. 31 (2010) 6121–6130. https://doi.org/10.1016/j.biomaterials.2010.04.050.

[4] H. Windsheimer, N. Travitzky, A. Hofenauer, P. Greil, Laminated object manufacturing of preceramic-paper-derived Si-SiC composites, Adv. Mater. 19 (2007) 4515–4519. https://doi.org/10.1002/adma.200700789.

[5] J.E. Smay, J. Cesarano, J.A. Lewis, Colloidal inks for directed assembly of 3-D periodic structures, Langmuir. 18 (2002) 5429–5437. https://doi.org/10.1021/la0257135.

[6] J.A. Lewis, Colloidal processing of ceramics, J. Am. Ceram. Soc. 83 (2000) 2341–2359. https://doi.org/10.1111/j.1151-2916.2000.tb01560.x.

[7] G. Franchin, L. Wahl, P. Colombo, Direct ink writing of ceramic matrix composite structures, J. Am. Ceram. Soc. 100 (2017) 4397–4401. https://doi.org/10.1111/jace.15045.

[8] G. Franchin, H.S. Maden, L. Wahl, A. Baliello, M. Pasetto, P. Colombo, Optimization and characterization of preceramic inks for Direct Ink Writing of Ceramic Matrix Composite structures, Materials (Basel). 11 (2018) 515.

https://doi.org/10.3390/ma11040515.

[9] A. Zocca, C.M. Gomes, A. Staude, E. Bernardo, J. Günster, P. Colombo, SiOC ceramics with ordered porosity by 3D-printing of a preceramic polymer, J. Mater. Res. 28 (2013) 2243–2252. https://doi.org/10.1557/jmr.2013.129.

[10] E. Zanchetta, M. Cattaldo, G. Franchin, M. Schwentenwein, J. Homa, G. Brusatin, P. Colombo, Stereolithography of SiOC Ceramic Microcomponents, Adv. Mater. 28 (2016) 370–376. https://doi.org/10.1002/adma.201503470.

[11] N.S. Hmeidat, J.W. Kemp, B.G. Compton, High-strength epoxy nanocomposites for 3D printing, Compos. Sci. Technol. 160 (2018) 9–20. https://doi.org/10.1016/j.compscitech.2018.03.008.

[12] H. Koerner, D. Misra, A. Tan, L. Drummy, P. Mirau, R. Vaia, Montmorillonite-thermoset nanocomposites via cryo-compounding, Polymer (Guildf). 47 (2006) 3426–3435. https://doi.org/10.1016/j.polymer.2006.03.057.

[13] Z. Qin, B.G. Compton, J.A. Lewis, M.J. Buehler, Structural optimization of 3D-printed synthetic spider webs for high strength, Nat. Commun. 6 (2015) 1–7. https://doi.org/10.1038/ncomms8038.

[14] J.W. Kemp, N.S. Hmeidat, B.G. Compton, Boron nitride-reinforced polysilazane-derived ceramic composites via direct-ink writing, J. Am. Ceram. Soc. 103 (2020) 4043–4050. https://doi.org/10.1111/jace.17084.

[15] C. Duty, C. Ajinjeru, V. Kishore, B. Compton, N. Hmeidat, X. Chen, P. Liu, A.A. Hassen, J. Lindahl, V. Kunc, What makes a material printable? A viscoelastic model for extrusion-based 3D printing of polymers, J. Manuf. Process. 35 (2018) 526–537. https://doi.org/10.1016/j.jmapro.2018.08.008.

[16] S.K. Romberg, M.A. Islam, C.J. Hershey, M. DeVinney, C.E. Duty, V. Kunc, B.G. Compton, Linking thermoset ink rheology to the stability of 3D-printed structures, Addit. Manuf. 37 (2021) 101621. https://doi.org/10.1016/j.addma.2020.101621.

[17] E.N. Udofia, W. Zhou, A Guiding Framework for Microextrusion Additive Manufacturing, J. Manuf. Sci. Eng. Trans. ASME. 141 (2019). https://doi.org/10.1115/1.4042607.

[18] B.G. Compton, J.A. Lewis, 3D-printing of lightweight cellular composites, Adv. Mater. 26 (2014) 5930–5935. https://doi.org/10.1002/adma.201401804.

[19] P. Colombo, G. Mera, R. Riedel, G.D. Sorarù, Polymer-Derived Ceramics: 40 Years of Research and Innovation in Advanced Ceramics, J. Am. Ceram. Soc. 4 (2010) 245–320. https://doi.org/10.1002/9783527631971.ch07.

[20] G. Parcianello, Advanced ceramics from preceramic polymers and fillers, (2012) 186.

[21] P. Greil, Polymer derived engineering ceramics, Adv. Eng. Mater. 2 (2000) 339–348. https://doi.org/10.1002/1527-2648(200006)2:6<339::AID-

ADEM339>3.0.CO;2-K.

[22] P. Greil, Active-Filler-Controlled Pyrolysis of Preceramic Polymers, J. Am. Ceram. Soc. 78 (1995) 835–848. https://doi.org/10.1111/j.1151-2916.1995.tb08404.x.

[23] G. Perale, C. Giordano, F. Daniele, M. Masi, P. Colombo, L. Gottardo, S. Maccagnan, A novel process for the manufacture of ceramic microelectrodes for biomedical applications, Int. J. Appl. Ceram. Technol. 5 (2008) 37–43. https://doi.org/10.1111/j.1744-7402.2008.02186.x.

[24] K. Shiina, M. Kumada, Notes - Thermal Rearrangement of Hexamethyldisilane to Trimethyl(dimethylsilylmethyl)silane, J. Org. Chem. 23 (1958) 139–139. https://doi.org/10.1021/jo01095a635.

[25] E. Kroke, Y.L. Li, C. Konetschny, E. Lecomte, C. Fasel, R. Riedel, Silazane derived ceramics and related materials, Mater. Sci. Eng. R Reports. 26 (2000) 97–199. https://doi.org/10.1016/s0927-796x(00)00008-5.

[26] C.R. Krüger, E.G. Rochow, Polyorganosilazanes, J. Polym. Sci. Part A Gen. Pap. 2 (1964) 3179–3189.

[27] P. Greil, Near net shape manufacturing of polymer derived ceramics, Key Eng. Mater. 18 (1997) 1981–1984. https://doi.org/10.4028/www.scientific.net/kem.132-136.1981.

[28] G.D.S. and H.-J.K. Mielle, Philippe, P. Colombo, R. Riedel, Polymer Derived Ceramics: From Nano-structure to Applications: Poron-based precursors, DEStech Publications, Inc, 2010.

https://www.destechpub.com/product/polymer-derived-ceramics/.

[29] W.G. Fahrenholtz, G.E. Hilmas, I.G. Talmy, J.A. Zaykoski, Refractory diborides of zirconium and hafnium, J. Am. Ceram. Soc. 90 (2007) 1347–1364. https://doi.org/10.1111/j.1551-2916.2007.01583.x.

[30] M. Zaheer, T. Schmalz, G. Motz, R. Kempe, Polymer derived non-oxide ceramics modified with late transition metals, Chem. Soc. Rev. 41 (2012) 5102–5116. https://doi.org/10.1039/c2cs15326b.

[31] R.D. Miller, J. Michl, Polysilane High Polymers, Chem. Rev. 89 (1989) 1359–1410. https://doi.org/10.1021/cr00096a006.

[32] R.M. da Rocha, P. Greil, J.C. Bressiani, A.H. de A. Bressiani, Complex-shaped ceramic composites obtained by machining compact polymer-filler mixtures, Mater. Res. 8 (2005) 191–196.

[33] Z.D. Apostolov, E.P. Heckman, T.S. Key, M.K. Cinibulk, Effects of low-temperature treatment on the properties of commercial preceramic polymers, J. Eur. Ceram. Soc. 40 (2020) 2887–2895. https://doi.org/10.1016/j.jeurceramsoc.2020.02.030.

[34] R. D'Elia, G. Dusserre, S. Del Confetto, N. Eberling-Fux, C. Descamps, T. Cutard, Cure kinetics of a polysilazane system: Experimental characterization and numerical modelling, Eur. Polym. J. 76 (2016) 40–52. https://doi.org/10.1016/j.eurpolymj.2016.01.025.

[35] R. D'Elia, G. Dusserre, S. Del Confetto, N. Eberling-Fux, C. Descamps, T. Cutard, Effect of dicumyl peroxide concentration on the polymerization

kinetics of a polysilazane system, Polym. Eng. Sci. 58 (2018) 859–869. https://doi.org/10.1002/pen.24638.

[36] C. Wang, J. Wang, C.B. Park, Y.W. Kim, Cross-linking behavior of a polysiloxane in preceramic foam processing, J. Mater. Sci. 39 (2004) 4913–4915. https://doi.org/10.1023/B:JMSC.0000035335.92101.7c.

[37] A. Zocca, G. Franchin, H. Elsayed, E. Gioffredi, E. Bernardo, P. Colombo, A. Bandyopadhyay, Direct Ink Writing of a Preceramic Polymer and Fillers to Produce Hardystonite (Ca2ZnSi2O7) Bioceramic Scaffolds, J. Am. Ceram. Soc. 99 (2016) 1960–1967. https://doi.org/10.1111/jace.14213.

[38] Z.C. Eckel, C. Zhou, J.H. Martin, A.J. Jacobsen, W.B. Carter, T.A. Schaedler, Additive manufacturing of polymer-derived ceramics, Science (80-. ). 351 (2016) 58–62.

[39] P. Greil, M. Seibold, Modelling of dimensional changes during polymer-ceramic conversion for bulk component fabrication, J. Mater. Sci. 27 (1992) 1053–1060. https://doi.org/10.1007/BF01197660.

[40] D. Suttor, T. Erny, P. Greil, H. Goedecke, T. Haug, Fiber-reinforced ceramic-matrix composites with a polysiloxane/boron-derived matrix, J. Am. Ceram. Soc. 80 (1997) 1831–1840.

[41] L. Wei, J. Li, S. Zhang, B. Li, Y. Liu, F. Wang, S. Dong, Fabrication of SiOC ceramic with cellular structure via UV-Assisted direct ink writing, Ceram. Int. 46 (2020) 3637–3643. https://doi.org/10.1016/j.ceramint.2019.10.083.

[42] F.F. Lange, Powder Processing Science and Technology for Increased

Reliability, J. Am. Ceram. Soc. 72 (1989) 3–15. https://doi.org/10.1111/j.1151-2916.1989.tb05945.x.

[43] F.F. Lange, Shape forming of ceramic powders by manipulation the interparticle pair potential, Chem. Eng. Sci. 56 (2001) 3011–3020. https://doi.org/10.1016/S0009-2509(00)00484-X.

[44] J.A. Lewis, Direct ink writing of 3D functional materials, Adv. Funct. Mater. 16 (2006) 2193–2204. https://doi.org/10.1002/adfm.200600434.

[45] P. Calvert, T.L. Lin, H. Martin, Extrusion freeform fabrication of chopped-fibre reinforced composites, High Perform. Polym. 9 (1997) 449–456. https://doi.org/10.1088/0954-0083/9/4/008.

[46] A.A. Azeez, K.Y. Rhee, S.J. Park, D. Hui, Epoxy clay nanocomposites - Processing, properties and applications: A review, Compos. Part B Eng. 45 (2013) 308–320. https://doi.org/10.1016/j.compositesb.2012.04.012.

[47] L. Le Pluart, J. Duchet, H. Sautereau, P. Halley, J.F. Gerard, Rheological properties of organoclay suspensions in epoxy network precursors, Appl. Clay Sci. 25 (2004) 207–219. https://doi.org/10.1016/j.clay.2003.11.004.

[48] R.R. Collino, T.R. Ray, R.C. Fleming, J.D. Cornell, B.G. Compton, M.R. Begley, Deposition of ordered two-phase materials using microfluidic print nozzles with acoustic focusing, Extrem. Mech. Lett. 8 (2016) 96–106. https://doi.org/10.1016/j.eml.2016.04.003.

[49] J.R. Raney, B.G. Compton, J. Mueller, T.J. Ober, K. Shea, J.A. Lewis, Rotational 3D printing of damage-tolerant composites with programmable

mechanics, Proc. Natl. Acad. Sci. U. S. A. 115 (2018) 1198–1203. https://doi.org/10.1073/pnas.1715157115.

[50] G. Pierin, C. Grotta, P. Colombo, C. Mattevi, Direct Ink Writing of micrometric SiOC ceramic structures using a preceramic polymer, J. Eur. Ceram. Soc. 36 (2016) 1589–1594. https://doi.org/10.1016/j.jeurceramsoc.2016.01.047.

[51] H. Chen, X. Wang, F. Xue, Y. Huang, K. Zhou, D. Zhang, 3D printing of SiC ceramic: Direct ink writing with a solution of preceramic polymers, J. Eur. Ceram. Soc. 38 (2018) 5294–5300. https://doi.org/10.1016/j.jeurceramsoc.2018.08.009.

[52] L. David, S. Bernard, C. Gervais, P. Miele, G. Singh, Facile synthesis and high rate capability of silicon carbonitride/boron nitride composite with a sheet-like morphology, J. Phys. Chem. C. 119 (2015) 2783–2791. https://doi.org/10.1021/jp508075x.

[53] K.W. Gyak, N.K. Vishwakarma, Y.H. Hwang, J. Kim, H.S. Yun, D.P. Kim, 3D-printed monolithic SiCN ceramic microreactors from a photocurable preceramic resin for the high temperature ammonia cracking process, React. Chem. Eng. 4 (2019) 1393–1399. https://doi.org/10.1039/c9re00201d.

[54] J.A. Lewis, J.E. Smay, J. Stuecker, J. Cesarano, Direct ink writing of three-dimensional ceramic structures, J. Am. Ceram. Soc. 89 (2006) 3599–3609. https://doi.org/10.1111/j.1551-2916.2006.01382.x.

[55] T. Ma, R. Yang, Z. Zheng, Y. Song, Rheology of fumed silica/polydimethylsiloxane suspensions, J. Rheol. (N. Y. N. Y). 61 (2017) 205–215. https://doi.org/10.1122/1.4973974.

[56] N. Janakiraman, Z. Burghard, F. Aldinger, Fracture toughness evaluation of precursor-derived Si-C-N ceramics using the crack opening displacement approach, J. Non. Cryst. Solids. 355 (2009) 2102–2113. https://doi.org/10.1016/j.jnoncrysol.2009.07.002.

[57] J.P. Lewicki, J.N. Rodriguez, C. Zhu, M.A. Worsley, A.S. Wu, Y. Kanarska, J.D. Horn, E.B. Duoss, J.M. Ortega, W. Elmer, R. Hensleigh, R.A. Fellini, M.J. King, 3D-Printing of Meso-structurally Ordered Carbon Fiber/Polymer Composites with Unprecedented Orthotropic Physical Properties, Sci. Rep. 7 (2017) 1–14. https://doi.org/10.1038/srep43401.

[58] J. Peng, T.L. Lin, P. Calvert, Orientation effects in freeformed short-fiber composites, Compos. Part A Appl. Sci. Manuf. 30 (1999) 133–138. https://doi.org/10.1016/S1359-835X(98)00110-9.

[59] H.A. Pierson, E. Celik, A. Abbott, H. De Jarnette, L. Sierra Gutierrez, K. Johnson, H. Koerner, J.W. Baur, Mechanical Properties of Printed Epoxy-Carbon Fiber Composites, Exp. Mech. 59 (2019) 843–857. https://doi.org/10.1007/s11340-019-00498-z.

[60] B.G. Compton, N.S. Hmeidat, R.C. Pack, M.F. Heres, J.R. Sangoro, Electrical and mechanical properties of 3D-printed graphene-reinforced epoxy, Jom. 70 (2018) 292–297.

[61] V.L. Solozhenko, T. Peun, Compression and thermal expansion of hexagonal graphite-like boron nitride up to 7 GPa and 1800 K, J. Phys. Chem. Solids. 58 (1997) 1321–1323. https://doi.org/10.1016/S0022-3697(97)00037-1.

[62] A. Kovalčíková, J. Balko, C. Balázsi, P. Hvizdoš, J. Dusza, Influence of hBN content on mechanical and tribological properties of Si3N4/BN ceramic composites, J. Eur. Ceram. Soc. 34 (2014) 3319–3328. https://doi.org/10.1016/j.jeurceramsoc.2014.02.021.

[63] W. Ruigang, P. Wei, J. Mengning, C. Jian, L. Yongming, Investigation of the physical and mechanical properties of hot-pressed machinable Si3N4/h-BN composites and FGM, Mater. Sci. Eng. B Solid-State Mater. Adv. Technol. 90 (2002) 261–268. https://doi.org/10.1016/S0921-5107(01)01048-0.

[64] W.S. Cho, Y.H. Lee, M.W. Cho, E.S. Lee, J.H. Lee, Y.C. Hong, D.S. Park, Microstructure and mechanical properties of AlN-BN based machinable ceramics, Key Eng. Mater. 264–268 (2004) 873–876. https://doi.org/10.4028/www.scientific.net/kem.264-268.873.

[65] R. Shuba, I. Chen, Machinable α-SiAlON/BN Composites, J. Am. Ceram. Soc. 89 (2006) 2147–2153.

[66] Q. Weng, X. Wang, X. Wang, Y. Bando, D. Golberg, Functionalized hexagonal boron nitride nanomaterials: Emerging properties and applications, Chem. Soc. Rev. 45 (2016) 3989–4012.

https://doi.org/10.1039/c5cs00869g.

[67] M.J. Gasch, D.T. Ellerby, S.M. Johnson, Ultra High Temperature Ceramic Composites, in: Handb. Ceram. Compos., Springer US, 2006: pp. 197–224. https://doi.org/10.1007/0-387-23986-3_9.

[68] T.A. Parthasarathy, M.D. Petry, M.K. Cinibulk, T. Mathur, M.R. Gruber, Thermal and oxidation response of UHTC leading edge samples exposed to simulated hypersonic flight conditions, J. Am. Ceram. Soc. 96 (2013) 907–915. https://doi.org/10.1111/jace.12180.

[69] C.M. Carney, Oxidation resistance of hafnium diboride-silicon carbide from 1400 to 2000 °c, J. Mater. Sci. 44 (2009) 5673–5681. https://doi.org/10.1007/s10853-009-3799-7.

[70] C.M. Carney, P. Mogilvesky, T.A. Parthasarathy, Oxidation behavior of zirconium diboride silicon carbide produced by the spark plasma sintering method, J. Am. Ceram. Soc. 92 (2009) 2046–2052. https://doi.org/10.1111/j.1551-2916.2009.03134.x.

[71] V.L. Wiesner, L.M. Rueschhoff, A.I. Diaz-Cano, R.W. Trice, J.P. Youngblood, Producing dense zirconium diboride components by room-temperature injection molding of aqueous ceramic suspensions, Ceram. Int. 42 (2016) 2750–2760. https://doi.org/10.1016/j.ceramint.2015.11.005.

[72] S. Leo, L. Jukes, S. Pinches, C. Tallon, G. V. Franks, Freeze casting for near-net-shaping of dense zirconium diboride ceramics, J. Am. Ceram. Soc. 101 (2018) 2770–2785. https://doi.org/10.1111/jace.15451.

[73] T. Huang, G.E. Hilmas, W.G. Fahrenholtz, M.C. Leu, Dispersion of zirconium diboride in an aqueous, high-solids paste, Int. J. Appl. Ceram. Technol. 4 (2007) 470–479. https://doi.org/10.1111/j.1744-7402.2007.02157.x.

[74] Z. Lü, D. Jiang, J. Zhang, Q. Lin, Aqueous tape casting of zirconium diboride, J. Am. Ceram. Soc. 92 (2009) 2212–2217. https://doi.org/10.1111/j.1551-2916.2009.03222.x.

[75] R. He, X. Zhang, P. Hu, C. Liu, W. Han, Aqueous gelcasting of ZrB 2-SiC ultra high temperature ceramics, Ceram. Int. 38 (2012) 5411–5418. https://doi.org/10.1016/j.ceramint.2012.03.051.

[76] L.M. Rueschhoff, C.M. Carney, Z.D. Apostolov, M.K. Cinibulk, Processing of fiber-reinforced ultra-high temperature ceramic composites: A review, Int. J. Ceram. Eng. Sci. 2 (2020) 22–37. https://doi.org/10.1002/ces2.10033.

[77] J. Binner, M. Porter, B. Baker, J. Zou, V. Venkatachalam, V.R. Diaz, A. D'Angio, P. Ramanujam, T. Zhang, T.S.R.C. Murthy, Selection, processing, properties and applications of ultra-high temperature ceramic matrix composites, UHTCMCs–a review, Int. Mater. Rev. 65 (2020) 389–444. https://doi.org/10.1080/09506608.2019.1652006.

[78] L. Silvestroni, D.D. Fabbriche, D. Sciti, Tyranno SA3 fiber-ZrB2 composites. Part I: Microstructure and densification, Mater. Des. 65 (2015) 1253–1263. https://doi.org/10.1016/j.matdes.2014.08.068.

[79] L. Silvestroni, D. Sciti, C. Melandri, S. Guicciardi, Tyranno SA3 fiber-ZrB2 composites. Part II: Mechanical properties, Mater. Des. 65 (2015) 1264–1273. https://doi.org/10.1016/j.matdes.2014.08.075.

[80] L. Silvestroni, D. Sciti, C. Melandri, S. Guicciardi, Toughened ZrB2-based ceramics through SiC whisker or SiC chopped fiber additions, J. Eur. Ceram. Soc. 30 (2010) 2155–2164. https://doi.org/10.1016/j.jeurceramsoc.2009.11.012.

[81] L. Silvestroni, D. Sciti, G.E. Hilmas, W.G. Fahrenholtz, J. Watts, Effect of a weak fiber interface coating in ZrB2 reinforced with long SiC fibers, Mater. Des. 88 (2015) 610–618. https://doi.org/10.1016/j.matdes.2015.08.105.

[82] D. Sciti, L. Pienti, A. Natali Murri, E. Landi, V. Medri, L. Zoli, From random chopped to oriented continuous SiC fibers-ZrB2 composites, Mater. Des. 63 (2014) 464–470. https://doi.org/10.1016/j.matdes.2014.06.037.

[83] F. Yang, X. Zhang, J. Han, S. Du, Characterization of hot-pressed short carbon fiber reinforced ZrB2-SiC ultra-high temperature ceramic composites, J. Alloys Compd. 472 (2009) 395–399. https://doi.org/10.1016/j.jallcom.2008.04.092.

[84] J.J. Sha, J. Li, Z.Z. Lv, S.H. Wang, Z.F. Zhang, Y.F. Zu, S. Flauder, W. Krenkel, ZrB2-based composites toughened by as-received and heat-treated short carbon fibers, J. Eur. Ceram. Soc. 37 (2017) 549–558. https://doi.org/10.1016/j.jeurceramsoc.2016.09.012.

[85] N.S. Hmeidat, R.C. Pack, S.J. Talley, R.B. Moore, B.G. Compton,

Mechanical anisotropy in polymer composites produced by material extrusion additive manufacturing, Addit. Manuf. 34 (2020) 101385. https://doi.org/10.1016/j.addma.2020.101385.

[86] R. McKenzie, H. Koerner, Enabling direct writing of an epoxy resin with thermo-activated organic thixotropes, Addit. Manuf. 31 (2020) 100905. https://doi.org/10.1016/j.addma.2019.100905.

[87] A.S.J. Suiker, Mechanical performance of wall structures in 3D printing processes: Theory, design tools and experiments, Int. J. Mech. Sci. 137 (2018) 145–170. https://doi.org/10.1016/j.ijmecsci.2018.01.010.

[88] W.J. Costakis, L.M. Rueschhoff, A.I. Diaz-Cano, J.P. Youngblood, R.W. Trice, Additive manufacturing of boron carbide via continuous filament direct ink writing of aqueous ceramic suspensions, J. Eur. Ceram. Soc. 36 (2016) 3249–3256. https://doi.org/10.1016/j.jeurceramsoc.2016.06.002.

[89] E. Feilden, D. Glymond, E. Saiz, L. Vandeperre, High temperature strength of an ultra high temperature ceramic produced by additive manufacturing, Ceram. Int. 45 (2019) 18210–18214. https://doi.org/10.1016/j.ceramint.2019.05.032.

[90] S. Tang, L. Yang, G. Li, X. Liu, Z. Fan, 3D printing of highly-loaded slurries via layered extrusion forming: Parameters optimization and control, Addit. Manuf. 28 (2019) 546–553. https://doi.org/10.1016/j.addma.2019.05.034.

[91] Z. Lu, Y. Xia, K. Miao, S. Li, L. Zhu, H. Nan, J. Cao, D. Li, Microstructure control of highly oriented short carbon fibres in SiC matrix composites

fabricated by direct ink writing, Ceram. Int. 45 (2019) 17262–17267. https://doi.org/10.1016/j.ceramint.2019.05.283.

[92] Z. Zhao, G. Zhou, Z. Yang, X. Cao, D. Jia, Y. Zhou, Direct ink writing of continuous SiO2 fiber reinforced wave-transparent ceramics, J. Adv. Ceram. 9 (2020) 403–412. https://doi.org/10.1007/s40145-020-0380-y.

[93] H. Xiong, L. Zhao, H. Chen, H. Luo, X. Yuan, K. Zhou, D. Zhang, Building SiC-based composites from polycarbosilane-derived 3D-SiC scaffolds via polymer impregnation and pyrolysis (PIP), J. Eur. Ceram. Soc. 41 (2021) 1121–1131. https://doi.org/10.1016/j.jeurceramsoc.2020.09.059.

[94] H. Xiong, L. Zhao, H. Chen, X. Wang, K. Zhou, D. Zhang, 3D SiC containing uniformly dispersed, aligned SiC whiskers: Printability, microstructure and mechanical properties, J. Alloys Compd. 809 (2019) 151824. https://doi.org/10.1016/j.jallcom.2019.151824.

[95] S.A. Potticary, Chemical and Behavioral Study of Commercial Polycarbosilanes for the Processing of SiC Fibers, (2017).

[96] S. Kaur, R. Riedel, E. Ionescu, Pressureless fabrication of dense monolithic SiC ceramics from a polycarbosilane, J. Eur. Ceram. Soc. 34 (2014) 3571–3578. https://doi.org/10.1016/j.jeurceramsoc.2014.05.002.

[97] B. V. Velamakanni, F.F. Lange, Effect of Interparticle Potentials and Sedimentation on Particle Packing Density of Bimodal Particle Distributions During Pressure Filtration, J. Am. Ceram. Soc. 74 (1991) 166–172. https://doi.org/10.1111/j.1151-2916.1991.tb07313.x.

[98] T.S. Key, G.B. Wilks, T.A. Parthasarathy, D.S. King, Z.D. Apostolov, M.K. Cinibulk, Process modeling of the low-temperature evolution and yield of polycarbosilanes for ceramic matrix composites, J. Am. Ceram. Soc. 101 (2018) 2809–2818. https://doi.org/10.1111/jace.15463.

[99] C.J. Leslie, E.E. Boakye, K.A. Keller, M.K. Cinibulk, Development and characterization of continuous SiC fiber-reinforced HfB2-based UHTC matrix composites using polymer impregnation and slurry infiltration techniques, Int. J. Appl. Ceram. Technol. 12 (2015) 235–244. https://doi.org/10.1111/ijac.12279.

[100] D. King, Z. Apostolov, T. Key, C. Carney, M. Cinibulk, Novel processing approach to polymer-derived ceramic matrix composites, Int. J. Appl. Ceram. Technol. 15 (2018) 399–408. https://doi.org/10.1111/ijac.12805.

[101] L. Zoli, D. Sciti, Efficacy of a ZrB2–SiC matrix in protecting C fibres from oxidation in novel UHTCMC materials, Mater. Des. 113 (2017) 207–213. https://doi.org/10.1016/j.matdes.2016.09.104.

[102] C. Yan, R. Liu, Y. Cao, C. Zhang, Fabrication and properties of PIP 3D Cf/ZrC-SiC composites, Mater. Sci. Eng. A. 591 (2014) 105–110. https://doi.org/10.1016/j.msea.2013.10.102.

[103] C.M. Carney, P.W.R. Beaumont, C.H. Zweben, Comprehensive composite materials II, 2017. https://doi.org/10.1016/c2016-1-04658-8.

[104] ASTM International, ASTM C373-17: Standard Test Methods for Determination of Water Absorption and Associated Properties by Vacuum

Method for Pressed Ceramic Tiles and Glass Tiles and Boil Method for Extruded Ceramic Tiles and Non-tile Fired Ceramic Whiteware Products, ASTM Int. (2016) 5. https://doi.org/10.1520/C0373-18.2.

[105] A. International, Standard Test Method for Flexural Strength of Advanced Ceramics at Ambient, Order A J. Theory Ordered Sets Its Appl. 94 (1996) 1–15. https://doi.org/10.1520/C1161-18.1.

[106] J.C. Conrad, S.R. Ferreira, J. Yoshikawa, R.F. Shepherd, B.Y. Ahn, J.A. Lewis, Designing colloidal suspensions for directed materials assembly, Curr. Opin. Colloid Interface Sci. 16 (2011) 71–79. https://doi.org/10.1016/j.cocis.2010.11.002.

[107] D. Therriault, S.R. White, J.A. Lewis, Rheological behavior of fugitive organic inks for direct-write assembly, Appl. Rheol. 17 (2007) 10111–10112. https://doi.org/10.1515/arh-2007-0001.

[108] C. Zhu, J.E. Smay, Catenary shape evolution of spanning structures in direct-write assembly of colloidal gels, J. Mater. Process. Technol. 212 (2012) 727–733. https://doi.org/10.1016/j.jmatprotec.2011.04.005.

[109] M. Sepehr, P.J. Carreau, M. Moan, G. Ausias, Rheological properties of short fiber model suspensions, J. Rheol. (N. Y. N. Y). 48 (2004) 1023–1048. https://doi.org/10.1122/1.1773783.

[110] E.G. Barroso, F.M. Duarte, M. Couto, J.M. Maia, High strain rate rheological characterization of low viscosity fluids, Polym. Test. 29 (2010) 419–424. https://doi.org/10.1016/j.polymertesting.2009.11.012.

[111] D. Lootens, P. Hébraud, E. Lécolier, H. Van Damme, Gelation, Shear-Thinning and Shear-Thickening in Cement Slurries Solid/Liquid Dispersions in Drilling and Production Fluides chargés en forage et production pétrolière, 2004. https://ogst.ifpenergiesnouvelles.fr/articles/ogst/pdf/2004/01/lootens_vol59n1.pdf (accessed March 3, 2021).

[112] S. Cao, Q. He, H. Pang, K. Chen, W. Jiang, X. Gong, Stress relaxation in the transition from shear thinning to shear jamming in shear thickening fluid, Smart Mater. Struct. 27 (2018). https://doi.org/10.1088/1361-665X/aacbf8.

[113] N. Sidaoui, P. Arenas Fernandez, G. Bossis, O. Volkova, M. Meloussi, S. Aguib, P. Kuzhir, Discontinuous shear thickening in concentrated mixtures of isotropic-shaped and rod-like particles tested through mixer type rheometry, J. Rheol. (N. Y. N. Y). 64 (2020) 817–836. https://doi.org/10.1122/1.5138994.

[114] M. Dinkgreve, J. Paredes, M.M. Denn, D. Bonn, On different ways of measuring “the” yield stress, J. Nonnewton. Fluid Mech. 238 (2016) 233–241. https://doi.org/10.1016/j.jnnfm.2016.11.001.

[115] B.P. Croom, A. Abbott, J.W. Kemp, L. Rueschhoff, L. Smieska, A. Woll, S. Stoupin, H. Koerner, Mechanics of nozzle clogging during direct ink writing of fiber-reinforced composites, Addit. Manuf. 37 (2021). https://doi.org/10.1016/j.addma.2020.101701.

[116] Z. Yu, H. Min, L. Yang, Y. Feng, P. Zhang, R. Riedel, Influence of the architecture of dendritic-like polycarbosilanes on the ceramic yield, J. Eur. Ceram. Soc. 35 (2015) 1161–1171. https://doi.org/10.1016/j.jeurceramsoc.2014.10.037.

[117] D.J. Roach, C.M. Hamel, C.K. Dunn, M. V. Johnson, X. Kuang, H.J. Qi, The m4 3D printer: A multi-material multi-method additive manufacturing platform for future 3D printed structures, Addit. Manuf. 29 (2019) 100819. https://doi.org/10.1016/j.addma.2019.100819.

[118] J. Schulte-Fischedick, S. Seiz, N. Lützenburger, A. Wanner, H. Voggenreiter, The crack development on the micro- and mesoscopic scale during the pyrolysis of carbon fibre reinforced plastics to carbon/carbon composites, Compos. Part A Appl. Sci. Manuf. 38 (2007) 2171–2181. https://doi.org/10.1016/j.compositesa.2007.06.013.

[119] L. Rueschhoff, W. Costakis, M. Michie, J. Youngblood, R. Trice, Additive Manufacturing of Dense Ceramic Parts via Direct Ink Writing of Aqueous Alumina Suspensions, Int. J. Appl. Ceram. Technol. 13 (2016) 821–830. https://doi.org/10.1111/ijac.12557.

[120] F. Folgar, C.L. Tucker, Orientation Behavior of Fibers in Concentrated Suspensions., J. Reinf. Plast. Compos. 3 (1984) 98–119. https://doi.org/10.1177/073168448400300201.

[121] H.L. Tekinalp, V. Kunc, G.M. Velez-Garcia, C.E. Duty, L.J. Love, A.K. Naskar, C.A. Blue, S. Ozcan, Highly oriented carbon fiber-polymer

composites via additive manufacturing, Compos. Sci. Technol. 105 (2014) 144–150. https://doi.org/10.1016/j.compscitech.2014.10.009.

[122] Y. Kanarska, E.B. Duoss, J.P. Lewicki, J.N. Rodriguez, A. Wu, Fiber motion in highly confined flows of carbon fiber and non-Newtonian polymer, J. Nonnewton. Fluid Mech. 265 (2019) 41–52. https://doi.org/10.1016/j.jnnfm.2019.01.003.

[123] E. V. Bongio, S.L. Lewis, D.R. Welson, W.J. Sherwood, Polymer derived ceramic matrix composites for friction applications, Adv. Appl. Ceram. 108 (2009) 483–487. https://doi.org/10.1179/174367609X459522.

[124] S. Arreguin, R.K. Bordia, Precursor derived nanostructured Si-C-X materials for nuclear applications, Trans. Am. Nucl. Soc. 106 (2012) 107–108.

[125] J.W. Kemp, A.A. Diaz, E.C. Malek, B.P. Croom, Z.D. Apostolov, S.R. Kalidindi, B.G. Compton, L.M. Rueschhoff, Direct ink writing of ZrB2-SiC chopped fiber ceramic composites, Addit. Manuf. 44 (2021) 102049. https://doi.org/10.1016/j.addma.2021.102049.

[126] J. Xiao, Y. Jia, D. Liu, H. Cheng, Three-dimensional printing of SiCN ceramic matrix composites from preceramic polysilazane by digital light processing, Ceram. Int. 46 (2020) 25802–25807. https://doi.org/10.1016/j.ceramint.2020.07.061.

[127] J.B. Quinn, G.D. Quinn, A practical and systematic review of Weibull statistics for reporting strengths of dental materials, Dent. Mater. 26 (2010)

135–147. https://doi.org/10.1016/j.dental.2009.09.006.

[128] J.B. Wachtman, W.R. Cannon, M.J. Mathewson, Mechanical Properties of Ceramics, 2nd Edition, 2nd ed., John Wiley & Sons, Inc., 2009.

[129] O. Bera, M. Jovičič, J. Pavličevič, B. Pilič, The influence of oxide nanoparticles on the kinetics of free radical methyl methacrylate polymerization in bulk, Polym. Compos. 34 (2013) 1342–1348. https://doi.org/10.1002/pc.22548.

[130] S.M. Olhero, J.M.F. Ferreira, Influence of particle size distribution on rheology and particle packing of silica-based suspensions, Powder Technol. 139 (2004) 69–75. https://doi.org/10.1016/j.powtec.2003.10.004.

[131] K. Zhu, D. Yang, Z. Yu, Y. Ma, S. Zhang, R. Liu, J. Li, J. Cui, H. Yuan, Additive manufacturing of SiO2–Al2O3 refractory products via Direct Ink Writing, Ceram. Int. 46 (2020) 27254–27261. https://doi.org/10.1016/j.ceramint.2020.07.210.

[132] S.R. Raghavan, S.A. Khan, Shear-induced microstructural changes in flocculated suspensions of fumed silica, J. Rheol. (N. Y. N. Y). 39 (1995) 1311–1325. https://doi.org/10.1122/1.550638.

[133] J.S. Weston, D. Venkataramani, C.P. Aichele, B.P. Grady, J. Harwell, D. Resasco, Pseudosolid, shear-thinning gel formation in binary dispersions of metal oxide nanoparticles at low volume fractions, Langmuir. 30 (2014) 14982–14990. https://doi.org/10.1021/la503442a.

[134] C.G. Campbell, D.J. Astorga, E. Duemichen, M. Celina, Thermoset

materials characterization by thermal desorption or pyrolysis based gas chromatography-mass spectrometry methods, Polym. Degrad. Stab. 174 (2020) 109032. https://doi.org/10.1016/j.polymdegradstab.2019.109032.

[135] A.I. Medalia, Dynamic shape factors of particles, Powder Technol. 4 (1971) 117–138. https://doi.org/10.1016/0032-5910(71)80021-9.

[136] F.W. Zok, On weakest link theory and Weibull statistics, J. Am. Ceram. Soc. 100 (2017) 1265–1268. https://doi.org/10.1111/jace.14665.

# VITA

James William Kemp was born and raised in Gallatin, Tennessee. James received his Bachelor of Science degree in Materials Science and Engineering from the University of Tennessee, Knoxville, where he received the highest honor a graduating senior can receive, the Torchbearer award. Upon completing his degree, he received the Chancellor's Fellowship for the Mechanical, Aerospace, and Biomedical department to start his Ph.D. in Dr. Brett Compton's group. The focus of his research has been using the additive manufacturing technique of direct ink writing to 3D print preceramic polymer materials. During his Ph.D. research, James was also an Air Force Research Laboratory scholar, where he got to work under Dr. Lisa Rueschhoff's mentorship at the Air Force Research Laboratory at Wright Patterson Air Force Base. James's primary research focus has been preceramic polymer direct ink writing and the processing difficulties that arise during curing and pyrolysis.